

Maskless plasma etching antireflection nanostructures on  
optical elements in concentrator photovoltaic systems

(集光型太陽光発電システムにおけるマスクレス・プラズマ  
エッチング・ナノ構造を用いた低反射光学素子)

Tamayo Ruiz Efrain Eduardo

タマヨ ルイス エフライン エドゥアルド



Maskless plasma etching antireflection nanostructures on  
optical elements in concentrator photovoltaic systems

(集光型太陽光発電システムにおけるマスクレス・プラズマ  
エッチング・ナノ構造を用いた低反射光学素子)

Tamayo Ruiz Efrain Eduardo

タマヨ ルイス エフライン エドゥアルド

A thesis submitted in partial fulfillment of the requirements for the degree of  
*Doctor of Philosophy*

Department of Advanced Interdisciplinary Studies  
Graduate School of Engineering  
The University of Tokyo

Supervisor: Professor Yoshitaka Okada

December, 2013





“We are star stuff harvesting sunlight.”

“One of the reasons for its success is that science has a built-in, error-correcting machinery at its very heart. Some may consider this an overbroad characterization, but to me every time we exercise self-criticism, every time we test our ideas against the outside world, we are doing science. When we are self-indulgent and uncritical, when we confuse hopes and facts, we slide into pseudoscience and superstition.”

- Carl Sagan (1934-1996)



## **Abstract**

Concentrator Photovoltaic (CPV) systems are a potential candidate to achieve low cost solar energy because in these systems the solar cell efficiency increases with concentration and the amount of semiconductor material required is lower. CPV systems use Fresnel lenses to focus the light into homogenizers, which uniformizes the flux distribution incident to the subjacent solar cell and does other optical corrections. A disadvantage of these optical elements is that they create three optical interfaces that reflect the incident light and together account for about 12% of losses. To achieve higher efficiency in CPV systems, these losses need to be reduced. These optical interfaces can be curved or corrugated, which limits the applicability of conventional antireflection methods. In addition, the antireflection effect should be broadband because the solar cell placed below the homogenizer absorbs most of the solar spectrum. In order to be suitable for production lines, the fabrication methods need to be applicable in large areas and to be cost effective. For these reasons, maskless plasma etching processes were selected to texture the PMMA (Fresnel lens) and glass (homogenizer) interfaces. An additional problem in CPV systems is the dew condensation on the front and back side of the Fresnel lenses. To solve this problem, a hydrophobic coating on an antireflection nanostructured surface was evaluated on the back side of a Fresnel lens.

In chapter 1, the basics of solar energy, CPV systems, and the motivation and outlines are introduced. In chapter 2, the approaches employed to study and improve CPV systems are described. Also in this chapter, the CPV system studied is introduced along with numerical calculations of optimum antireflection nanostructures. Chapter 3 is focused on the fabrication methods employed to fabricate broadband antireflection nanostructures on glass and on PMMA. The composition of the studied homogenizer is close to the composition of Schott B270 glass, which was the main material studied. Employing Schott B270 glass substrates, a  $\text{CHF}_3$  plasma etching process achieving the fabrication of high aspect ratio nanostructures was developed.

O<sub>2</sub> plasma etching and water rinsing were applied as cleaning processes afterwards. Broadband high transmittance was achieved on Schott B270 glass substrates, reaching nearly 96% and over 99% on samples with one and both treated sides, respectively. This improvement resulted from the formation of high aspect ratio nanostructures and graded material distributions created by the selective removal of SiO<sub>2</sub> during CHF<sub>3</sub> plasma etching, resulting in low SiO<sub>2</sub> density at the tips of the nanostructures and increasing density towards the bulk substrate. The aspect ratio of the nanostructures increased with increasing the CHF<sub>3</sub> plasma etching process time. In B270, the formation of high aspect ratio nanostructures was achieved without lithography or the assistance of any deposited mask, making it a novel fabrication method and suitable for curved and large surfaces. The surface of various types of glasses and quartz substrates were treated using the same processes obtaining large or moderate transmittance enhancements, or scattering properties. The transmittance enhancement depended on the size and aspect ratio of the nanostructures. Scattering appeared when fabrication of large structures on the surface was obtained. Surface and cross section composition measurements revealed that the glass composition plays a critical role to obtain antireflection or scattering structures. FDTD and RCWA simulations were carried out to study the morphology and graded composition effects. The controllability of the wettability properties on nanostructured B270 using self-assembled molecular monolayer is also presented.

At the Fraunhofer IOF (Jena, Germany) two types of processes were applied on PMMA substrates and LPI's Fresnel lenses. The first one (S1) uses a self-generated mask formed during O<sub>2</sub> and Ar plasma etching. The second type (S2) uses a TiO<sub>2</sub> thin layer prior to the same process as in S1. Depending on the fabrication process, two types of antireflection structures were generated and applied on one-side and both-sides of PMMA substrates and Fresnel lenses.

In chapter 4, the optical and field tests evaluation of Fresnel lenses and homogenizers with nanostructured surfaces are presented. Module assembly and field tests were carried out at LPI-CeDint facilities (Madrid, Spain). The Current-Voltage curves were measured for each sample and the efficiencies were calculated. Spectrolab Concentrator Cell Assemblies (CCAs) using triple junction solar cell GaInP (1.88 eV) / GaInAs (1.41 eV) / Ge (0.67 eV) were encapsulated below the treated homogenizers and a reference Fresnel lens was used to evaluate the effect of the glass nanostructuring process, which achieved maximum 3.78% and 2.75%  $J_{sc}$  and efficiency relative gains, respectively. To evaluate the effect of the nanostructures on the Fresnel lenses, the same bare secondary optical element and Spectrolab CCAs were employed.

On the Fresnel lens with S2 on both sides, maximum 6.56% and 3.82%  $J_{sc}$  and efficiency relative gains were obtained, respectively. Finally, the CPV module assembled using the Fresnel lens with S2 on both sides and the best treated homogenizer showed 7.99% and 5.06%  $J_{sc}$  and efficiency relative gains, respectively.

The efficiency relative gains were lower than the  $J_{sc}$  ones because the Fill Factor (FF) was degraded on the textured samples. The origin of the FF decrease is under consideration, but it was found that the bottom cell does not become limiting when employing the antireflection nanostructures. Overheat of the cell by increased current or the modifications of the spectral or irradiance homogeneity on the sub-cells are other plausible causes.  $V_{oc}$  remained unchanged;  $J_{sc}$  was normalized at Direct Normal Irradiation  $900 \text{ W/m}^2$  and the efficiency at  $25^\circ\text{C}$ . The hydrophobic coating was applied on S2 on the back side of a Fresnel lens and it was tested using University of Tokyo's CPV system. The hydrophobic coating caused a slight decrease in the transmittance at short wavelengths, but a 7.73%  $J_{sc}$  relative gain was obtained. The uncoated Fresnel lens with S2 on the back side showed a 2.87%  $J_{sc}$  relative gain. The additional enhancement could be the result of a focal point modification by the coating. Further study of this additional gain is under consideration.

In chapter 5, applications to flat PV of nanostructured glass and PMMA surfaces are introduced employing InAs Quantum-Dot solar cells. Also, the applications to space cover glasses and aspheric lenses were demonstrated. Finally, in chapter 6, the conclusions and outlines of this thesis are presented.



# Acknowledgements

This thesis describes the research carried out while the author was a graduate student in the Department of Advanced Interdisciplinary studies at Research Center for Advanced Science and Technology, the University of Tokyo, from April 2011 to March 2014.

First and foremost, I would like to express my gratitude to my thesis supervisors Professor Yoshitaka Okada and Professor Kenjiro Miyano for this opportunity and for the support, encouragements, and freedom they gave me in my research.

I wish to specially thank my thesis committee members Professor Masakazu Sugiyama, Professor Takaya Kubo, Professor Shinji Yamashita, and Professor Eiji Higurashi, for taking the time to review my thesis and providing me valuable comments and suggestions to complete it.

I wish to express my deep gratitude to Dr. Ryo Tamaki for all his instruction, support, and discussions particularly on the optical measurements and building the optical setup, to Dr. Takuya Hoshii for his support and encouragement during difficult moments as well as for his insight and skills in the XPS and EDX measurements that were crucial to understand the self-generated masks generation during the plasma etching on glass surface, and to Dr. Kentaroh Watanabe for his support in several kinds of experiments, field tests, simulations and discussions. I gratefully acknowledge Dr. Masanori Kubota and Mr. Shigeru Furuya for assistance and instruction with the plasma etching equipment.

I feel very fortunate and grateful to have had the chance to collaborate with other laboratories in campus as well as with institutes and companies abroad that played a significant role from discussions to overcoming difficulties and altogether to demonstrate CPV module efficiency enhancements by texturing the surfaces of the optical elements. I would like to thank Professor Ulrike Schulz, Dr. Kevin Fuchs, Dr. Friedrich Rickelt, and Dr. Peter Munzert from the Fraunhofer Institute of Applied Optics and Precision Engineering, and Dr. Andreas Büchtemann from the Fraunhofer

Institute for Applied Polymer Research, for their support and collaboration on texturing the front and back side of PMMA substrates and Fresnel lenses. I would like to thank Dr. Rubén Mohedano, Dr. Aleksandra Cvetkovic, Dr. Juan V. Nicolau, Dr. Maikel H. Sanz, and Dr. Jose B. Flores, from Light Prescription Innovators for collaboration in prototypes assembly and CPV field tests measurements.

I am thankful to Dr. James Hall and Dr. Andy Grail from Qioptiq, and to Dr. Scott Burroughs, Dr. Brent Fisher, and Dr. Steven Steel from Semprius Inc., for their trust and willingness to collaborate and try the glass nanostructuring process on the space cover glass and CPV optical elements, respectively.

I would like to show my gratitude to Professor Koji Ikuta, and Professor Beomjoon Kim for their support and for allowing me to carry out experiments in their laboratories, and to Dr. Masashi Ikeuchi and Mr. Ikjoo Byun for their advice and help in implementing several experiments.

I am indebted to current and former members of Okada Laboratory who everyday helped make this a very fruitful and stimulating experience: Dr. Nazmul Ahsan, Dr. Naoya Miyashita, Dr. Tomah Sogabe, Dr. Daniel J. Farrell, Dr. Yasushi Shoji, Dr. Toshiyuki Kaizu, Dr. M. Monirul Islam, Dr. Katsuhisa Yoshida, Mr. Mitsuyoshi Ohba, Mr. Akio Ogura, Mr. Chao-Yu Hung, Mr. Kohei Narahara, Mr. Kouichi Nakano, Mr. Ryo Matsuda, Mr. Shunya Naito, Mr. Jun Osawa, Ms. Noriko Fujiki and Ms. Riwako Hosaka.

A heartfelt acknowledgement goes to my parents Tarcisio Tamayo and Margarita Ruiz, and to my girlfriend Kasumi Ichinose whose love, encouragements, patience, and support have been a fundamental pillar to complete this thesis.

I am thankful to Mr. Atsushi Tobita from Sigma Koki Co. Ltd., to Mr. Katsutaka Inazumi from Matsunami Glass Ind. Ltd., and to Ms. Asuka Matsushita from Chemitox Inc. for their support in carrying out tests and providing samples and materials information.

I wish to express my gratitude to the GCOE program and RCAST for the financial support during the first and second year; and to the Atsumi International Foundation for the financial support and various activities during the third year.

This work was supported by the incorporated administrative agency New Energy and Industrial Technology Development Organization (NEDO) and the Ministry of Economy Trade and Industry (METI) of Japan.



# Contents

Abstract.....	i
<i>Acknowledgements .....</i>	<i>v</i>
List of Figures .....	x
List of Tables .....	xviii
<b>1. Introduction.....</b>	<b>1</b>
1.1. Introduction to solar cells.....	2
1.2. Introduction to Concentrator Photovoltaic systems.....	4
1.3. Motivation and outlines .....	5
<b>2. Improving transmission-type Concentrator Photovoltaic system.....</b>	<b>7</b>
2.1. Light Prescriptions Innovators' Ventana CPV system .....	8
2.2. Approach to reduce the reflectance at the optical-elements interfaces ....	9
2.3. RCWA simulations of desirable structures morphology.....	10
2.4. Reducing the dew condensation on POE's back side.....	13
2.4.1. Dew condensation on POE's back side.....	13
2.4.2. Dew condensation on POE's front side .....	14
2.4.3. Hydrophobic functionalization of nanostructured surface .....	15
<b>3. Fabrication methods on glass and PMMA substrates.....</b>	<b>17</b>
3.1. Previous researches on antireflection methods for flat glass surfaces ...	18
3.2. Maskless plasma etching on glass.....	23
3.2.1. Background of plasma etching .....	25
3.2.2. Composition of B270 glass and other employed glasses.....	26

3.2.3.	Optical properties.....	27
3.2.4.	Surface morphology by AFM .....	33
3.2.5.	Surface morphology and composition by XPS and SEM-EDX .....	34
3.2.6.	Cross section morphology and composition by STEM-EDX.....	38
3.2.7.	Aspect ratio tunability and fabrication process .....	42
<b>3.3.</b>	<b>Maskless plasma etching on various glasses .....</b>	<b>51</b>
3.3.1.	LIBA 2000 glass .....	51
3.3.2.	Na <sub>2</sub> O-free B270 glass .....	53
3.3.3.	Quartz .....	56
3.3.4.	Soda Lime glass.....	57
3.3.5.	D263 glass.....	60
3.3.6.	Qioptiq space cover glasses.....	64
<b>3.4.</b>	<b>Self-generated masks under maskless plasma etching.....</b>	<b>70</b>
<b>3.5.</b>	<b>Optical properties simulations using FDTD and RCWA.....</b>	<b>74</b>
3.5.1.	FDTD and RCWA shape dependence simulations .....	74
3.5.2.	Graded refractive index simulations .....	76
3.5.3.	Comparison between experimental and simulation results.....	78
<b>3.6.</b>	<b>Controllable wettability of nanostructured B270 glass surface .....</b>	<b>79</b>
<b>3.7.</b>	<b>Previous researches on antireflection methods for flat PMMA surfaces</b>	<b>81</b>
<b>3.8.</b>	<b>Maskless and TiO<sub>2</sub>-assisted plasma etching on PMMA substrates .....</b>	<b>82</b>
<b>4.</b>	<b><i>Nanostructuring surfaces of the POE and SOE.....</i></b>	<b>87</b>
<b>4.1.</b>	<b>Texturing the flat and corrugated surfaces of LPI's PMMA POE.....</b>	<b>88</b>
4.1.1.	Optical properties.....	88
4.1.2.	Field tests .....	90
<b>4.2.</b>	<b>Texturing the curved surface of LPI's glass SOE .....</b>	<b>93</b>
4.2.1.	LPI's curved secondary optical element.....	93
4.2.2.	Field tests .....	94
<b>4.3.</b>	<b>CPV module with all textured interfaces.....</b>	<b>96</b>
4.3.1.	Field tests .....	96
<b>4.4.</b>	<b>Hydrophobic coating.....</b>	<b>97</b>
4.4.1.	PMMA substrates.....	97
4.4.2.	Primary optical element of UT CPV system .....	99

4.5.	<b>Nanostructured surfaces' effect on the Fill Factor .....</b>	<b>102</b>
4.5.1.	EQE measurement of 3JSC below bare and textured substrates.....	102
4.5.2.	Irradiance and spectral homogeneity effect .....	105
<b>5.</b>	<b><i>Applications of this research in other fields .....</i></b>	<b>107</b>
<b>5.1.</b>	<b>Flat PV .....</b>	<b>108</b>
5.1.1.	Quantum-Dot solar cells below glass substrates .....	108
5.1.2.	Quantum-Dot solar cells below PMMA substrates .....	111
<b>5.2.</b>	<b>Cover glasses for solar cells in space .....</b>	<b>113</b>
<b>5.3.</b>	<b>Aspheric lenses.....</b>	<b>113</b>
<b>6.</b>	<b><i>Summary and outlook.....</i></b>	<b>115</b>
<b>7.</b>	<b><i>Bibliography .....</i></b>	<b>119</b>
	<b><i>Publications and achievements.....</i></b>	<b>125</b>

## List of Figures

Fig. 1.1. Detailed balance efficiency limit for single junction solar cells under 1 sun and 1000 suns incident light. Figure is from Ref. [2] .....	2
Fig. 1.2. Research cell efficiency records as of January 20th 2014, National Renewable Energy Laboratory, US. Figure is from Ref. [9].....	3
Fig. 1.3. Example of triple junction solar cell and representation of the portion of the AM 1.5 spectrum that each cell absorbs. Figure is from Ref. [10].....	3
Fig. 1.4. Detailed balance efficiency limit for multi-junction solar cells under one sun or concentration dependence. Figure is from Ref. [11].....	4
Fig. 1.5. Schematic comparison of flat panel and different concentrator photovoltaic systems. Figure is from Ref. [14].....	5
Fig. 1.6. Characteristics of the optical elements in transmission CPV system considered to design the approach to reduce their reflectance. Figure in the middle if from Ref. [13].....	6
Fig. 2.1. 3D and 2D views of LPI's four-fold Fresnel Kohler concentrator system. Yellow arrows indicate the reflections at the Air/Optical elements interfaces. Figure is from Ref. [13].....	8
Fig. 2.2. Requirements and research flow in order to reduce the reflectance at the three interfaces of the optical elements in transmission-type CPV systems.	10
Fig. 2.3. Flat (left) and periodically textured (right) PDMS interfaces simulated using RCWA.....	11
Fig. 2.4. $J_{sc}$ improvement of structured PDMS compared to flat PDMS at normal incidence. ....	12
Fig. 2.5. $J_{sc}$ angle dependence improvement of structured PDMS (Period = 100 nm) compared to flat PDMS. ....	13
Fig. 2.6. Dew accumulation on the inner-side of Daido Steel's POE (left) and its	

effect on the module output throughout the day (right). Figures are from Ref. [24].	14
Fig. 2.7. Power plant output effect of dew accumulation on the outer-side of Soitec's POE. Figure is from Ref. [25].	14
Fig. 3.1. Schema of deposition system (left) and reflectance spectra with and without universal visible AR on various glasses (right). Figures are from Ref. [26].	18
Fig. 3.2. Effective refractive index dependence (left) and porosity dependence (right) on the deposition angle. Figures are from Ref. [28].	19
Fig. 3.3. Nanoimprint process flow and SEM images of the mold and imprinted surface (left) and measured and simulated transmittance spectra (right). Figures are from Ref. [27].	19
Fig. 3.4. Fabrication process steps of periodic tapered high aspect ratio nanostructures on fused silica using lithography and plasma etching. The white bars represent 200 nm and the figure is from Ref. [29].	20
Fig. 3.5. Averaged TE and TM transmittance spectra at different angles of incidence on both-sides patterned fused silica. Figure is from Ref. [29].	20
Fig. 3.6. Fabrication of antireflection nanostructures on borosilicate glass metallic layer deposition, thermal dewetting, and plasma etching (left) and dependence of the morphology and transmittance spectra on the thickness of the deposited metallic layer (right). All figures are from Ref. [40].	21
Fig. 3.7. Nanopillars on quartz substrates obtained by using three types of PMMA layers and subsequent self-generated mask formation and plasma etching (left) and transmittance spectra of each nanostructured surface (right). All figures are from Ref. [35].	22
Fig. 3.8. Summary of the literature review on glass nano-microstructuration by maskless or assistance mask plasma etching obtaining antireflection or scattering on various types of glasses.	24
Fig. 3.9. Schema of the processes in plasma etching and the role of the mask. Figure is from Ref. [53].	25
Fig. 3.10. Optical setup built to obtaining a collimated beam to evaluate the optical properties of nanostructured glass and PMMA substrates and lenses.	28
Fig. 3.11. Transmittance spectra after $\text{CHF}_3$ (40 min) and $\text{O}_2$ (10 min) plasma etching, deionized water rinsing, and SPM processes on one and both sides of B270 glass.	29
Fig. 3.12. Transmittance angle of incidence dependence spectra from $0^\circ$ to $60^\circ$	

on bare B270 substrate.....	30
Fig. 3.13. Transmittance angle of incidence dependence spectra from 0° to 60° on B270 substrate after CHF <sub>3</sub> (40 min) and O <sub>2</sub> (10 min) plasma etching, and deionized water rinsing on one side. ....	31
Fig. 3.14. Transmittance angle of incidence dependence spectra from 0° to 60° on B270 substrate after CHF <sub>3</sub> (40 min) and O <sub>2</sub> (10 min) plasma etching, and deionized water rinsing on both sides. ....	31
Fig. 3.15. Transmittance angle of incidence dependence spectra at 600 nm from 0° to 60° on bare B270 substrate, and after CHF <sub>3</sub> (40 min) and O <sub>2</sub> (10 min) plasma etching, and deionized water rinsing on one and both sides.....	32
Fig. 3.16. AFM images of bare B270 substrate (left), after CHF <sub>3</sub> (40 min) and O <sub>2</sub> (10 min) plasma etching processes (right), and after subsequent 10 min SPM process. The white bar represents 1μm. ....	33
Fig. 3.17. AFM images of the nanostructured surface after 40 min CHF <sub>3</sub> plasma etching (left) and after subsequent 1 min (middle) and 10 min (right) O <sub>2</sub> plasma etching. ....	34
Fig. 3.18. XPS spectra carried out on bare B270 substrates and after the CHF <sub>3</sub> (40 min) and O <sub>2</sub> (10 min) plasma etching, deionized water rinsing, and SPM processes.....	35
Fig. 3.19. SEM-EDX spectra on the textured surface (black) and focused on the NaF cubic crystal (red). The inset shows a SEM image of the textured surface and the NaF cubic crystal. ....	36
Fig. 3.20. SEM image of B270 glass after 25 (left) and 80 (right) min CHF <sub>3</sub> plasma etching showing the presence and permanence of NaF crystals on the surface. ....	37
Fig. 3.21. SEM cross-section images of B270 after 40 min CHF <sub>3</sub> (left) and subsequent 10 min O <sub>2</sub> (right) plasma etching.....	37
Fig. 3.22. STEM cross-section image of B270 after 40 min CHF <sub>3</sub> plasma etching (top) and STEM-EDX spectra on two areas and points of the cross-section (bottom).....	38
Fig. 3.23. STEM cross section image of B270 after 40 min CHF <sub>3</sub> plasma etching a). Elements distribution images of O b), F c), Si d), Ca e), and Na f) obtained by STEM-EDX on the a). The white bar represents 500 nm.....	40
Fig. 3.24. Etching depth on B270 and quartz after 1 to 80 min CHF <sub>3</sub> plasma etching using a protective 300-nm-thick Aluminum mask and measured by DekTak after removing it.....	42

Fig. 3.25. Transmittance spectra dependence on the CHF <sub>3</sub> plasma etching time from 1 to 80 min. ....	43
Fig. 3.36. Transmittance spectra dependence on the CHF <sub>3</sub> plasma etching time from 1 to 80 min. Subsequent 10 min O <sub>2</sub> plasma etching was applied on all samples.....	44
Fig. 3.27. Transmittance spectra dependence on the CHF <sub>3</sub> plasma etching time from 1 to 80 min. Subsequent 10 min O <sub>2</sub> plasma etching and deionized water rinsing were applied on all samples. ....	44
Fig. 3.28. SEM images of the nano-pillars aspect ratio dependence on the CHF <sub>3</sub> plasma etching time from 20 to 80 min.....	45
Fig. 3.29. Approximated pillar height measured on the SEM images of B270 substrates after CHF <sub>3</sub> plasma etching from 20 to 80 min. ....	46
Fig. 3.30. Model of the surface nanostructuration process using CHF <sub>3</sub> plasma etching on B270 glass, based on the XPS, STEM-EDX, Dektak, and SEM results. ....	47
Fig. 3.31. Transmittance spectra and cross-section images of “Tapered” and “Pillar” nanostructures obtained after CHF <sub>3</sub> (40 min) plasma etching. Subsequent 10 min O <sub>2</sub> plasma etching and deionized water rinsing were applied on both samples.....	48
Fig. 3.32. Transmittance spectra and cross-section images of “Tapered” and “Pillar” nanostructures obtained after CHF <sub>3</sub> (80 min) plasma etching. Subsequent 10 min O <sub>2</sub> plasma etching was applied on both samples. ....	49
Fig. 3.33. Transmittance spectra and cross-section images of bare B270 substrates and after CHF <sub>3</sub> (40 min) and O <sub>2</sub> (10 min) plasma etching using a different RIE machine and at two lower RF power conditions.....	50
Fig. 3.34. Transmittance spectra after CHF <sub>3</sub> (40 min) and O <sub>2</sub> (10 min) plasma etching, and deionized water rinsing processes on one side of LIBA 2000 glass. ....	51
Fig. 3.35. AFM images of bare LIBA 2000 substrates (left) and after CHF <sub>3</sub> (40 min) and O <sub>2</sub> (10 min) plasma etching processes (right). The white bar represents 1μm.....	52
Fig. 3.36. Picture of the 200 g Na <sub>2</sub> O-free B270 sample just after fabrication and before cutting and polishing it for testing the role of CaO alone.....	53
Fig. 3.37. Transmittance spectra after CHF <sub>3</sub> (40-80 min) and O <sub>2</sub> (10 min) plasma etching, and deionized water rinsing processes on one side of Na <sub>2</sub> O-free B70 substrates. ....	54
Fig. 3.38. AFM images of bare Na <sub>2</sub> O-free B70 substrates (left), after CHF <sub>3</sub> (40	

min) and O <sub>2</sub> (10 min) (middle), and after CHF <sub>3</sub> (80 min) and O <sub>2</sub> (10 min) (right) plasma etching processes. The white bar represents 1μm. ....	55
Fig. 3.39. AFM images of bare quartz substrates (left) and after CHF <sub>3</sub> (40 min) and O <sub>2</sub> (10 min) plasma etching processes (right). The white bar represents 1μm.....	56
Fig. 3.40. XPS spectra carried out on quartz substrates before and after the CHF <sub>3</sub> (40 min) and O <sub>2</sub> (10 min) plasma etching processes. ....	56
Fig. 3.41. Transmittance spectra after CHF <sub>3</sub> (40 min) and O <sub>2</sub> (10 min) plasma etching on one side of soda lime glass. ....	57
Fig. 3.42. AFM images of bare Soda Lime substrates (left) and after CHF <sub>3</sub> (40 min) and O <sub>2</sub> (10 min) plasma etching processes (right). The white bar represents 1μm.....	58
Fig. 3.43. SEM image of the surface of Soda Lime after 40 min CHF <sub>3</sub> plasma etching.....	59
Fig. 3.44. XPS spectra carried out on Soda Lime substrates before and after the CHF <sub>3</sub> (40 min) and O <sub>2</sub> (10 min) plasma etching processes. ....	60
Fig. 3.45. Transmittance and diffuse reflectance spectra after CHF <sub>3</sub> (40 min) and O <sub>2</sub> (10 min) plasma etching on one side of D263 glass.....	61
Figure 3.47 shows an enlarged SEM image of the large size structures on the treated D263 surface after 40 min CHF <sub>3</sub> plasma etching that originated the scattering effect. It has been reported that the scattering properties can be tuned by adjusting the plasma etching parameters or the assistance mask characteristics to achieve desired scattering properties that can be applied to improve solar cells, OLEDs, or other applications [44, 49].....	61
Fig. 3.46. AFM images of bare D263 substrates (left) and after CHF <sub>3</sub> (40 min) and O <sub>2</sub> (10 min) plasma etching processes (right). The white bar represents 1μm.....	62
Fig. 3.47. SEM image of the surface of D263 after 40 min CHF <sub>3</sub> plasma etching. ....	62
Fig. 3.48. XPS spectra carried out on D263 substrates before and after the CHF <sub>3</sub> (40 min) and O <sub>2</sub> (10 min) plasma etching processes. ....	63
Fig. 3.49. Transmittance spectra of bare CMG substrate, CMG substrates using typical AR coating, and after CHF <sub>3</sub> (40 min), O <sub>2</sub> (10 min) plasma etching, and deionized water rinsing processes on one side. ....	64
Fig. 3.50. Transmittance spectra of bare CMX substrate, CMX substrates using typical AR coating, and after CHF <sub>3</sub> (40 min), O <sub>2</sub> (10 min) plasma etching,	



and deionized water rinsing processes on one side. ....	65
Fig. 3.51. Transmittance spectra of bare CMO substrate, CMO substrates using typical AR coating, and after $\text{CHF}_3$ (40 min), $\text{O}_2$ (10 min) plasma etching, and deionized water rinsing processes on one side. ....	65
Fig. 3.52. AFM images of bare CMG substrates (left) and after $\text{CHF}_3$ (40 min), $\text{O}_2$ (10 min) plasma etching and deionized water rinsing processes (right). The white bar represents $1\mu\text{m}$ . ....	66
Fig. 3.53. AFM images of bare CMX substrates (left) and after $\text{CHF}_3$ (40 min), $\text{O}_2$ (10 min) plasma etching and deionized water rinsing processes (right). The white bar represents $1\mu\text{m}$ . ....	67
Fig. 3.54. AFM images of bare CMO substrates (left) and after $\text{CHF}_3$ (40 min), $\text{O}_2$ (10 min) plasma etching and deionized water rinsing processes (right). The white bar represents $1\mu\text{m}$ . ....	67
Fig. 3.55. XPS spectra carried out on bare CMG substrates and after $\text{CHF}_3$ (40 min), $\text{O}_2$ (10 min) plasma etching, and deionized water rinsing processes. ....	68
Fig. 3.56. XPS spectra carried out on bare CMX substrates and after $\text{CHF}_3$ (40 min), $\text{O}_2$ (10 min) plasma etching, and deionized water rinsing processes. ....	69
Fig. 3.57. XPS spectra carried out on bare CMO substrates and after $\text{CHF}_3$ (40 min), $\text{O}_2$ (10 min) plasma etching, and deionized water rinsing processes. ....	69
Fig. 3.58. Geometry of the Pillar and Tapered nanostructures simulated using FDTS and RCWA. ....	74
Fig. 3.59. FDTD and RCWA simulation results of Pillar and Tapered nanostructures with height from 100 to 500 nm. ....	75
Fig. 3.60. Graded refractive index profile from 1.2 to 1.5 using 100 layers. ....	76
Fig. 3.61. RCWA simulation results of Pillar and Tapered nanostructures with constant and graded refractive index and height from 100 to 500 nm. ....	77
Fig. 3.62. Comparison between experimental and RCWA simulation results of Tapered nanostructures with 100 and 450 nm in height. ....	78
Fig. 3.63. Top (left) and oblique (right) images of water droplets on nanostructured fused silica with as-fabricated hydrophilic and functionalized hydrophobic wettability properties. Figure is from Ref. [29]. ....	79
Fig. 3.64. Contact angle measurements of the structured quartz surface. Prepared using (a) on nanostructures on quartz fabricated using PMMA with different thicknesses and plasma etching. Figure is from Ref. [35]. ....	79
Fig. 3.65. Deionized water contact angle on bare and nanostructured B270 substrates on three conditions: Reference, SPM, and SPM + FDTS. ....	80

Fig. 3.66. SEM top and cross-section images of porous films achieved by copolymer films and removal of the PMMA domains having different weight percentages and achieving different effective refractive indexes. White bar represents 200 nm and figure is from Ref. [68].....	81
Fig. 3.67. Reflectance spectra of one-side antireflection treatment polycarbonate and PMMA using solgel, ion-assisted deposition, and sputtering. Figure is from Ref. [69].....	82
Fig. 3.68. Schema of the equipment used at Fraunhofer IOF to fabricate antireflection nanostructured surfaces on PMMA by maskless and TiO <sub>2</sub> assisted plasma etching processes. Figure is from Ref. [21].....	83
Fig. 3.69. SEM images of structure 1 and structure 2 on PMMA surface (left) and their transmittance and reflectance spectra (right). Figure is from Ref. [19].....	83
Fig. 3.70. Transmittance spectra of bare and on PMMA substrates treated with S1 or S2 on one or both sides.....	84
Fig. 3.71. Transmittance ratio of bare and on PMMA substrates treated with S1 or S2 on one or both sides. ....	85
Fig. 4.1. Schema of the Fresnel lenses characterization in which a 5 mm collimated beam scanned a rectangular section on one of the 4-fold parts. ....	88
Fig. 4.2. Transmittance spectra of a 5 x 80 mm <sup>2</sup> section of bare Fresnel lens and the ones having structure S1 on one side, and S2 on one and both sides. ....	89
Fig. 4.3. Image of LPI's Ventana CPV system depicting the characterization of S1 and S2 nanostructuring methods applied on one and both sides of the PMMA Fresnel lenses.....	90
Fig. 4.4. Field tests Current-Voltage curves obtained using a bare Fresnel lens (blue), and the one having S2 on both sides (red). ....	91
Fig. 4.5. $J_{sc}$ and efficiency relative gains obtained on Fresnel lenses with S1 and S2 on one or both sides. ....	92
Fig. 4.6. Image of the textured SOEs with Spectrolab C3MJ+ solar cells encapsulated below them before field tests.....	93
Fig. 4.7. Image of LPI's Ventana CPV system depicting the characterization of the nanostructuring process on the SOEs.....	94
Fig. 4.8. $J_{sc}$ and efficiency relative gains measured at two different times on SOEs treated during 80 min with CHF <sub>3</sub> plasma etching using RF power 1000W (SOE1) and 800W (SOE2).....	95
Fig. 4.9. $J_{sc}$ and efficiency relative gains measured every 5-10 min from 11:38	

to 12:45 on October 7 <sup>th</sup> in Madrid, Spain using Fresnel lens with S2 on both sides and SOE2. ....	96
Fig. 4.10. Oblique images of water droplets on bare (top), S2 (middle), and hydrophobic functionalized S2 (bottom) PMMA surfaces. ....	97
Fig. 4.11. Transmittance spectra on bare, S2, and hydrophobic functionalized S2 on PMMA substrates. ....	98
Fig. 4.12. Transmittance ratio of bare, S2, and hydrophobic functionalized S2 on PMMA substrates.....	98
Fig. 4.13. Transmittance spectra of a 10 x 50 mm <sup>2</sup> section of bare (top) Fresnel lens and the ones having S2 (middle), and hydrophobic functionalized S2 (bottom) on the back-side.....	99
Fig. 4.14. Image of UTCPV system depicting the characterization of S2 and hydrophobic functionalized S2 back side of PMMA Fresnel lenses.....	100
Fig. 4.15. Field tests Current-Voltage curves obtained using a bare Fresnel lens (blue), and the ones having S2 (red), and hydrophobic functionalized S2 (green) on the back-side.....	101
Fig. 4.16. EQE of each sub-cell without PMMA substrate, below bare PMMA substrate, and below PMMA substrate with S2 on both sides.....	102
Fig. 4.17. EQE and Transmittance ratio comparison between bare PMMA substrate and PMMA substrate with S2 on both sides.....	103
Fig. 4.18. Irradiance distribution on each sub-cell for different types of CPV systems at normal incidence and at 0.6° OFF-AXIS. Figures are from Ref. [12]. ....	105
Fig. 4.19. Current-Voltage curves calculations based on the irradiance distributions on each sub-cell for different types of CPV systems at normal incidence and at 0.6° OFF-AXIS. Figures are from Ref. [12]. ....	105
Fig. 5.1. Image of the treated glass substrates placed 4 cm above the InGaAs / GaAsSb QDSC during EQE measurements.....	108
Fig. 5.2. Transmittance spectra of the bare glass substrates and after CHF <sub>3</sub> (left) and subsequent O <sub>2</sub> (right) plasma etching processes.....	109
Fig. 5.3. EQE measurements of an InGaAs / GaAsSb QDSC placed 4 cm below the bare and textured substrates. ....	109
Fig. 5.4. Ratio between the EQE of the InGaAs / GaAsSb QDSC placed below the textured substrates and the bare glass.....	110
Fig. 5.5. EQE measurements of an InGaAs / GaAsSb QDSC placed 6 cm below the bare and textured substrates. ....	111

Fig. 5.6. Transmittance and EQE enhancements of textured PMMA substrates compared to bare one. ....	113
Fig. 5.7. Sigma Koki's Aspheric Condenser Lenses. Figure is from Ref. [70]. .	114
Fig. 5.8. Transmittance spectra of bare (left), after CHF <sub>3</sub> (40 min) and O <sub>2</sub> (10 min) plasma etching (middle), and after water rinsing (right) processes on the curved side of Sigma Koki's AGL-30-23.5P lenses. ....	114

## List of Tables

Table 1. MSDS composition data of B270, D263, and soda-lime glasses. ....	27
Table 2. Summarized transmittance difference at 0° and 60° at 600 nm on Bare B270 substrate, and after CHF <sub>3</sub> (40 min) and O <sub>2</sub> (10 min) plasma etching, and deionized water rinsing processes on one and both sides. ....	32
Table 3. Summarized $J_{sc}$ in mA/cm <sup>2</sup> of each sub-cell without PMMA substrate and placed below bare and textured PMMA substrates. The limiting $J_{sc}$ is indicated in red. ....	104
Table 4. Summarized $J_{sc}$ in mA/cm <sup>2</sup> of each sub-cell without PMMA substrate and placed below bare and textured PMMA substrates. The limiting $J_{sc}$ is indicated in red. ....	104
Table 5. Summarized relative and absolute $J_{sc}$ gains of the textured glass substrates compared to the bare one. ....	110
Table 6. Summarized relative and absolute $J_{sc}$ gains of the textured PMMA substrates compared to the bare one. ....	112

# **Chapter 1**

## **1. Introduction**

## 1.1. Introduction to solar cells

Solar cells can convert solar energy into electricity [1]. The first example is single junction solar cells, which efficiency limit depends on the band-gap of the material it is made of as shown in Fig. 1.1. Figure 1.1 also shows that with concentration, for example 1000 suns, the efficiency limit can be increased. This is due because the short circuit current ( $J_{sc}$ ) increases linearly with concentration, whereas the open circuit voltage ( $V_{oc}$ ) increases logarithmically by the  $J_{sc}$  increase.

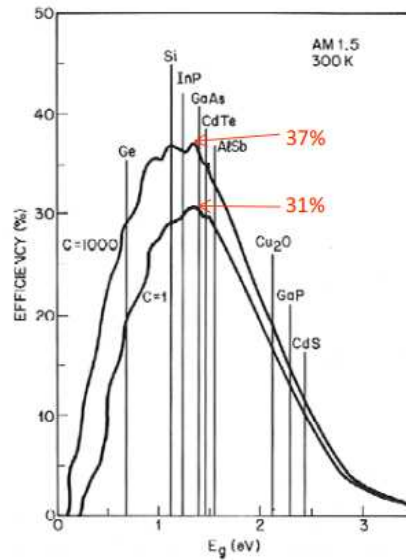


Fig. 1.1. Detailed balance efficiency limit for single junction solar cells under 1 sun and 1000 suns incident light. Figure is from Ref. [2]

Worldwide a great number of universities and research centers have been researching over a great variety of materials and solar cells architectures in order to achieve high efficiency and low cost. Figure 1.2 shows the progress of each type of solar cell over the past 40 years.

There are several approaches that have been proposed in order to further increase the efficiency of solar cells such as multi-junction solar cells [3], intermediate band solar cells [4], hot carriers solar cells [5], up-or down-conversion [6, 7], and multiple exciton generation [8]. In this thesis, for the purpose of presenting the solar cells currently used in CPV systems, only triple junction solar cell is introduced in more detail as shown in Fig. 1.3.

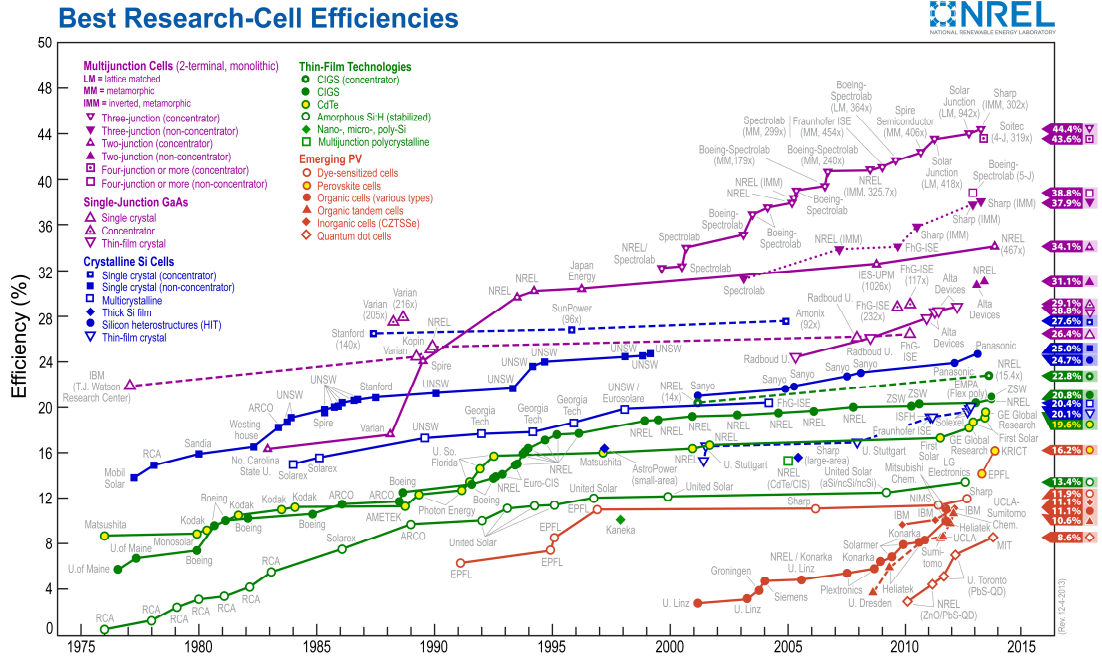


Fig. 1.2. Research cell efficiency records as of January 20th 2014, National Renewable Energy Laboratory, US. Figure is from Ref. [9].

Figure 1.3 shows a series connected type triple junction solar cell (3JSC) grown on Ge substrate. Each sub-cell (Top, Middle, and Bottom) absorbs a portion of the incident solar spectrum as represented in Fig. 1.3 (right). In this 3JSC, the sub-cells are connected in series via a tunnel junction. Therefore, the  $V_{oc}$  of this 3JSC is the sum of the  $V_{oc}$  of each sub-cell and the  $J_{sc}$  is the lowest among the three sub-cells.

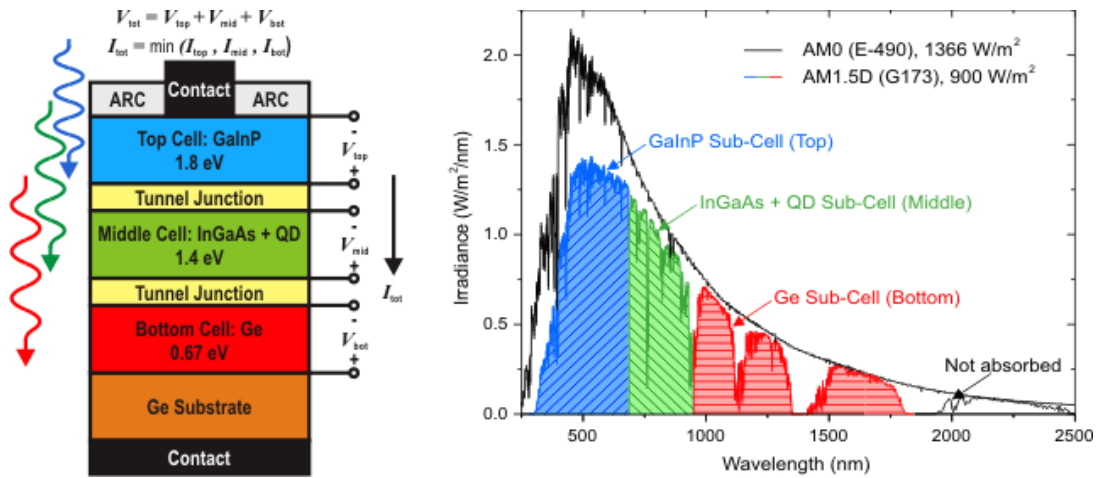


Fig. 1.3. Example of triple junction solar cell and representation of the portion of the AM 1.5 spectrum that each cell absorbs. Figure is from Ref. [10].

## 1.2. Introduction to Concentrator Photovoltaic systems

In the same manner as in single junction solar cells, the efficiency of multi-junction solar cells increases with concentration. Figure 1.4 shows the detailed balance efficiency of solar cells depending on their number of junctions under one sun and under maximum concentration. In practice, solar cells cannot operate under maximum concentration because the high current density and the series resistance of the cell result in overheating, which reduces the solar cell performance.

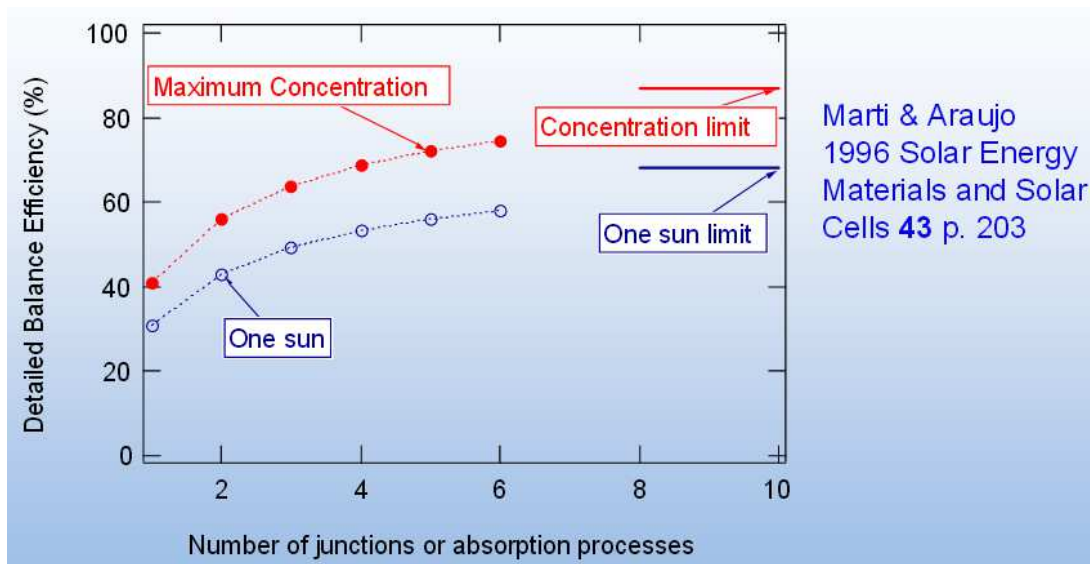


Fig. 1.4. Detailed balance efficiency limit for multi-junction solar cells under one sun or concentration dependence. Figure is from Ref. [11].

Multi-junction solar cells are the main type of solar cells used in CPV systems, typically two or three junction solar cells, but in the future four or more junction solar cells could also be implemented. Figure 1.5 shows various types of CPV technologies compared to flat panel. One particular characteristic of CPV systems is that they need to track the sun, typically using double-axis trackers, because only the direct part of the solar irradiation can be precisely focused on the solar cells. In order to concentrate light into a solar cell a Fresnel lens or a mirror can be used as show in Fig. 1.5 (b, c) and Fig. 1.5 (d, e), respectively. The Fresnel lens or the mirror represents the primary optical element (POE) of the CPV system. In addition to the POE, some CPV systems have a homogenizer or secondary optical element (SOE) as shown in Fig. 1.5 (c, e).



The purpose of the SOE is to uniformize the flux distribution incident to the subjacent solar cell and other optical corrections. A non-uniform spectral or irradiance level distribution reduces the Fill Factor in CPV systems employing multiple junction solar cells [12]. In addition, the use of a SOE allows larger acceptance angle, which partially alleviates the constrain on costly and highly precise tracking systems [13].

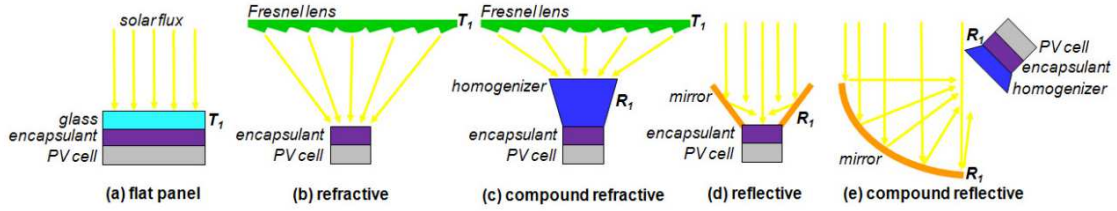


Fig. 1.5. Schematic comparison of flat panel and different concentrator photovoltaic systems. Figure is from Ref. [14].

### 1.3. Motivation and outlines

Currently, the highest efficiency solar cells are based on III-V semiconductor materials. When combined with CPV systems, the efficiency is further increased and the required amount of semiconductor material is decreased, which makes CPV a potential candidate to achieve low cost solar energy [15]. The motivation of this thesis is to reduce the reflectance at the Air/Optical-elements interfaces in transmission CPV systems. For this purpose simulation and fabrication of nanostructured surfaces are performed. As shown in Fig. 1.6, in order to achieve this purpose the nanostructures need to be successfully applied on two materials (PMMA and glass) and on surfaces with different sizes and shapes. In addition, the shape of the nanostructures has to be smaller than the wavelength in order to avoid scattering, which could affect the spectral or the irradiance distribution on the solar cells.

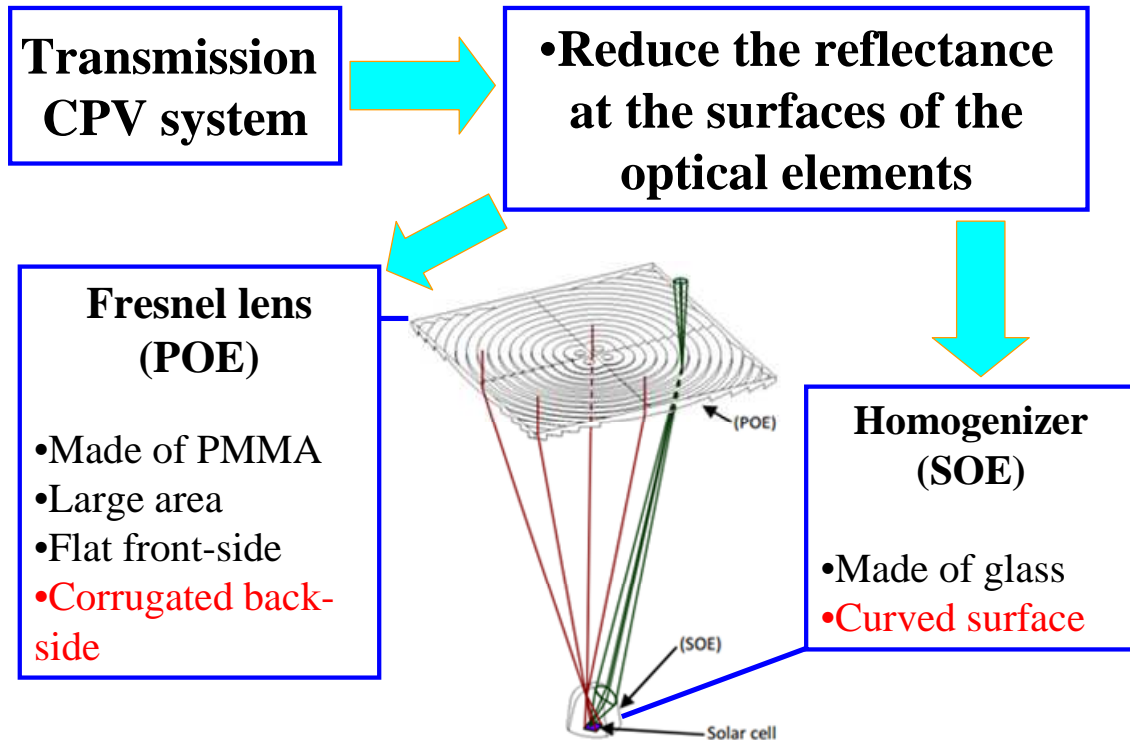


Fig. 1.6. Characteristics of the optical elements in transmission CPV system considered to design the approach to reduce their reflectance. Figure in the middle if from Ref. [13].

# **Chapter 2**

## **2. Improving transmission-type Concentrator Photovoltaic system**

## 2.1. Light Prescriptions Innovators' Ventana CPV system

In this thesis, the Ventana CPV system manufactured by Light Prescription Innovators (LPI), has been implemented to demonstrate the effect of the nanostructured Air/Optical-elements' interfaces. Ventana CPV system is a type of transmission CPV system that employs broken rotational symmetry and Köhler integration design of the POE and SOE achieving high concentration and high acceptance angle [16]. Fig. 2.1 shows the reflections that occur at the Air/Optical-elements' interfaces in a transmission-type CPV system: At first there are two reflections at the Air/Fresnel-lens and Fresnel-lens/Air interfaces (R1), and then there is the reflection at the Air/Homogenizer interface (R2).

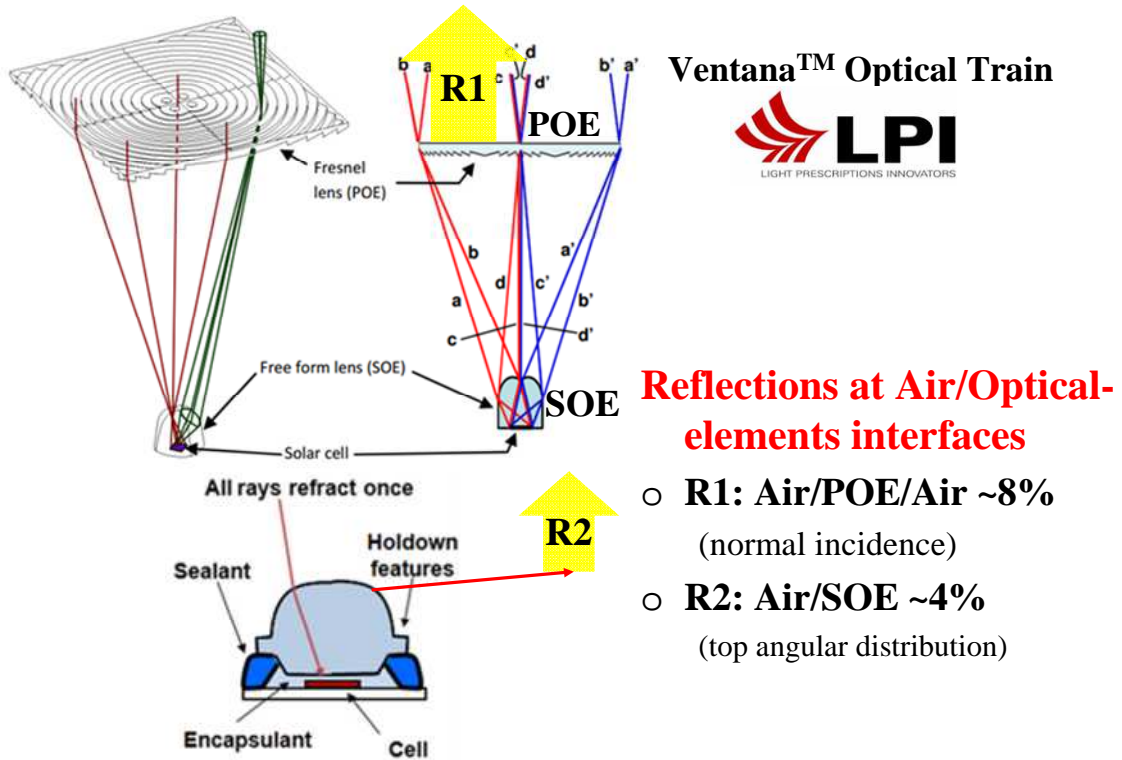


Fig. 2.1. 3D and 2D views of LPI's four-fold Fresnel Köhler concentrator system. Yellow arrows indicate the reflections at the Air/Optical elements interfaces. Figure is from Ref. [13].

The light reaching the top of the homogenizer has an angular distribution which depends on the  $f$ -number of the Fresnel lens employed. In the case of Ventana CPV system, it is equal to 1.43 and the angular distribution at the top of the SOE is  $\pm 20^\circ$ .

A disadvantage of the homogenizer is that it increases the incident angle distribution, which reduces the amount of light harvested by the solar cell because the reflectance increases as the incident angle increases. The effect on the angular distribution reaching the solar cell depends on the type of homogenizer employed [17]. The optical efficiency and the irradiance distribution also depend on the type of SOE employed [18]. In the case of Ventana CPV system, with ideal perfect tracking the angular distribution on the cell is around  $\pm 30^\circ$ , and around  $\pm 40^\circ$  for a tracking error of  $1^\circ$  [13]. In the case of Ventana CPV system, the Fresnel lens is made of Poly (methyl methacrylate) (PMMA) and the homogenizer is made of Glass. The refractive index of both materials is around 1.5, which means that at normal incidence each of these interfaces reflects around 4% of the incident light, in total accounting for around 12% of losses. Due to the angular distribution reaching the homogenizer, the losses at this interface are greater than 4%.

## **2.2. Approach to reduce the reflectance at the optical-elements interfaces**

The surface of the front-side of the POE is flat, the back side has the imprinted corrugations of the Fresnel lens, and the surface of the SOE is curved. Figure 2.2 shows the approach that was implemented in order to nanostructure these three surfaces. In the case of Ventana CPV system, the size of one POE is  $16 \times 16 \text{ cm}^2$  and the size of one large module containing 36 Fresnel lenses is around  $1 \text{ m}^2$ . For this reason, a considerably scalable technique is required in order to be suitable to apply it on the front-and-back side of the POE. As for the SOE in Ventana CPV system, it has a curved front surface, a diameter of 24 mm and height of 22 mm. Figure 2.2 also shows in more detail the SOE's curved surface. Finally, a low cost fabrication method is preferable so that the three interfaces can be nanostructured in a mass production level and have an impact in the CPV industry.

In order to fulfill all the fabrication requirements, plasma etching method was selected. As for PMMA (POE's material), a collaboration was initiated with Fraunhofer Institute for Applied Optics and Precision Engineering (IOF). At Fraunhofer IOF, Prof. Schulz *et al.*, have employed plasma etching to achieve antireflection nanostructures on flat PMMA sheets [19,-21].

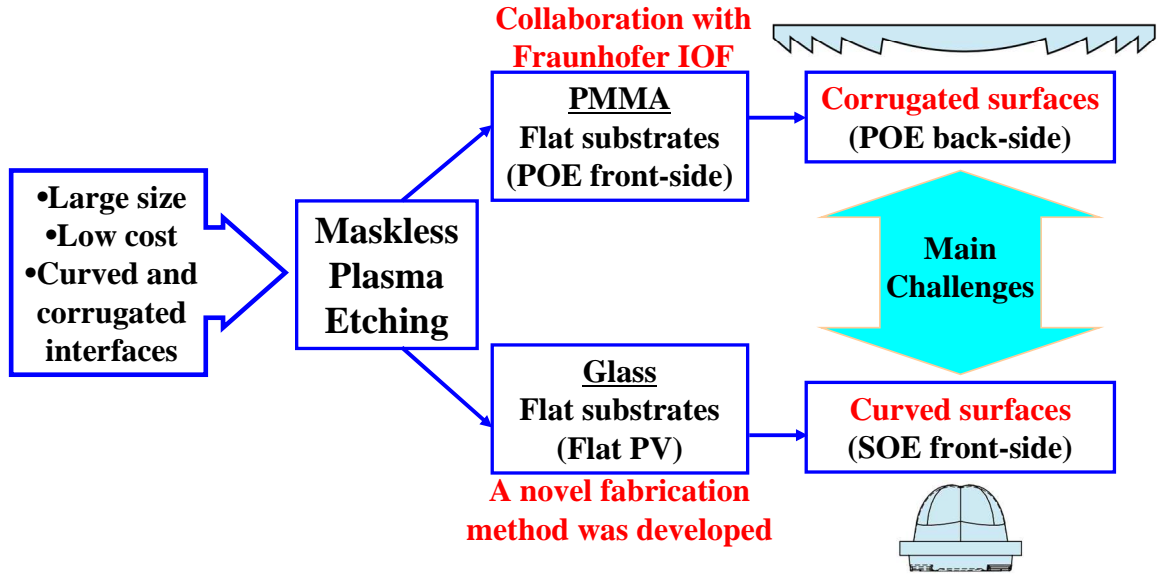


Fig. 2.2. Requirements and research flow in order to reduce the reflectance at the three interfaces of the optical elements in transmission-type CPV systems.

The purpose and novelty of this collaboration was to apply the antireflection nanostructures on the front-and-back sides of a series of POEs and evaluate their performance by transmittance measurements and field tests. Since the back side of the POE has the corrugations of the Fresnel lens, demonstrating the applicability of the PMMA antireflection nanostructures for CPV systems represented a particular interest in this collaboration. As for glass (SOE's material), a novel fabrication method was developed using maskless plasma etching. This fabrication method was initially applied on flat substrates and then on the curved SOE.

Finally, Field tests were carried out in Madrid at LPI-CeDint facilities in which reference bare POE and SOE were measured at the same time with nanostructured POEs and SOEs and the  $J_{sc}$  and efficiency gains were evaluated.

## 2.3. RCWA simulations of desirable structures morphology

Simulations of antireflective structures with weak angular dependence on the incident angle intended for the POE's and SOE's surfaces were carried out using Rigorous Coupled Wave Analysis (RCWA) [22].

## Simulated nanostructures

Wide-angle antireflection effects can be achieved by subwavelength structures [23]. The initial approach to reduce the reflectance at POE's and SOE's surfaces was to use nanoimprint of Poly (dimethylsiloxane) (PDMS) nanostructures. For this reason, PDMS periodic Moth-eye structures were simulated using RCWA to study the reflectance spectra of flat and structured Air/PDMS interfaces. Finally, direct texturing by plasma etching was found to be better suited for the CPV industry, to have better durability, and to be more cost effective. The results obtained for PDMS are analogous for the cases of PMMA and glass textures because the refractive index of PDMS is approximately 1.41, which is very close to the refractive index of PMMA and glass, approximately 1.5.

Rsoft's DiffractMOD package was used to carry out RCWA simulations to study the reflectance spectra of flat and nanostructured Air/PDMS interfaces, which was used to calculate the  $J_{sc}$  of each structure. In these simulations a 300  $\mu\text{m}$  thick single junction GaAs solar cell was considered and the effect of textured PDMS was analyzed. The flat and nanostructured PDMS are shown in Fig. 2.3. The aspect ratio for the periodic structured interfaces is equal to Height/Period. The period of the triangular PDMS structure was varied from 50 nm to 1.5  $\mu\text{m}$  and the aspect ratio from 0.5 to 3 as shown in Fig. 2.4.

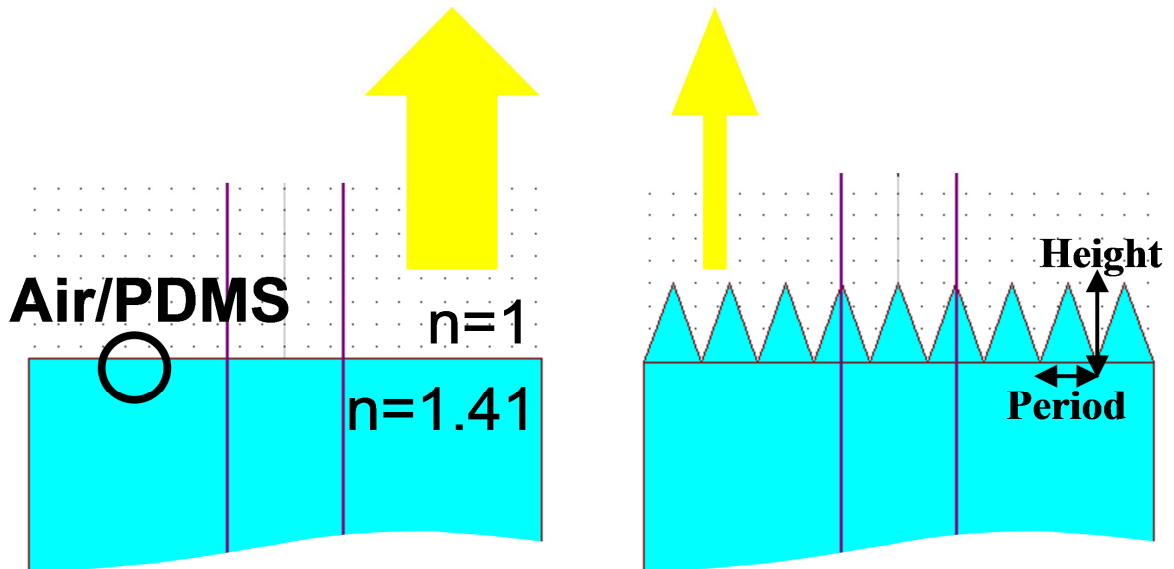


Fig. 2.3. Flat (left) and periodically textured (right) PDMS interfaces simulated using RCWA.

First of all, the reflectance of the flat Air/PDMS interface was simulated to calculate its  $J_{sc}$  and to use it as a reference to normalize the results of the nanostructured case. Also, angular dependence simulations were carried out to assess the performance of each structure regarding the angular distribution coming from the POE.

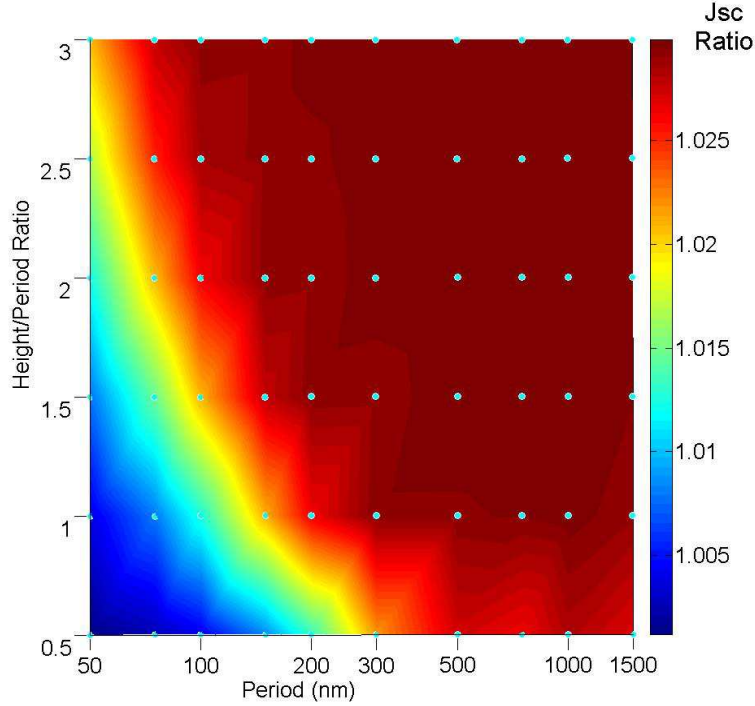


Fig. 2.4.  $J_{sc}$  improvement of structured PDMS compared to flat PDMS at normal incidence.

The maximum improvement at normal incidence of structured PDMS over flat PDMS is 3%. Low diffraction at the Air/optical-elements in R1 and R2 is desirable to avoid scattering. Therefore, a small period is preferred *e.g.* 100 nm, which reaches the maximum improvement with an aspect ratio equal to 3. Such structure could be used on the surfaces of the POE and SOE to reduce the reflectance and maximize the transmitted power. The angle dependence of the reflectance was simulated between 0 and 70° and the dependence of flat PDMS was used to normalize the dependence of structured PDMS of Period equal to 100 nm and with aspect ratio from 1 to 3 as shown in Fig. 2.5. As the aspect ratio increases, the improvement of the structured PDMS increases compared to the flat case; hence a low period and high aspect ratio is the desirable structure for the Air/optical-elements interfaces.



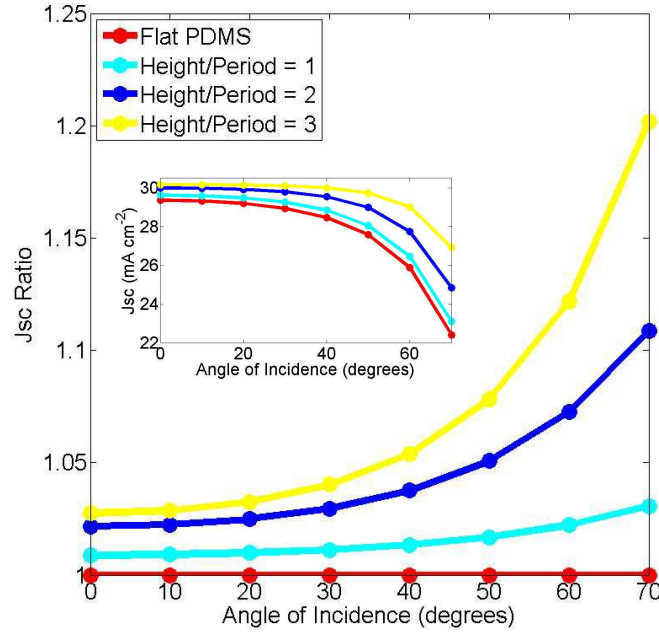


Fig. 2.5.  $J_{sc}$  angle dependence improvement of structured PDMS (Period = 100 nm) compared to flat PDMS.

In CPV systems the incident angle distribution to the SOE depends on the  $f$ -number of the Fresnel lens or mirror employed. The geometry of the SOE can also affect the angle of incidence. The  $J_{sc}$  improvement shown in Fig. 2.5 corresponds to the case where all light is normally incident ( $0^\circ$ ), but the real improvement is greater due to the incident angle distribution. To evaluate the improvement on each type of CPV system, the percentage of light incident at each angle need to be normalized by the angle of incidence dependence shown in Fig. 2.5.

## 2.4. Reducing the dew condensation on POE's back side

### 2.4.1. Dew condensation on POE's back side

Dew condensation on the POE occurs typically after a rainy day or in the morning depending on the humidity of each location. Dew condensation can occur on the front and/or back side of the POE. Daido Steel employs breathing holes in order to avoid dew condensation on POE's back side.

Despite the breathing holes, dew accumulation persists as shown in Fig. 2.6. In an installation at Toyohashi, Japan, the annual CPV energy generated decreased 1.21% in 2004-2005 period and 2% in 2005-2006 period. Figure also shows that as the module is dried up the module output increases [24].

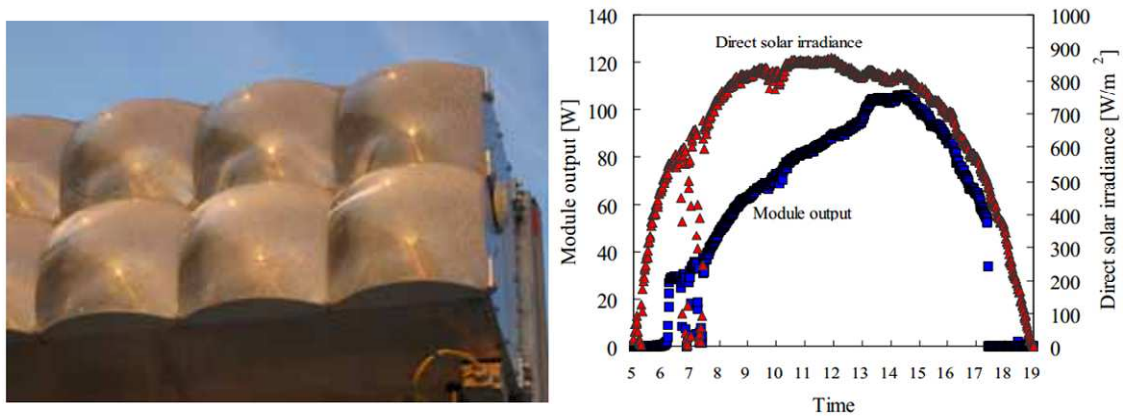


Fig. 2.6. Dew accumulation on the inner-side of Daido Steel's POE (left) and its effect on the module output throughout the day (right). Figures are from Ref. [24].

#### 2.4.2. Dew condensation on POE's front side

In the case of Soitec, despite employing air blow at night in large scale CPV plants, to avoid dew condensation on POE's back side, a slow morning rise in the power generated was observed, which corresponded to dew accumulation on the POE's front side as shown on Fig. 2.7.

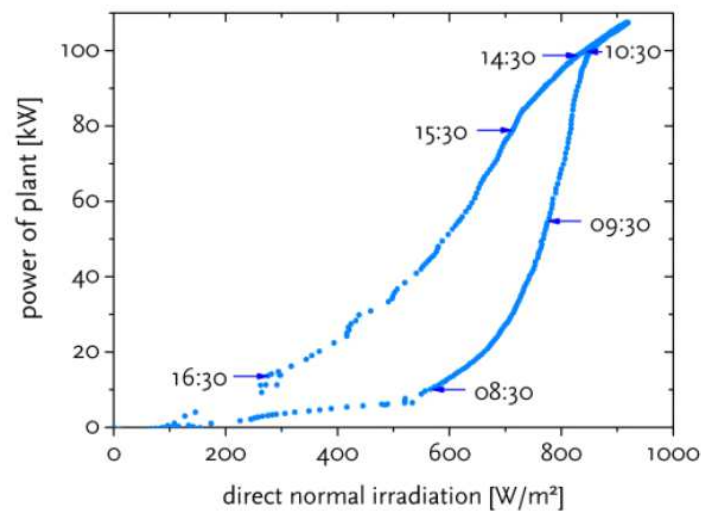


Fig. 2.7. Power plant output effect of dew accumulation on the outer-side of Soitec's POE. Figure is from Ref. [25].

Air blow prevents dew condensation on the POE's back side, but it may represent a significant effect in cost and maintenance and the dew condensation on POE's front side is still unsolved by neither breathing holes nor air blow inside the modules.

### **2.4.3. Hydrophobic functionalization of nanostructured surface**

In order to solve the dew accumulation on the back side of the POE, the application of a hydrophobic coating on the backside of POE was proposed and its realization made part of the collaboration with Fraunhofer IOF. The purpose set was to apply a hydrophobic coating on the antireflection nanostructured surfaces thus achieving higher power generation by increased transmittance and preventing dew accumulation on POE's back side. In order to consider the applicability of this hydrophobic coating to prevent the dew accumulation on POE's front side, the durability of the coating to the outer environment also needs to be evaluated but it is out of the scope of this present study.



# **Chapter 3**

## **3. Fabrication methods on glass and PMMA substrates**

### 3.1. Previous researches on antireflection methods for flat glass surfaces

Glass is a widely used material in optical components for applications ranging from ultraviolet to near-infrared wavelengths. Applications in optics or optoelectronics such as sensors, displays, cover glasses, solar cells, or lenses can be benefited by antireflection. In order to reduce the reflectance, several techniques have been developed such as thin film coatings [26], nanoimprint [27], oblique angle deposition [28], and periodic patterning or moth-eye [29-31]. Simpler methods using sacrificial thin metallic or organic layers, or spheres as mask combined with plasma etching has also been demonstrated on borosilicate glass, fused silica, and quartz [32-39]. The use of a sacrificial mask or thin films with precise thickness, limit the applicability of these techniques to curved surfaces such as lenses, LPI's FK secondary [13] or REhnu's ball lens [40] in concentrator photovoltaic systems.

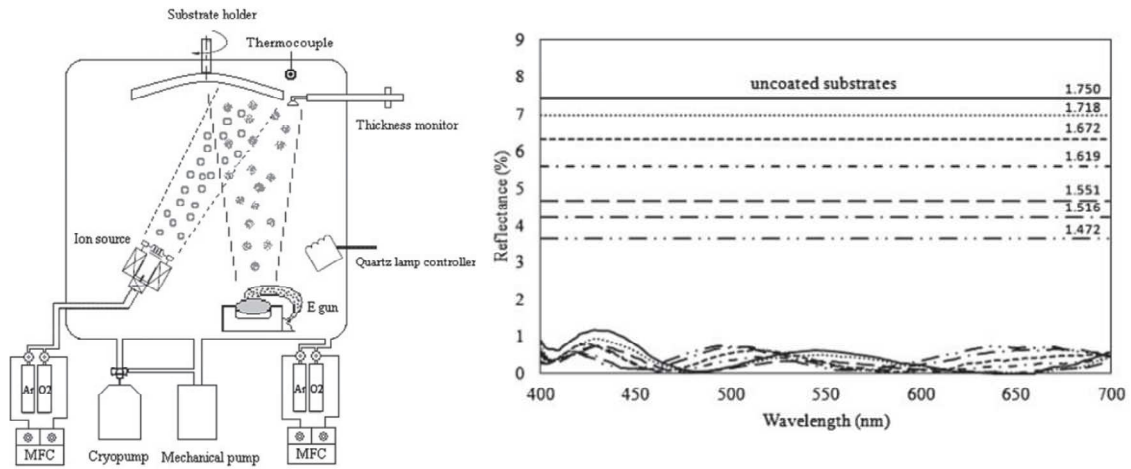


Fig. 3.1. Schema of deposition system (left) and reflectance spectra with and without universal visible AR on various glasses (right). Figures are from Ref. [26].

Figure 3.1 shows the fabrication method and reduction of reflectance by applying thin film antireflection coatings on glasses with different refractive indexes. Thin-film antireflection coatings are effective for narrow spectral ranges and the reflectance rapidly increases outside the optimized range, which limit their applicability for CPV systems because for highest efficiency, broadband antireflection effect is required.

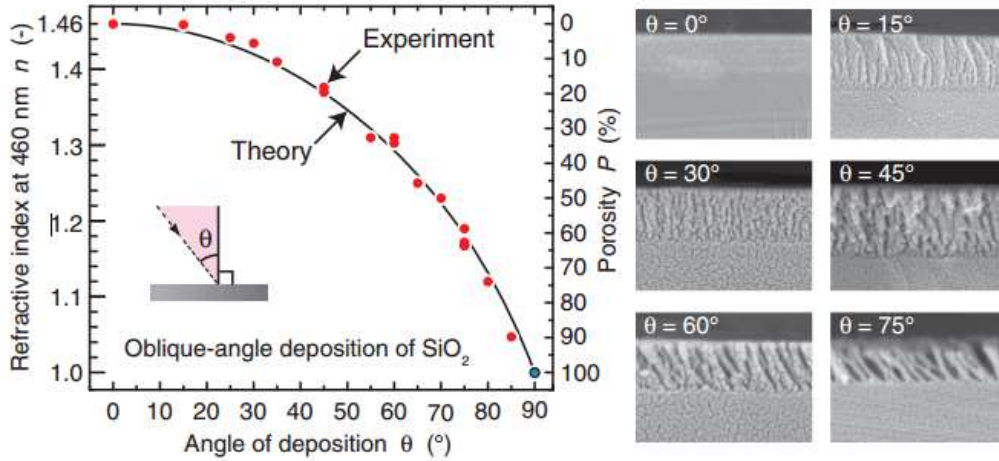


Fig. 3.2. Effective refractive index dependence (left) and porosity dependence (right) on the deposition angle. Figures are from Ref. [28].

Oblique angle deposition relies on angle controllability in order to achieve the desired effective refractive index as shown in Fig. 3.2. The deposition methods of thin film coatings and oblique angle deposition require precise control of the thickness and deposition angle, respectively, which limits their applicability to the curved surface of SOEs in CPV systems.

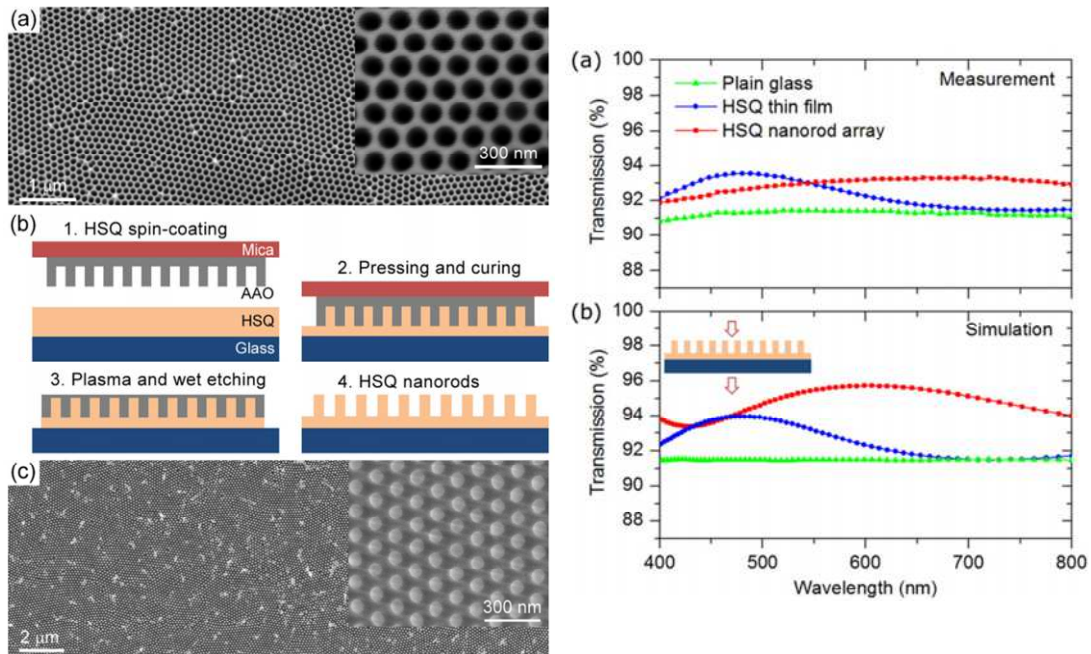


Fig. 3.3. Nanoimprint process flow and SEM images of the mold and imprinted surface (left) and measured and simulated transmittance spectra (right). Figures are from Ref. [27].

Lithography or nanoimprint techniques can achieve controllable, high density, and periodic structures as shown in Fig 3.3 and 3.4, respectively. Nanoimprint relies on a polymer material that is cured by a thermal or UV process. For this reason, small nanostructures with high aspect ratio are more difficult to achieve than by using lithography as the ones shown in Fig. 3.4 (F).

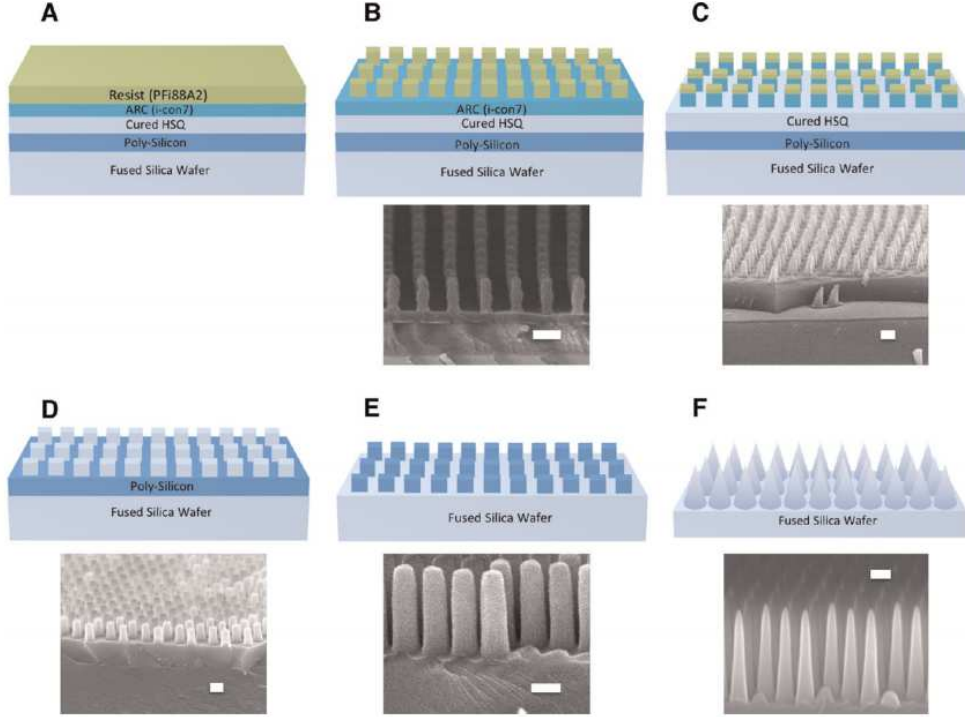


Fig. 3.4. Fabrication process steps of periodic tapered high aspect ratio nanostructures on fused silica using lithography and plasma etching. The white bars represent 200 nm and the figure is from Ref. [29].

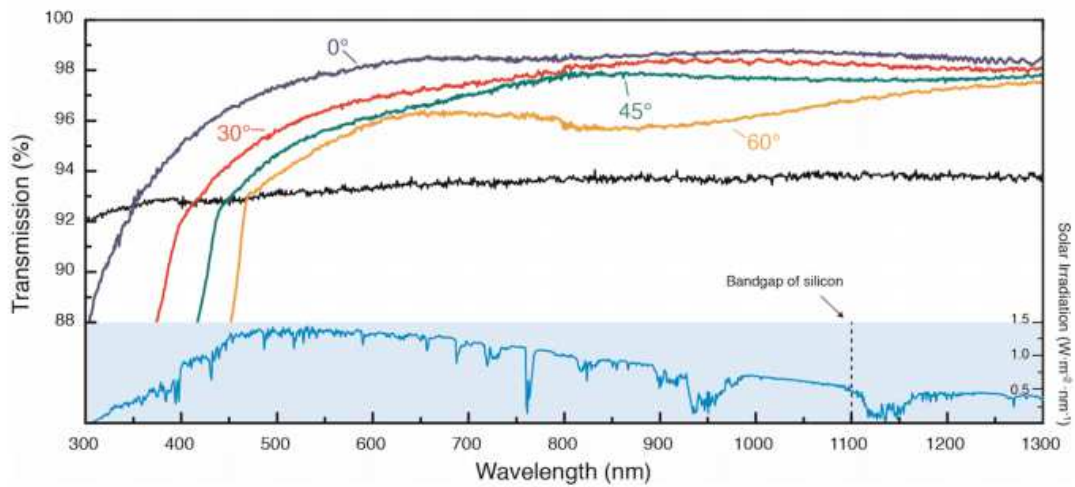


Fig. 3.5. Averaged TE and TM transmittance spectra at different angles of incidence on both-sides patterned fused silica. Figure is from Ref. [29].



The high aspect ratio nanostructures fabricated by lithography on fused silica achieved broadband antireflection effect as shown in Fig. 3.5. Nanoimprint and lithography are promising techniques, but their applicability is limited to small surfaces and are constrained by the cost, and time required for their fabrication.

Lithography-free fabrication methods have also been proposed employing metallic or organic self-generated masks. Fig. 3.6 (left) shows the fabrication of self-generated metallic mask on the glass surface. At first, a Ag or another metallic thin film is deposited; then by thermal dewetting the thin film self-assembles into Ag nanoparticles masks. Finally, these nanoparticles serve as mask to protect the subjacent glass to the plasma etching process resulting in a nanostructured surface. The size and distribution of the Ag nanoparticles, and the obtained nanostructures strongly depend on the thickness of the deposited metallic layer as shown in Fig. 3.6 (right).

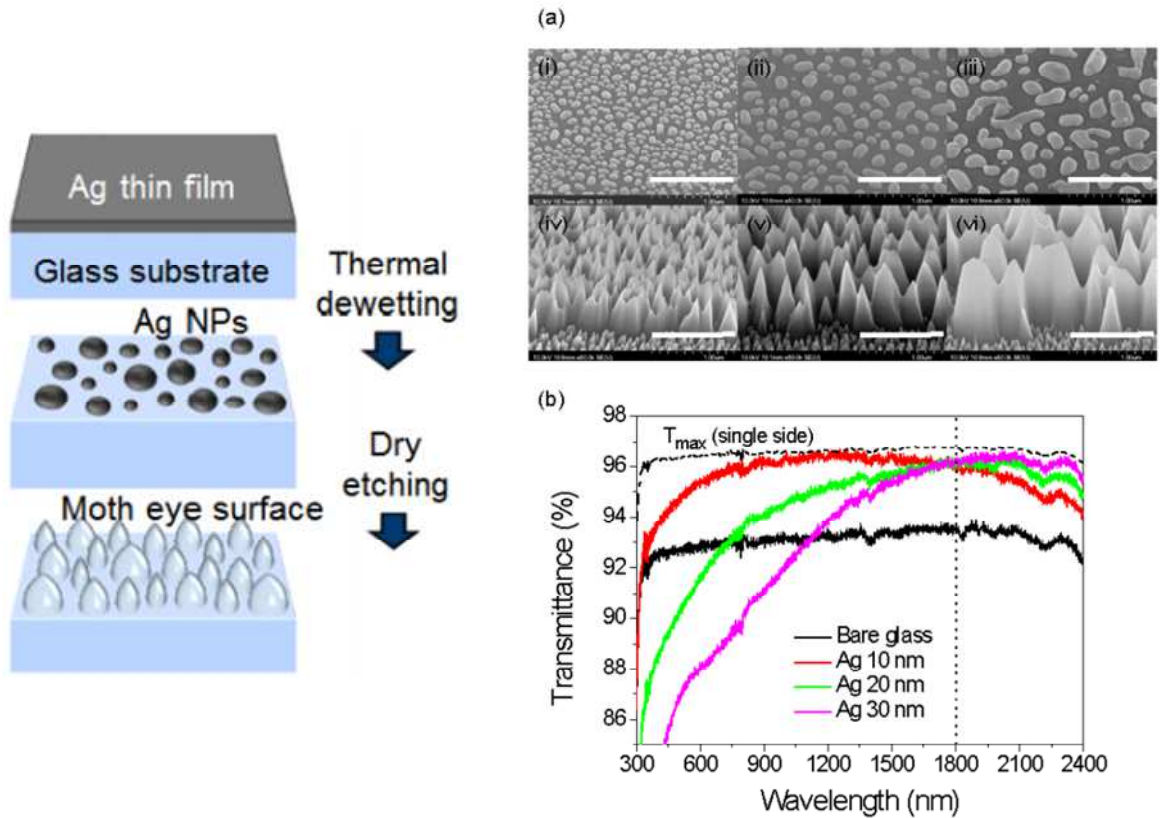


Fig. 3.6. Fabrication of antireflection nanostructures on borosilicate glass metallic layer deposition, thermal dewetting, and plasma etching (left) and dependence of the morphology and transmittance spectra on the thickness of the deposited metallic layer (right). All figures are from Ref. [40].

The surface nanostructuration employing an organic self-generated mask on the surface of quartz is shown in Fig. 3.7. In this process, at first a PMMA layer is deposited on the surface; then under plasma etching PMMA creates a self-generated mask and protects the subjacent glass or quartz to the plasma etching process resulting in a nanostructured surface. The sizes of the obtained nanostructures depend on the thickness of the deposited metallic layer as shown in Fig. 3.6 (right). The expected thicknesses of A2, A8, and A11 are 50, 500, and 800 nm.

The difference between the thickness dependence of the metallic [40] and organic [35] layers deposited in these two studies might be the results of various fabrication parameters as well as the fact that borosilicate glass was employed below metallic mask and quartz below organic mask.

Compared to lithography, lithography-free methods employing metallic or organic self-generated masks can be applied on surfaces with larger area and at lower cost, but due to the need of a deposited layer and the thickness dependence of such layer; their applicability to the curved surface of SOEs in CPV systems is limited.

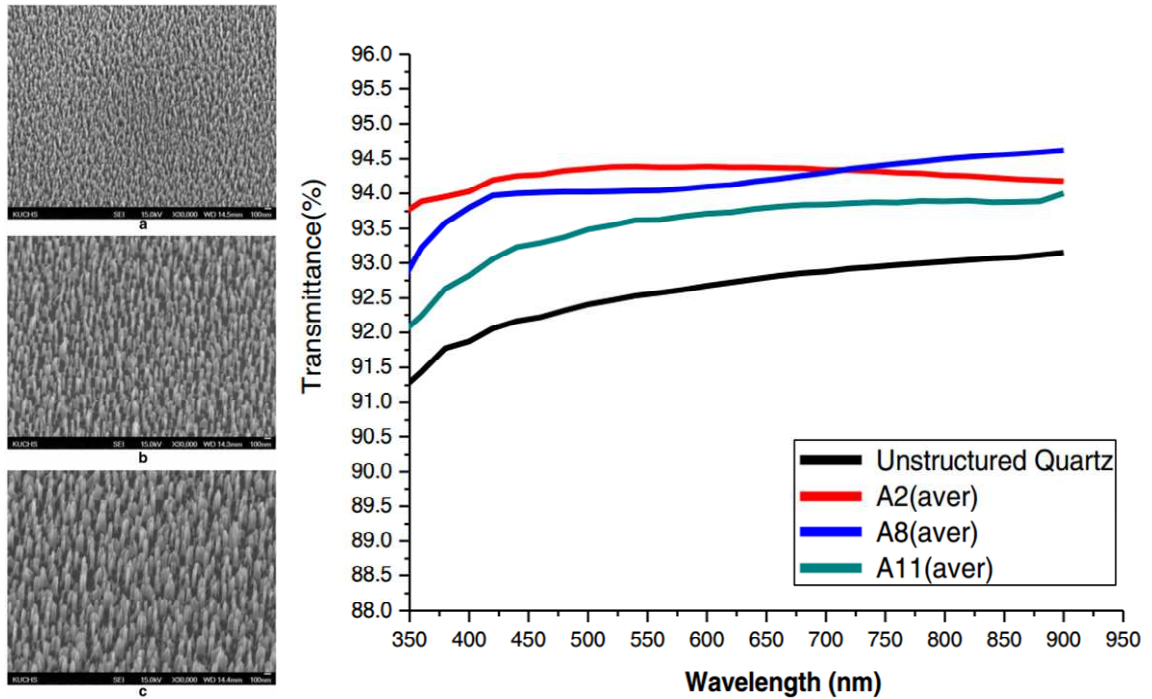


Fig. 3.7. Nanopillars on quartz substrates obtained by using three types of PMMA layers and subsequent self-generated mask formation and plasma etching (left) and transmittance spectra of each nanostructured surface (right). All figures are from Ref. [35].

Scattering surfaces are attractive for applications in lighting engineering and can also enhance the performance of solar cells [41, 42], or OLEDs [43-45] because they randomize the incident  $k$ -vector of the light leading to a light trapping effect [46]. Additionally, they have a variety of other applications including architecture and design. Scattering surfaces on glass can be achieved by wet etching-, heat-, or laser-assisted methods with drawbacks in defects generation, reproducibility, or scalability [42, 47, 48]. Maskless plasma etching fabrication of scattering surfaces has been reported only on borosilicate glass [42, 49]. Employing a metallic or organic assistance-mask, scattering surfaces were also obtained on borosilicate glass, fused silica, and soda-lime glass [50-52].

### **3.2. Maskless plasma etching on glass.**

Fig. 3.8 summarizes the antireflection or scattering properties that have been reported by using maskless or assistance mask plasma etching on various glasses and quartz. When employing an assistance mask prior to plasma etching *i.e.* deposition of a metallic or an organic layer, antireflection effect has been reported on borosilicate glass, on fused silica, and on quartz [32-39]. In a similar process, after depositing a metallic or an organic layer on borosilicate glass and fused silica, scattering effect has been observed [50-52]. Maskless plasma etching has only been reported on borosilicate glass resulting in scattering surface [42, 49].

For the purpose of applicability to the curved surface of SOEs in CPV systems, a novel fabrication process consisting in maskless plasma etching to obtain broadband antireflection effect is needed and it is one of the main directions of the research carried out during this thesis. The absence of deposited mask allows the fabrication on curved surface and the plasma etching process itself is low cost, scalable to large areas, and suitable to current production lines.

	Antireflection	Scattering
Maskless	<ul style="list-style-type: none"> <li>• <b>Novel process by self-generated mask</b></li> <li>• <b>Curved surfaces</b></li> <li>• <b>Large scale</b></li> <li>• <b>Low-cost</b></li> </ul>	<ul style="list-style-type: none"> <li>• <b>Henning Fouckhardt <i>et al.</i>, [42, 49]</b></li> <li>• <b>Borosilicate glass</b></li> </ul>
Assistance Mask	<ul style="list-style-type: none"> <li>• <b>J.K.N. Lindner <i>et al.</i>, Jae Su Yu <i>et al.</i>, Hobbs, D.S. <i>et al.</i>, Jung Suk Kim <i>et al.</i>, [32-39]</b></li> <li>• <b>Mask</b> <ul style="list-style-type: none"> <li>• <u>Organic or metallic</u></li> </ul> </li> <li>• <b>Borosilicate glass, fused silica, quartz</b></li> </ul>	<ul style="list-style-type: none"> <li>• <b>Henning Fouckhardt <i>et al.</i>, [42, 47, 48]</b></li> <li>• <b>Mask</b> <ul style="list-style-type: none"> <li>• <b>Organic or metallic</b></li> </ul> </li> <li>• <b>Borosilicate glass, fused silica</b></li> </ul>

Fig. 3.8. Summary of the literature review on glass nano-microstructuration by maskless or assistance mask plasma etching obtaining antireflection or scattering on various types of glasses.

To our knowledge, fabrication of broadband antireflection structures using plasma etching without lithography or the assistance of any predeposited mask, as presented in this thesis, has not been reported. One of the main efforts has been to develop a low cost maskless, *i.e.* lithography-free and assistance-mask-free, fabrication method of broadband antireflection structures directly on the surface of glass, which can be cost-effectively applied in large areas and potentially in curved optical elements. Moreover, structures directly patterned on the glass surface have better thermal and mechanical performance than thin film coatings [38].

Schott B270 glass, also called superwhite, is a high grade glass material for optical components and its composition is very close to the composition employed in SOEs for CPV systems. For this reason, Schott B270 has been the model and the material most studied in this research. Fabrication of broadband antireflection nanostructures by maskless plasma etching was achieved on Schott B270 substrates.

The same process was applied to other type of glasses and quartz. In soda-lime substrates the transmittance was also improved, but less than in B270, in borosilicate substrates rough scattering surfaces were fabricated, on quartz substrates structures formation was not observed. A customized glass composition, Na<sub>2</sub>O-free B270 was studied showing as good performance as in commercial B270. Finally, very broadband antireflection effect was also obtained in CeO<sub>2</sub> doped cover glasses, which are the glasses employed to protect the solar cells in space.

### 3.2.1. Background of plasma etching

To texture the surface a mask is required. This mask can be pre-deposited or self-generated. Typically, the pre-deposited mask is done through a lithography process [29]. Other pre-deposited masks include metallic or organic layers that through dewetting or plasma etching become randomly distributed masks [35, 39]. The purpose of the mask is to protect the material below the mask from the physical and chemical interactions induced during the plasma etching process. In plasma etching, both physical and chemical interactions can be controlled, which allows very high selectivity.

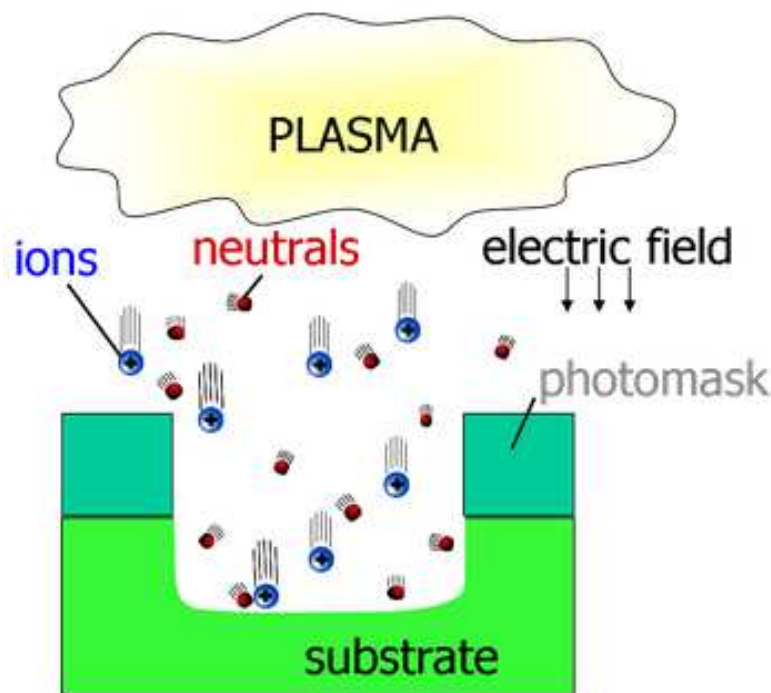


Fig. 3.9. Schema of the processes in plasma etching and the role of the mask.  
Figure is from Ref. [53].

The physical etching is carried out by high energy particles bombarding the surface of the sample. To protect the material below the mask, the mask has to be much stronger than the substrate against this particle bombardment. In this way, by the difference of the strength against the physical etching between the mask and the substrate, the substrate is physically etched creating the desired shape. The chemical etching is carried out by reactive chemical species that chemically attack the substrate and removes it from the surface. In this case, the role of the mask is to be inert against the chemical attack. The mask being inert to the chemical attack, protect the material below the mask and other areas of the substrate are chemically etched creating the desired shape. These interactions are summarized in Fig. 3.9.

$\text{CHF}_3$  in Reactive Ion Etching (RIE, Anelva DEA 507L) was employed to directly fabricate broadband antireflective structures on B270 surfaces without the assistance of any predeposited mask. The optimized etching parameters were 40 min, 800 W RF power, 75 sccm, and 2 Pa of pressure. The same process was applied to various types of glasses and quartz. After the  $\text{CHF}_3$  process, 10 min  $\text{O}_2$  plasma etching was applied for cleaning the residual fluorocarbon polymer from the surface of the samples.

### **3.2.2. Composition of B270 glass and other employed glasses**

In the present work, B270, D263 (Schott AG), and soda-lime (Asahi Glass Co.) glasses with typical dimensions of  $76 \times 26 \times 1.1 \text{ mm}^3$  were employed. As a high purity bulk  $\text{SiO}_2$  sample, quartz substrates with dimensions of  $18 \times 18 \times 0.5 \text{ mm}^3$ , were also treated. LIBA 2000 glass substrates provided by LPI, which is the same material as the SOE in the Ventana CPV system, were also evaluated. A customized glass composition,  $\text{Na}_2\text{O}$ -free B270, and  $\text{CeO}_2$  doped cover glasses provided by Qioptiq were also evaluated. The glass composition provided in the Material Safety Data Sheet (MSDS) of some of the glasses employed in this study is summarized in Table 1.

All substrates were cleaned in a 1% Contaminon solution (Wako Pure Chemical Industries, Ltd.) ultrasonic bath for 30 min, then rinsed in an ultrasonic bath with Milli-Q (Millipore Co.) deionized water for 30 min, and finally dried at  $80^\circ\text{C}$  for 10 hours. After the  $\text{CHF}_3$  and  $\text{O}_2$  plasma etching processes, a final cleaning process in an ultrasonic bath with deionized water for 5 min and drying was performed. In some cases, SPM process (Piranha solution) was also employed as cleaning processes after fabrication of the nanostructured surfaces.

<b>Table 1. MSDS composition data (%)</b>			
<b>Chemical formula</b>	<b>B270</b>	<b>D263</b>	<b>Soda-Lime</b>
<b>SiO<sub>2</sub></b>	>51	50-60	70-74
<b>Al<sub>2</sub>O<sub>3</sub></b>		1-10	0-3
<b>CaO</b>	<b>1-10</b>	<b>&lt;1</b>	<b>6-12</b>
<b>Na<sub>2</sub>O</b>	<b>1-10</b>	<b>1-10</b>	<b>12-16</b>
<b>K<sub>2</sub>O</b>	1-10	1-10	
<b>BaO</b>	1-10		
<b>ZnO</b>	1-10	1-10	
<b>MgO</b>		<b>1-10</b>	<b>0-6</b>
<b>Sulfur</b>		<1	
<b>B<sub>2</sub>O<sub>3</sub></b>		1-10	
<b>Sb<sub>2</sub>O<sub>3</sub></b>	<1		
<b>TiO<sub>2</sub></b>	<1	1-10	

Table 1. MSDS composition data of B270, D263, and soda-lime glasses.

### 3.2.3. Optical properties

#### Optical setup

In order to characterize the transmittance of the glass and PMMA substrates, Fresnel lenses, and aspheric lenses, an optical setup was built to achieve a collimated beam to scan the surface of the samples and collect the light into an integrating sphere as shown in Fig 3.10. In the case of Fresnel lenses optical characterization, the highly collimated beam was necessary to emulate the condition of sun tracking. The sun has a divergence of  $0.266^\circ$  and the divergence of the employed collimated beam was below  $0.2^\circ$ . The collimated beam was also particularly useful when evaluating the angle of incidence dependence on bare and nanostructured glass substrates.

The light intensity fluctuation in measurement time was below 0.2%. The transmittance of the glass substrates was measured from 400 nm to 1000 nm using a 1 cm diameter collimated beam at three different substrate positions to evaluate the homogeneity of the fabrication process.



For the transmittance measurements, the samples were placed 2 mm distant from the front port with the untreated side facing the integrating sphere. For the same spectral region, diffuse reflectance measurements were carried out placing the treated side of the substrates in contact with the back port and ensuring that the specular reflectance was outside the integrating sphere.

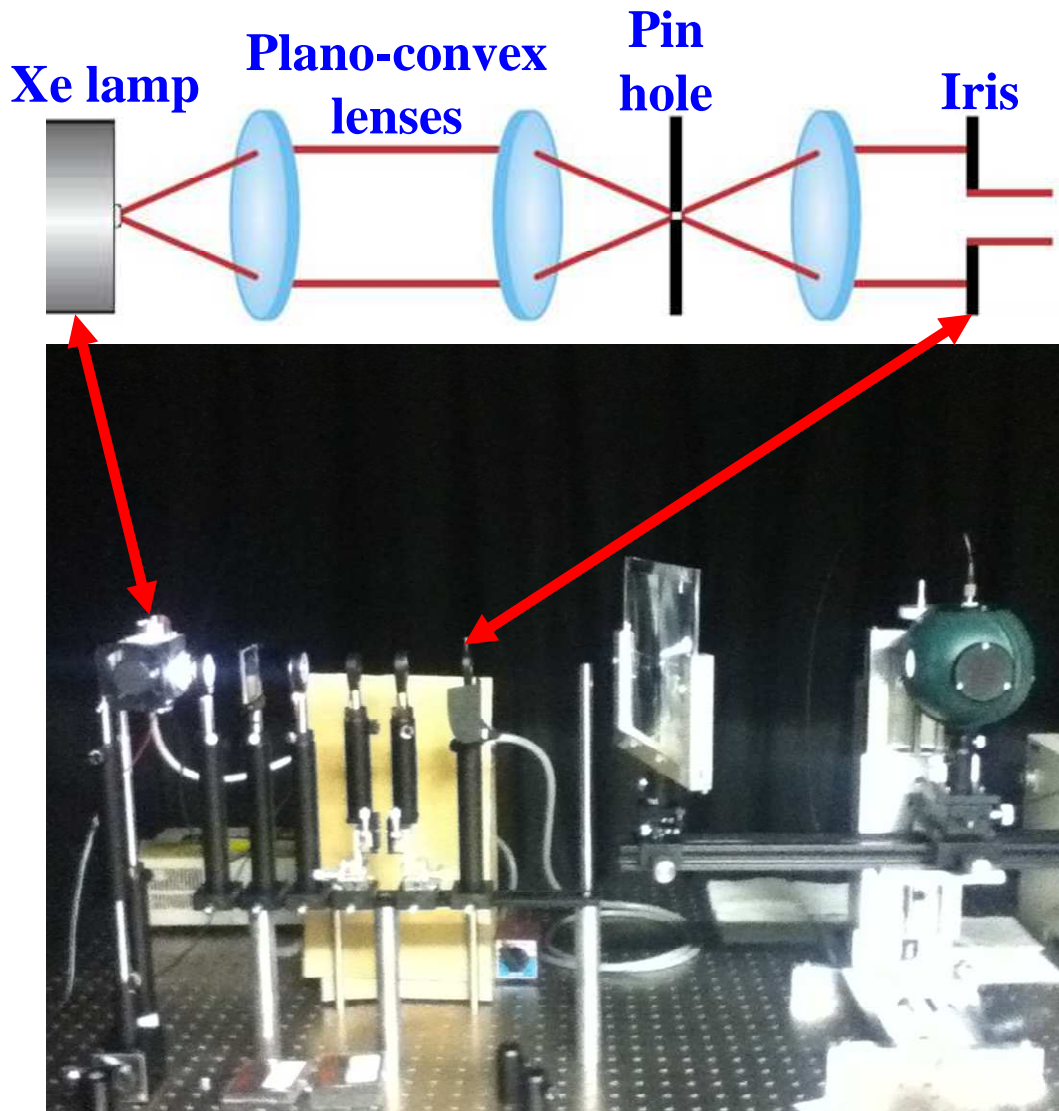


Fig. 3.10. Optical setup built to obtaining a collimated beam to evaluate the optical properties of nanostructured glass and PMMA substrates and lenses.



## Transmittance at normal incidence

The transmittance of bare B270 is around 92% in the measured spectra as shown in Fig. 3.11 (black). After optimizing the  $\text{CHF}_3$  plasma etching parameters, an increase in the transmittance was observed in one-side textured B270 substrates compared to the bare ones. However, the transmittance decreased with decreasing the wavelength in the whole measured spectra as shown in Fig. 3.11 (red). In addition, after  $\text{CHF}_3$  plasma etching, the substrates were slightly yellowish, which may correspond to fluorocarbon films that polymerize during plasma etching processes as has also been observed [54-57].

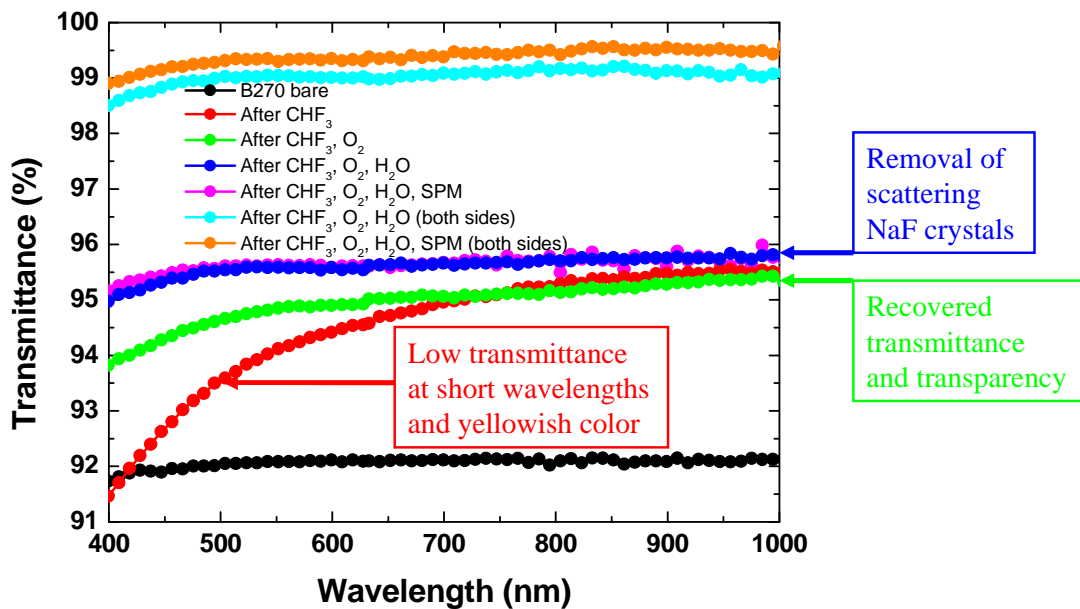


Fig. 3.11. Transmittance spectra after  $\text{CHF}_3$  (40 min) and  $\text{O}_2$  (10 min) plasma etching, deionized water rinsing, and SPM processes on one and both sides of B270 glass.

Subsequently,  $\text{O}_2$  plasma etching was performed as a cleaning process to remove the yellowish deposited material and the transparency was recovered as shown in Fig. 3.11 (green). Sodium fluoride (NaF) crystals of 500 nm to 1.5  $\mu\text{m}$  in size were observed by SEM-EDX on the surface of B270 after  $\text{CHF}_3$  plasma etching as shown in section 3.2.5. These crystals were removed, dissolving them by immersing the substrates in an ultrasonic bath with deionized water for 5 min.

The transmittance was further improved after removing them reaching almost 96% as shown in Fig. 3.11 (blue). A final SPM cleaning process was applied resulting in almost no effect or a very slight increase of the transmittance at short wavelengths as shown in Fig. 3.11 (magenta). These processes were applied on both sides of B270 substrates achieving over 99% transmittance in a broad range of the measured spectrum as shown in Fig. 3.11 (cyan). On the B270 substrates with both nanostructured sides, the SPM cleaning process had an additional broadband increase in the transmittance as shown in Fig. 3.11 (orange). The achieved antireflection performance on the double side treated sample was larger, especially at short wavelengths, than recent sophisticated lithography methods [29].

### Transmittance angle of incidence dependence

The transmittance angle of incidence dependence was evaluated on bare, one-side treated, and both-sides treated samples by placing them 2 cm in front of the integrating sphere and rotating them from  $0^\circ$  to  $60^\circ$  by steps of  $5^\circ$ . The transmittance angle of incidence dependences on bare, one-side treated, and both-sides treated are shown in Fig. 3.12, Fig. 3.13, and Fig. 3.14, respectively. For the purpose of visualizing the improvement the same scale of the vertical-axis is kept in the three figures.

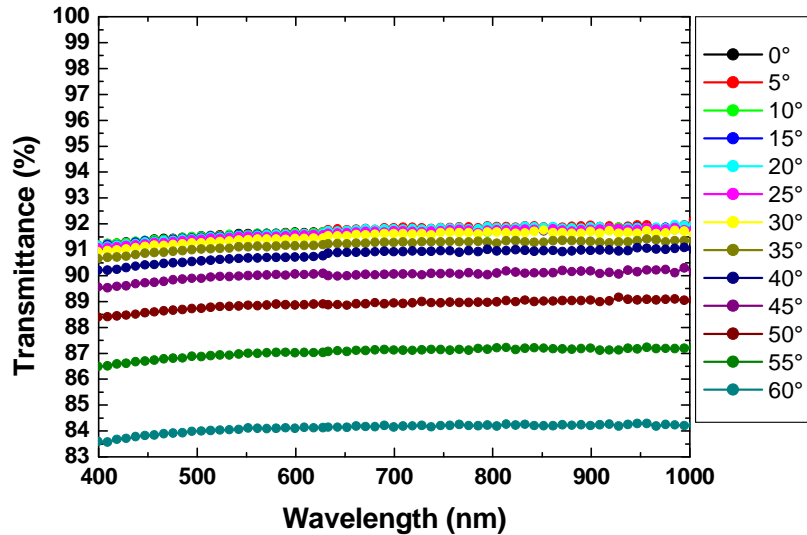


Fig. 3.12. Transmittance angle of incidence dependence spectra from  $0^\circ$  to  $60^\circ$  on bare B270 substrate.

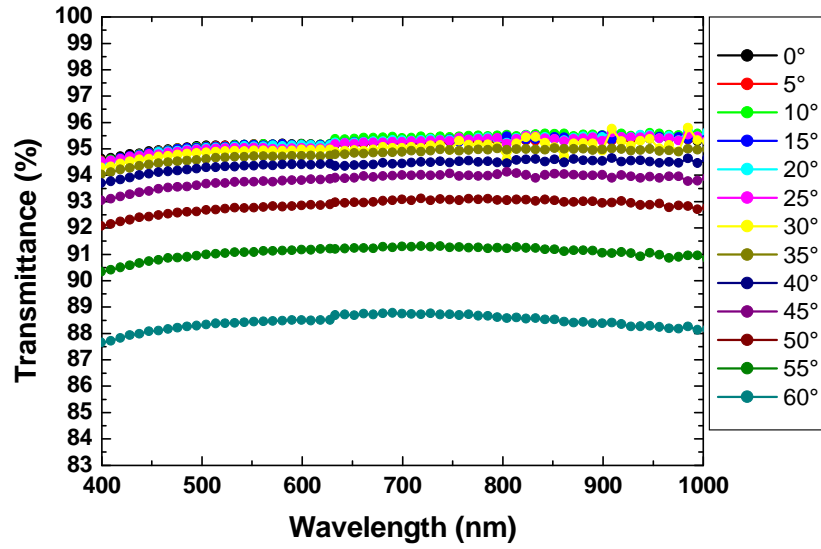


Fig. 3.13. Transmittance angle of incidence dependence spectra from 0° to 60° on B270 substrate after CHF<sub>3</sub> (40 min) and O<sub>2</sub> (10 min) plasma etching, and deionized water rinsing on one side.

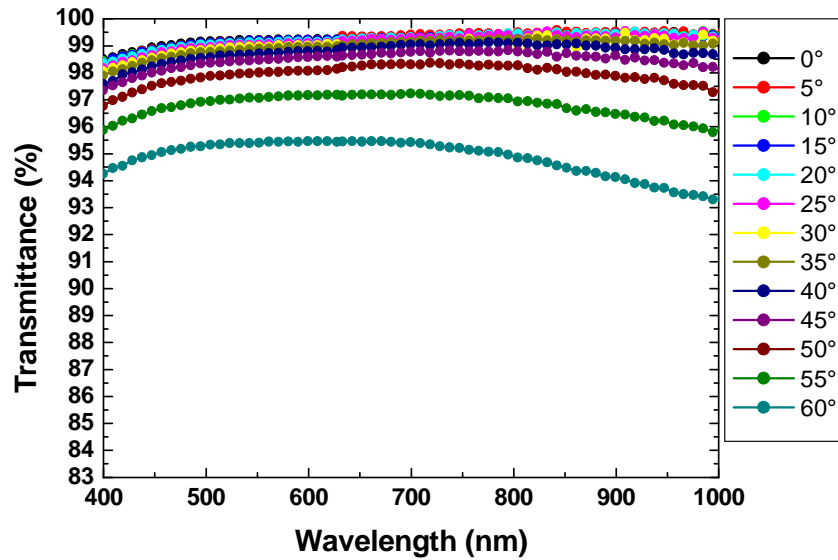


Fig. 3.14. Transmittance angle of incidence dependence spectra from 0° to 60° on B270 substrate after CHF<sub>3</sub> (40 min) and O<sub>2</sub> (10 min) plasma etching, and deionized water rinsing on both sides.

In summary, Fig. 3.12, Fig. 3.13, and Fig. 3.14 show that by texturing one side, the obtained broadband transmittance remains all over the measured angle of incidence range and that the reduction of the transmittance by increasing the incident angle is lower than the bare case as shown in Table 2. By texturing both sides the transmittance enhancement increases. In addition, by texturing both sides the reduction of the transmittance by increasing the incident angle is significantly reduced as shown in Table 2.

AOI	T. Bare	T. One side	T. Both sides
0°	91.68%	95.2%	99.23%
60°	84.1%	88.5%	95.46%
Diff. 0°-60°	7.58%	6.7%	3.77%

Table 2. Summarized transmittance difference at 0° and 60° at 600 nm on Bare B270 substrate, and after CHF<sub>3</sub> (40 min) and O<sub>2</sub> (10 min) plasma etching, and deionized water rinsing processes on one and both sides.

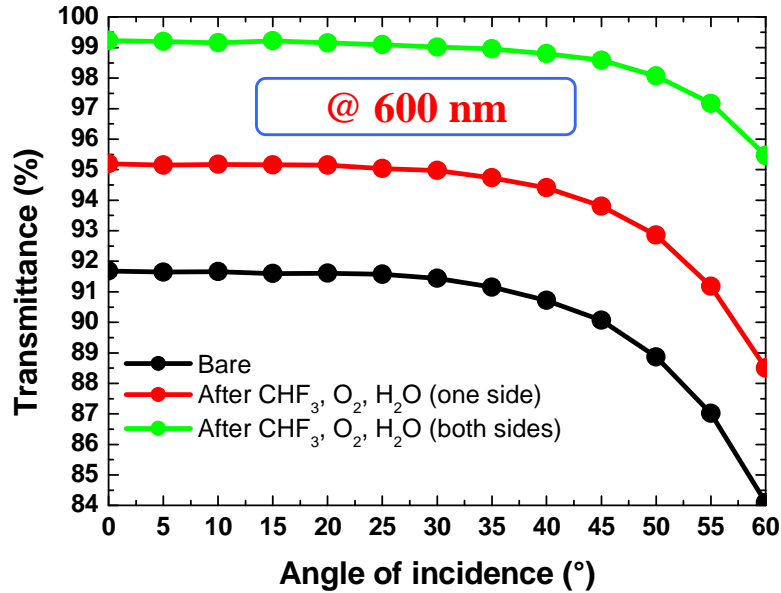


Fig. 3.15. Transmittance angle of incidence dependence spectra at 600 nm from 0° to 60° on bare B270 substrate, and after CHF<sub>3</sub> (40 min) and O<sub>2</sub> (10 min) plasma etching, and deionized water rinsing on one and both sides.

The transmittance angle of incidence dependence on bare, one-side treated, and both-sides treated from  $0^\circ$  to  $60^\circ$  for an incident wavelength of 600 nm is summarized in Fig 3.15 showing the transmittance increase and the lower angle of incident dependence by texturing one and both sides of B270 substrates.

### 3.2.4. Surface morphology by AFM

Surface morphologies were evaluated using Scanning Electron Microscope (SEM) and Atomic Force Microscope (AFM, Nanonavi Station/E-sweep, SII Nanotechnology). Figure 3.16 shows AFM images of the bare glass surface morphology and after 40 min  $\text{CHF}_3$  plasma etching, and after 10 min SPM process. Figure 3.16 revealed the subwavelength nature of the structures formed in B270 that originated the antireflection effect and that the SPM process did not induce any significant morphology modification within the AFM resolution. Fig. 3.16 does not resolve the whole height of the structures due to the short separation between individual “pillars”.

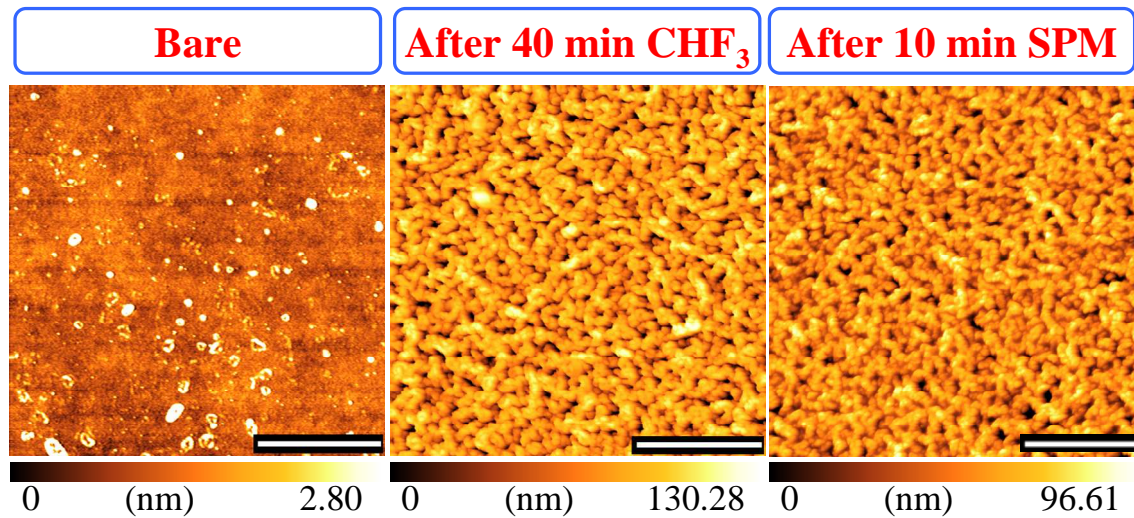


Fig. 3.16. AFM images of bare B270 substrate (left), after  $\text{CHF}_3$  (40 min) and  $\text{O}_2$  (10 min) plasma etching processes (right), and after subsequent 10 min SPM process. The white bar represents  $1\mu\text{m}$ .

After 10 min  $\text{O}_2$  plasma etching there was a broadband transmittance enhancement. The surface morphology after 1 and 10 min  $\text{O}_2$  plasma etching was evaluated, but it shows that within AFM resolution the  $\text{O}_2$  cleaning process did not have an effect on the morphology as shown in Fig.3.17.

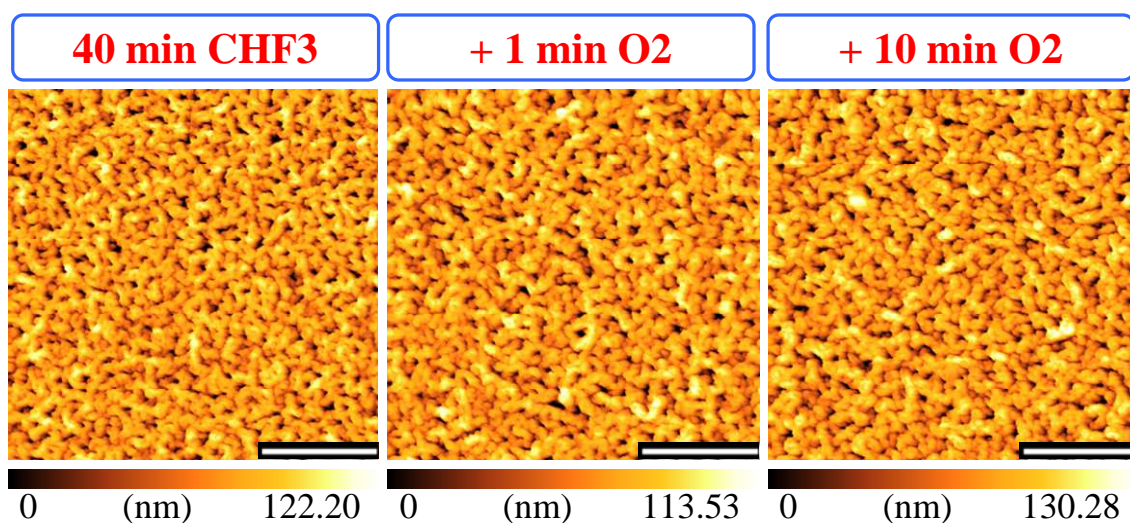


Fig. 3.17. AFM images of the nanostructured surface after 40 min  $\text{CHF}_3$  plasma etching (left) and after subsequent 1 min (middle) and 10 min (right)  $\text{O}_2$  plasma etching.

### 3.2.5. Surface morphology and composition by XPS and SEM-EDX

X-ray photoelectron spectroscopy (XPS) using  $\text{AlK-}\alpha$  X-rays was employed to characterize the composition of the surface of the glass substrates before and after both plasma etching processes on each type of glass and on quartz. Surface composition measurements were also carried out by means of SEM Energy Dispersive X-ray spectroscopy (SEM-EDX) using Hitachi FESEM S-4700.

On B270 glass, the XPS spectra was measured on the bare surface and after  $\text{CHF}_3$  plasma etching,  $\text{O}_2$  plasma etching, deionized water rinsing, and SPM process. On the bare surface, the Si  $2p$  (103.5 eV), Si  $2s$  (155 eV), and O  $1s$  (533 eV) peaks were clearly observed as shown in Fig. 3.18 (red). Also, small Ca  $2p$  (348 eV), Ca  $2s$  (440 eV), Auger Na KLL (493 eV, 532 eV, 561 eV) peaks and a small broad contamination related C  $1s$  (287 eV) peak were observed. This result on the bare surface is in agreement with the MSDS data summarized in Table 1.

After the  $\text{CHF}_3$  plasma etching process, the Si  $2p$ , Si  $2s$ , and O  $1s$  peaks vanished almost completely and it was very hard to observe any clearly defined peak as shown in Fig. 3.18 (green). After the  $\text{O}_2$  plasma etching process, Ca  $2p$ , Ca  $2s$ , Auger Na KLL, and F  $1s$  (688 eV), peaks became dominant, but the Si  $2p$ , Si  $2s$ , and O  $1s$  peaks remained very small as shown in Fig. 3.18 (blue). At this point a very important surface composition modification was observed.



The significance of this surface modification is that the oxides (CaO and Na<sub>2</sub>O) contained in B270, under CHF<sub>3</sub> plasma etching reacted forming fluoride compounds (Ca, F) and (Na, F) that remained on the surface. The decrease of the Si 2*p*, Si 2*s*, and O 1*s* peaks results from the selective removal of Si by CHF<sub>3</sub> plasma etching and the low boiling point of SiF<sub>4</sub> and OF<sub>2</sub>, which is below 0°C. These results show that the observed nanostructured surfaces by AFM have a different surface composition than the initial bare B270. Also, surface nanostructuration and transmittance enhancement occurred after the CHF<sub>3</sub> plasma etching process suggesting that the formation of the fluorides on the surface played a key role on the fabrication of the nanostructures.

After deionized water rinsing process, the Ca 2*p*, Ca 2*s*, Auger Na KLL, and F 1*s* (688 eV), peaks were still visible, but decreased. Also, the Si 2*p*, Si 2*s*, and O 1*s* peaks slightly increased as shown in Fig. 3.18 (magenta).

Finally, after SPM process, Ca 2*p*, Ca 2*s*, Auger Na KLL, and F 1*s* peaks further decreased and the Si 2*p*, Si 2*s*, and O 1*s* peaks were clearly visible again as shown in Fig. 3.18 (orange). After the SPM process a surface composition somehow similar to the composition on the bare substrate was reached.

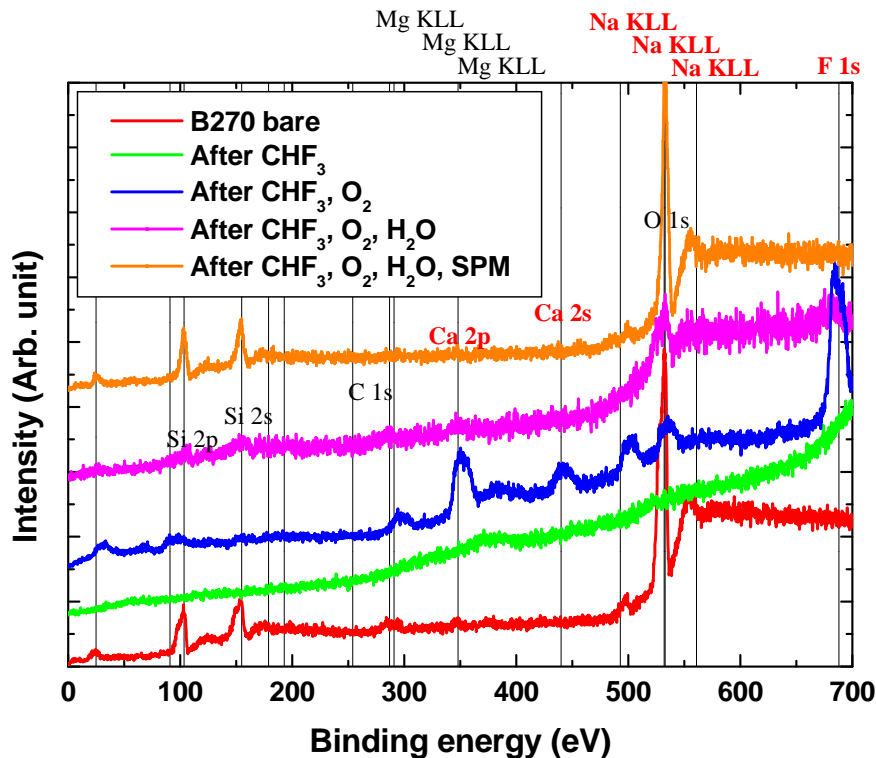


Fig. 3.18. XPS spectra carried out on bare B270 substrates and after the CHF<sub>3</sub> (40 min) and O<sub>2</sub> (10 min) plasma etching, deionized water rinsing, and SPM processes.

The transmittance measurements on one side treated B270 glass shown in Fig. 3.11 show that the transmittance enhancement observed after deionized water rinsing is accompanied by a surface composition modification. Fig. 3.19 supports that the dissolution of scattering NaF crystals on the surface originated this gain, which also explains the decrease of the Na KLL and F 1s peaks shown in Fig 3.18 (Magenta). Perhaps, (Ca, F) compound on the surface was also dissolved by water rinsing. The fact that the composition was returned to the bulk composition without affecting the morphology or reducing the transmittance enhancement, suggests that the key role that the fluorides play in the fabrication of the nanostructures is localized only on the top surface of the nanostructures. Otherwise, the nanostructures would have been dissolved and the transmittance deteriorated.

Cubic crystals with random distribution and different densities were observed on the surface of B270. The diameter of the XPS beam is approximately 500  $\mu\text{m}$ ; therefore, the NaF crystals observed in B270 are unavoidably included in the measurements. In B270, the textured surface and cubic crystals composition was evaluated using SEM-EDX showing a high Na and F content in the crystals compared to the textured surface as shown in Fig. 3.19. Additionally, the crystal structure of NaF is cubic form suggesting that they might be NaF crystals.

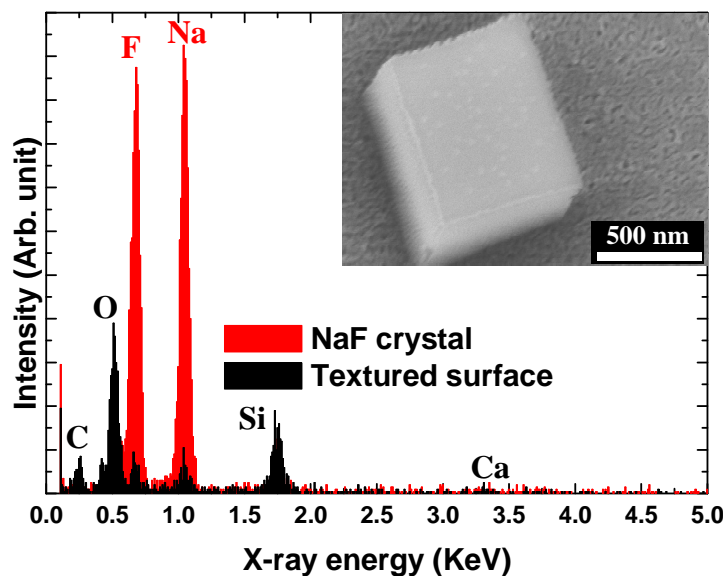


Fig. 3.19. SEM-EDX spectra on the textured surface (black) and focused on the NaF cubic crystal (red). The inset shows a SEM image of the textured surface and the NaF cubic crystal.



The size of the crystals was between 500 nm to 1.5  $\mu\text{m}$  and they act as scatterers on the surface. For this reason, the transmittance was further enhanced after removing them by dissolving them in water as shown in Fig. 3.11 (blue). NaF crystals distributed on the surface of B270 after 25 and 80 min  $\text{CHF}_3$  plasma etching process are shown in Fig. 3.20. Randomly distributed crystals on the surface are shown after both 25 and 80 min meaning that the NaF crystals are already formed within 25 min of  $\text{CHF}_3$  plasma etching and that they remain on the surface after 80 min.

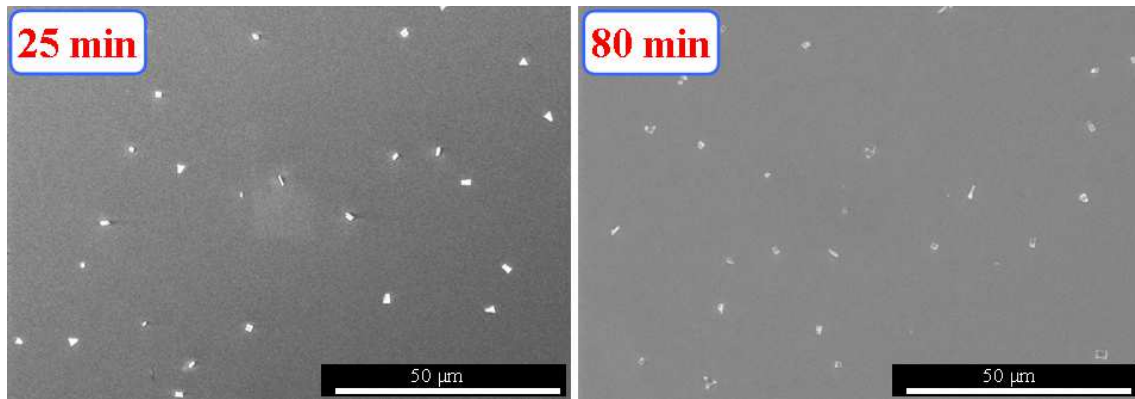


Fig. 3.20. SEM image of B270 glass after 25 (left) and 80 (right) min  $\text{CHF}_3$  plasma etching showing the presence and permanence of NaF crystals on the surface.

The effect of the  $\text{O}_2$  plasma etching process on the NaF crystals was also analyzed by looking at oblique view of the cross section as shown in Fig. 3.21. Since the NaF crystals were not removed, it seems that the  $\text{O}_2$  plasma etching process does not have any effect on the NaF crystals and there is only modification after deionized water rinsing.

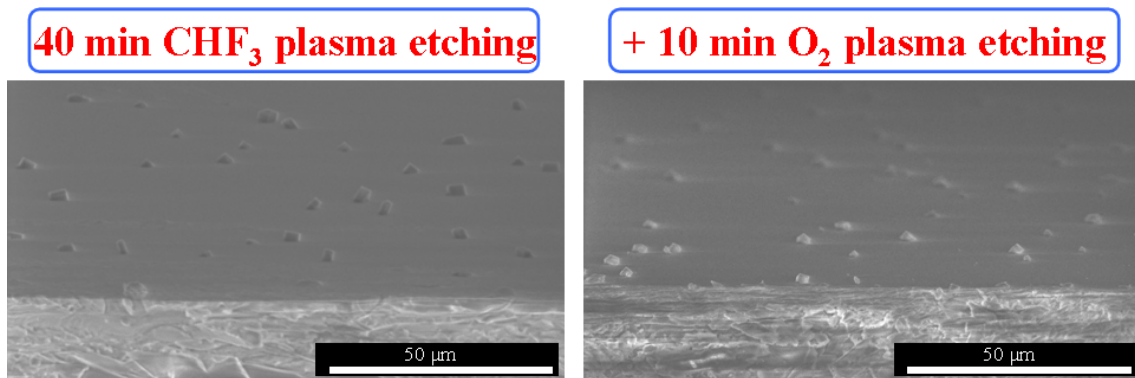


Fig. 3.21. SEM cross-section images of B270 after 40 min  $\text{CHF}_3$  (left) and subsequent 10 min  $\text{O}_2$  (right) plasma etching.

### 3.2.6. Cross section morphology and composition by STEM-EDX

In order to further analyze the cross section of the antireflection nanostructures fabricated on B270 and their composition, Scanning Transmission Electron Microscope (STEM) (STEM-EDX) measurements were performed using Hitachi High-Technologies HD-2700 and EDAX Genesis.

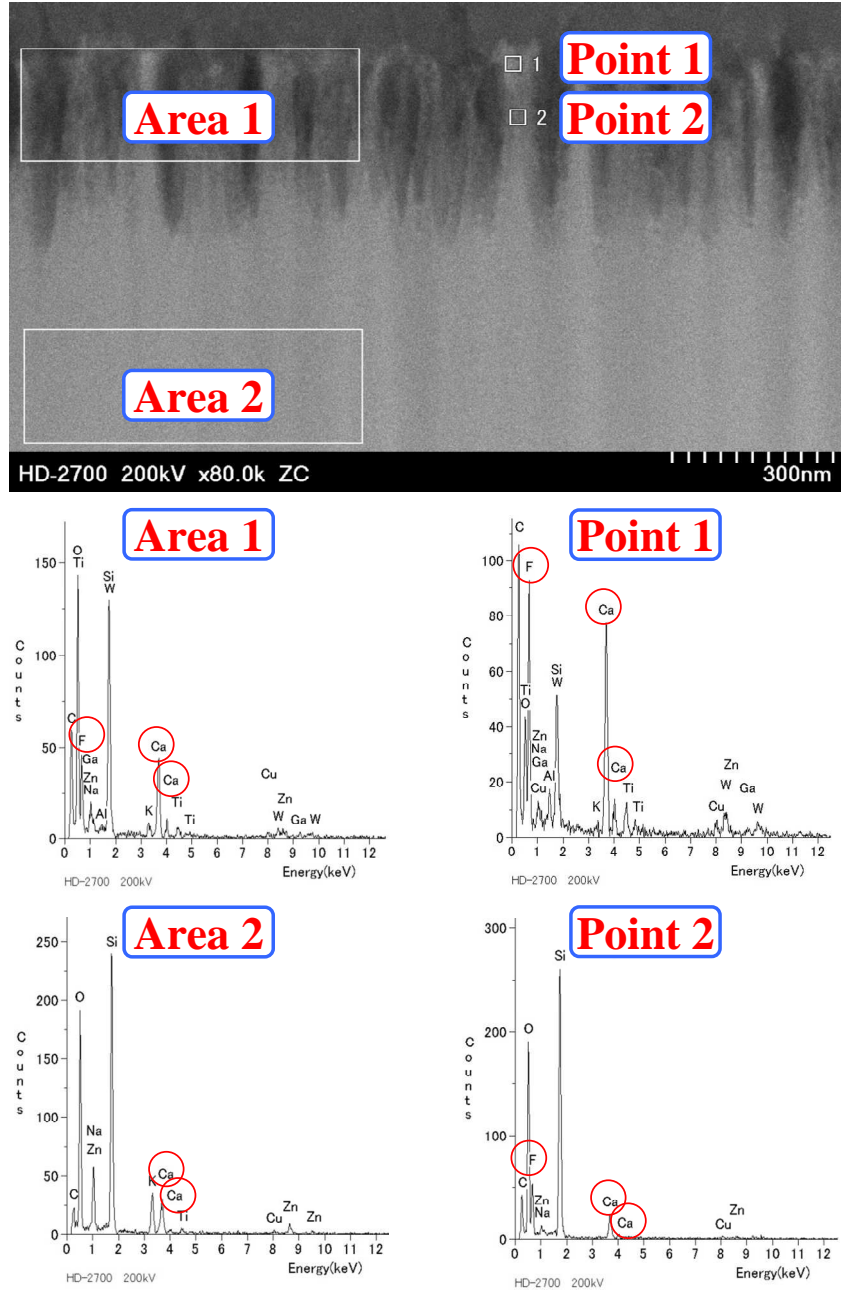


Fig. 3.22. STEM cross-section image of B270 after 40 min  $\text{CHF}_3$  plasma etching (top) and STEM-EDX spectra on two areas and points of the cross-section (bottom).

The first cross section morphology and composition analysis by STEM-EDX is shown in Fig. 3.22. Regarding the morphology, Fig. 3.22 shows that dense pillars with around 100 nm in size and over 300 nm in height were fabricated on the surface of B270 glass after 40 min  $\text{CHF}_3$  plasma etching.

The high aspect ratio and the small size of the nanostructures explain the broadband antireflection effect shown in Fig. 3.11. The AFM images shown in Fig. 3.16 could not resolve the whole aspect ratio of the nanostructures because of their high density and the small gap of tens of nanometers between them. In Fig. 3.2, the STEM-EDX spectra show the composition of the cross section at two large areas (Area 1 and Area 2 corresponding to the top part of the nanostructured surface and the bulk B270 glass, respectively) and it is also measured at two points (Point 1 and Point 2 corresponding to the tip of one nanostructure and at a lower position than Point 1 towards half-height, respectively).

The cross section composition observed in Area 2 is in agreement with the expected results compared to the MSDS data shown in Table 1. In Area 1, an F peak appears and the Ca peaks also increase in intensity compared to the maximum intensity of Si and O. The observed STEM-EDX results are in agreement with the XPS measurements shown in Fig. 3.18 in which F and Ca appeared to be accumulated at the surface. More detailed inspection of the pillar composition was carried out by evaluating the composition at the tip (Point 1) and towards half-height of one pillar (Point 2) as shown in Fig. 3.22. The STEM-EDX spectra at point 1 shows that F and Ca peaks have larger intensity than Si and O owing to their concentration as observed by XPS. The concentration of F and Ca is lowered away from the tip as shown by the STEM-EDX spectra at Point 2.

These results suggest that the (Ca, F) accumulation occurs only at the tip of the nanostructures. This is also in agreement with the conclusion that the key role that the fluorides play in the fabrication of the nanostructures is localized only on the top surface of the nanostructures in section 3.2.5.

In order to understand in detail the cross section composition of the pillars STEM-EDX mapping was carried out on the nanostructures and composition obtained on B270 glass just after 40 min  $\text{CHF}_3$  plasma etching as shown in Fig. 3.23. The cross section compositions of O, F, Ca, Si and Na by STEM-EDX mapping are shown in Fig. 3.23. Figure 3.23 shows that there is a higher Ca and F concentration at the tips of the nanostructures compared to the bulk, Si and O density is low at the tips and gradually increase from the tips of the nanostructures towards the bulk, and there is not any particular concentration of Na in the pillars.

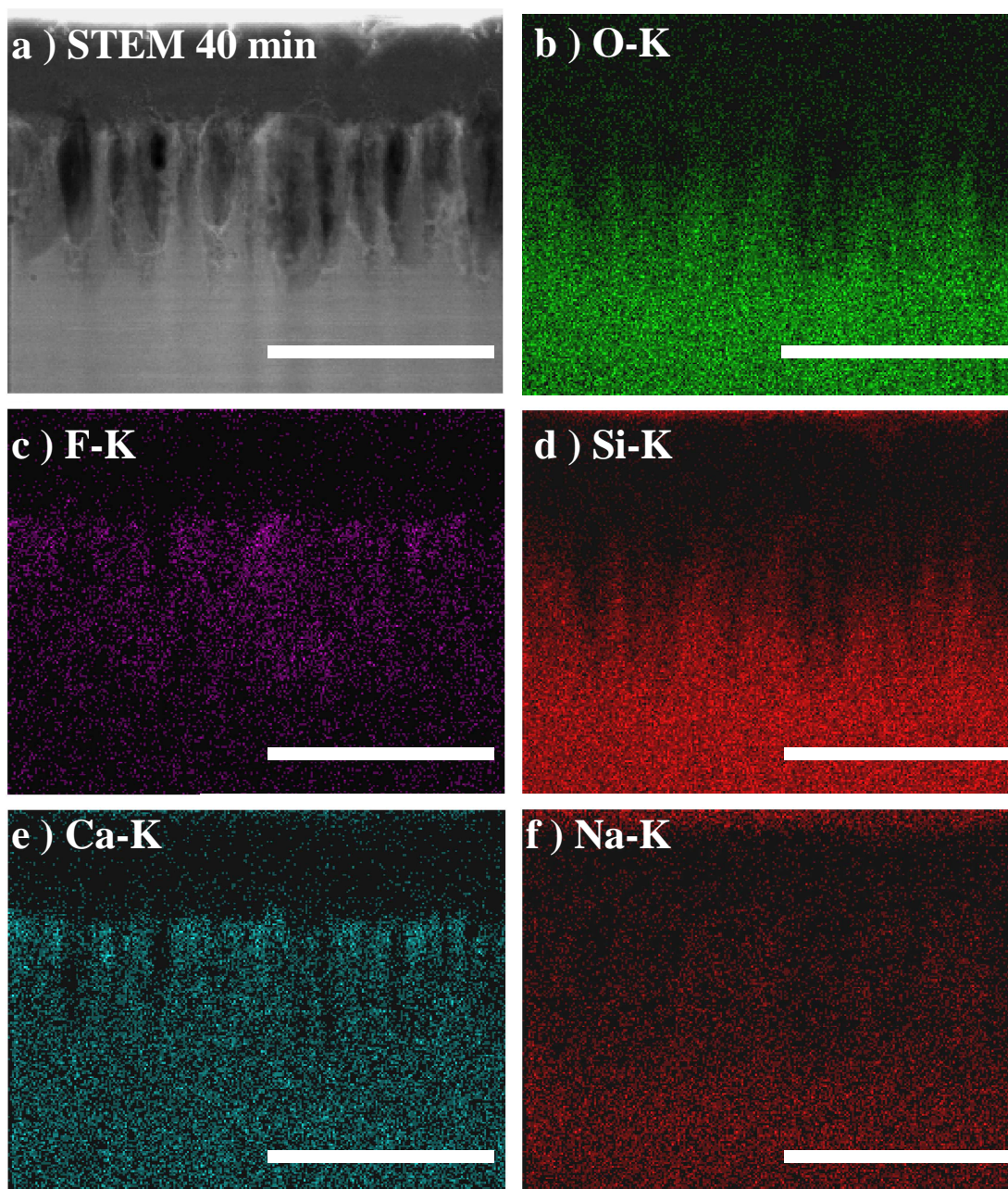


Fig. 3.23. STEM cross section image of B270 after 40 min  $\text{CHF}_3$  plasma etching a). Elements distribution images of O b), F c), Si d), Ca e), and Na f) obtained by STEM-EDX on the a). The white bar represents 500 nm.

The observed elements distribution supports the formation of a CaF self-generated mask at the tips of the nanostructures in agreement with the XPS results shown in Fig. 3.18. CaO contained in B270, under  $\text{CHF}_3$  plasma etching reacted forming (Ca, F) compound that self-generated into a mask at the tips of the nanostructures.



This (Ca, F) self-generated mask has the two characteristics of a mask that can sustain both physical and chemical plasma etching described in section 3.2.1. As for physical plasma etching,  $\text{CaF}_2$  is a very strong material with boiling point of  $2553^\circ\text{C}$ . As for chemical plasma etching, (Ca, F) self-generated mask, being a fluoride, reacts little or almost nothing with the  $\text{CHF}_3$  plasma etching. The accumulation of (Ca, F) at the tips of the nanostructures and its resistance against physical and chemical plasma etching resulted in the protection of the glass below the (Ca, F) self-generated mask and therefore formation of high aspect ratio nanostructures under sustained  $\text{CHF}_3$  plasma etching. More analysis of the self-generated masks is introduced in section 3.4. Figure 3.23 shows that there is not any particular concentration of Na in the pillars, which supports that the Na KLL peaks in the XPS spectra correspond only to the NaF crystals on the surface as shown in Fig. 3.19. Figure 3.18 showed a decrease of the Si  $2p$ , Si  $2s$ , and O  $1s$  peaks in the XPS spectra and Fig. 3.23 shows that more than just a decrease of Si and O on the surface, their density is actually gradient from low density at the tips of the nanostructures and increasing towards the bulk reaching the same density as the bulk at the bottom of the nanostructures. Si and O are selectively removed by  $\text{CHF}_3$  plasma etching and they do not accumulate on the nanostructures, they evaporate owing to the low boiling point of  $\text{SiF}_4$  and  $\text{OF}_2$ , which is below  $0^\circ\text{C}$ . In addition, as the plasma etching process time is sustained; further Si and O selective removal occurs towards the top of the nanostructures because they are more accessible to the  $\text{CHF}_3$  plasma, creating a graded density. After SPM process the Si  $2p$ , Si  $2s$ , and O  $1s$  peaks in the XPS spectra were clearly visible again suggesting that after SPM process the (Ca, F) self-generated mask is removed and the tips of the nanostructures are exposed. Since after SPM process the morphology and the transmittance enhancement were not modified, the exposed tips and nanostructures would still have the graded  $\text{SiO}_2$  density. It has been reported that “Moth-eye” like nanostructures generate a graded refractive index transition that in particular achieves significant antireflection effect when the height of the nanostructures is 40% or higher compared to the wavelength [30, 31]. The lateral size of the structures is also critical and needs to be of subwavelength nature to avoid scattering. For example, to effectively suppress the reflection in the ultraviolet and visible region it has to be smaller than 200 nm [36, 58]. The outstanding broadband transmittance improvement shown in Fig 3.11 by the fabricated nanostructures shown in Fig. 3.22 can be better understood by the combination of a geometrical “Moth-eye” effect and a graded material density of  $\text{SiO}_2$  in the nanostructures. Furthermore the observed random nature of the fabricated structures cause no diffraction patterns compared to the periodic ones [32].

### 3.2.7. Aspect ratio tunability and fabrication process

#### Etching ratio in B270 and quartz

In order to evaluate the etching ratio on B270 and quartz, a 300-nm-thick aluminum pattern was deposited on the glass surface through a stencil mask. Then,  $\text{CHF}_3$  plasma etching was applied at different duration times between 1 to 80 min. Typically, RF power equal to 800 W was employed. The RF power dependence is introduced at the end of this section. Finally, the aluminum mask was removed using tetramethyl ammonium hydroxide (Tokyo Ohka Kogyo Co.) and the profile of the hills and valleys was measured using Dektak XT (Bruker). The depth of the valleys represents the etching depth shown in Fig. 3.24.

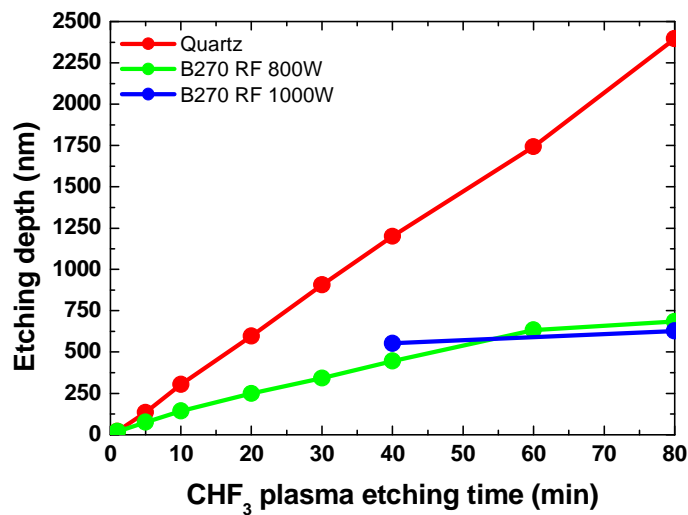


Fig. 3.24. Etching depth on B270 and quartz after 1 to 80 min  $\text{CHF}_3$  plasma etching using a protective 300-nm-thick Aluminum mask and measured by DekTak after removing it.

Under RF equal to 800 W, Fig. 3.24 shows that the etching ratio on quartz is approximately 30 nm per min, while it is approximately 11 nm per min, on B270 glass, on which it tends to saturate after 80 min. Figure 3.22 shows that nanostructures with a height over 300 nm were fabricated after 40 min  $\text{CHF}_3$  plasma etching. Figure 3.24 shows that for the same plasma etching time, a thickness of 445 nm was removed from the surface of bare B270 glass. Figure 3.23 showed that there is a self-generated (Ca, F) mask that remained at the tip of the nanostructures and allowed their formation.

This (Ca, F) self-generated mask was formed from the CaO contained in B270 and the reaction with  $\text{CHF}_3$  plasma etching. The amount of Ca required for self-generating the mask that allowed the formation of the nanostructures shown in Fig. 3.22 came from the 445 nm that were removed from the B270 surface. This observation indicates that there is a certain amount of CaO reacting with  $\text{CHF}_3$  plasma etching needed for self-generating the (Ca, F) mask and begin fabrication of the nanostructures. The loss of the almost linear tendency and tendency to saturate after 80 min of sustained  $\text{CHF}_3$  plasma etching may be originated by the formation of a thicker (Ca, F) etch-stop layer.

### Optical properties

The transmittance of the B270 substrates treated with  $\text{CHF}_3$  plasma etching applied at different duration times between 1 to 80 min was measured just after  $\text{CHF}_3$  plasma etching, after subsequent  $\text{O}_2$  plasma etching, and after subsequent deionized water rinsing as shown in Fig 3.25, Fig 3.26, and Fig. 3.27, respectively. Figure 3.25 shows that only after 20 min of  $\text{CHF}_3$  plasma etching transmittance enhancement was obtained. Even after  $\text{O}_2$  plasma etching and deionized water rinsing, there is no significant transmittance enhancement for the applied plasma etching times below 20 min. Figure 3.24 shows that between a to 20 min the etching depth increases linearly with  $\text{CHF}_3$  plasma etching time, which indicates that between 10 to 20 min enough (Ca, F) self-generated mask was reached and surface nanostructuration began.

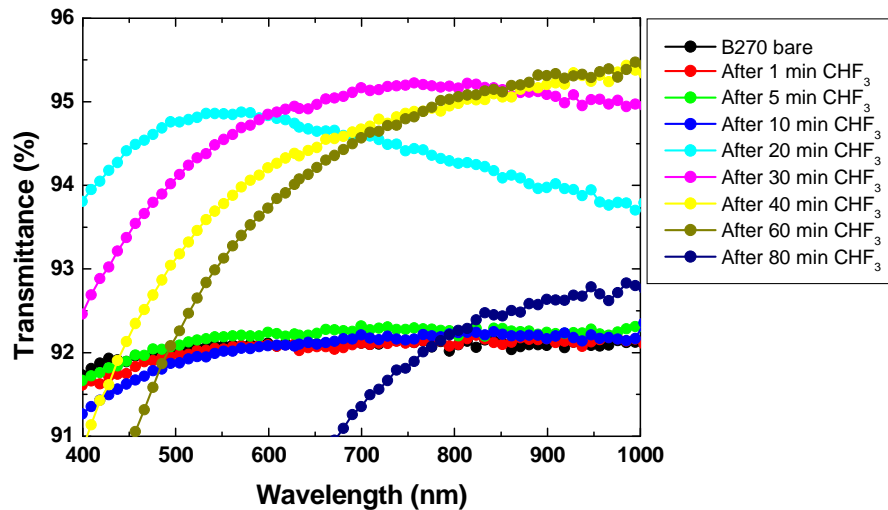


Fig. 3.25. Transmittance spectra dependence on the  $\text{CHF}_3$  plasma etching time from 1 to 80 min.

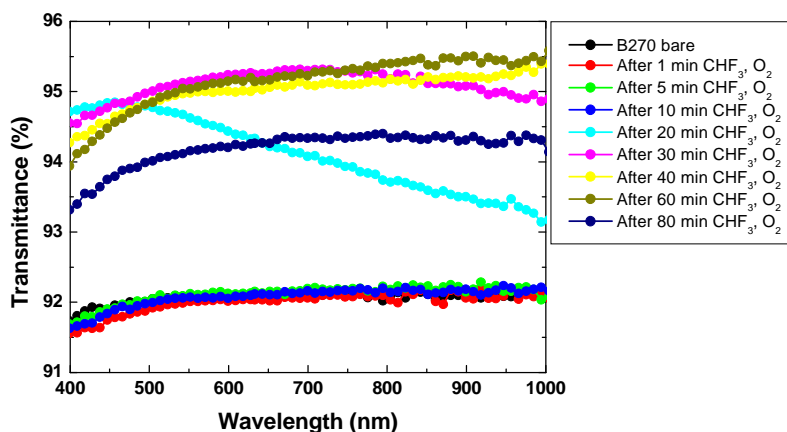


Fig. 3.36. Transmittance spectra dependence on the  $\text{CHF}_3$  plasma etching time from 1 to 80 min. Subsequent 10 min  $\text{O}_2$  plasma etching was applied on all samples.

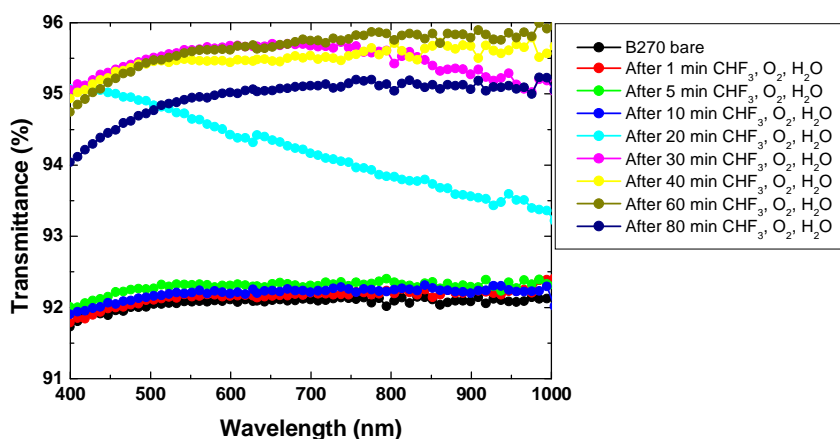


Fig. 3.27. Transmittance spectra dependence on the  $\text{CHF}_3$  plasma etching time from 1 to 80 min. Subsequent 10 min  $\text{O}_2$  plasma etching and deionized water rinsing were applied on all samples.

Just after  $\text{CHF}_3$  plasma etching there was low transmittance enhancement at short wavelengths accompanied by slight yellowish coloration of the samples. The intensity of this coloration increased with increasing time meaning that with longer time, more fluorocarbon polymer is deposited. After subsequent  $\text{O}_2$  plasma etching, the transmittance at short wavelengths was recovered and after subsequent deionized water rinsing the transmittance further increased owing to the removal of NaF crystals.



### Cross sections by SEM

In order to evaluate the morphology dependence of the structures on  $\text{CHF}_3$  plasma etching time, SEM images of the cross sections on samples treated from 20 to 80 min were obtained as shown in Fig. 3.28.

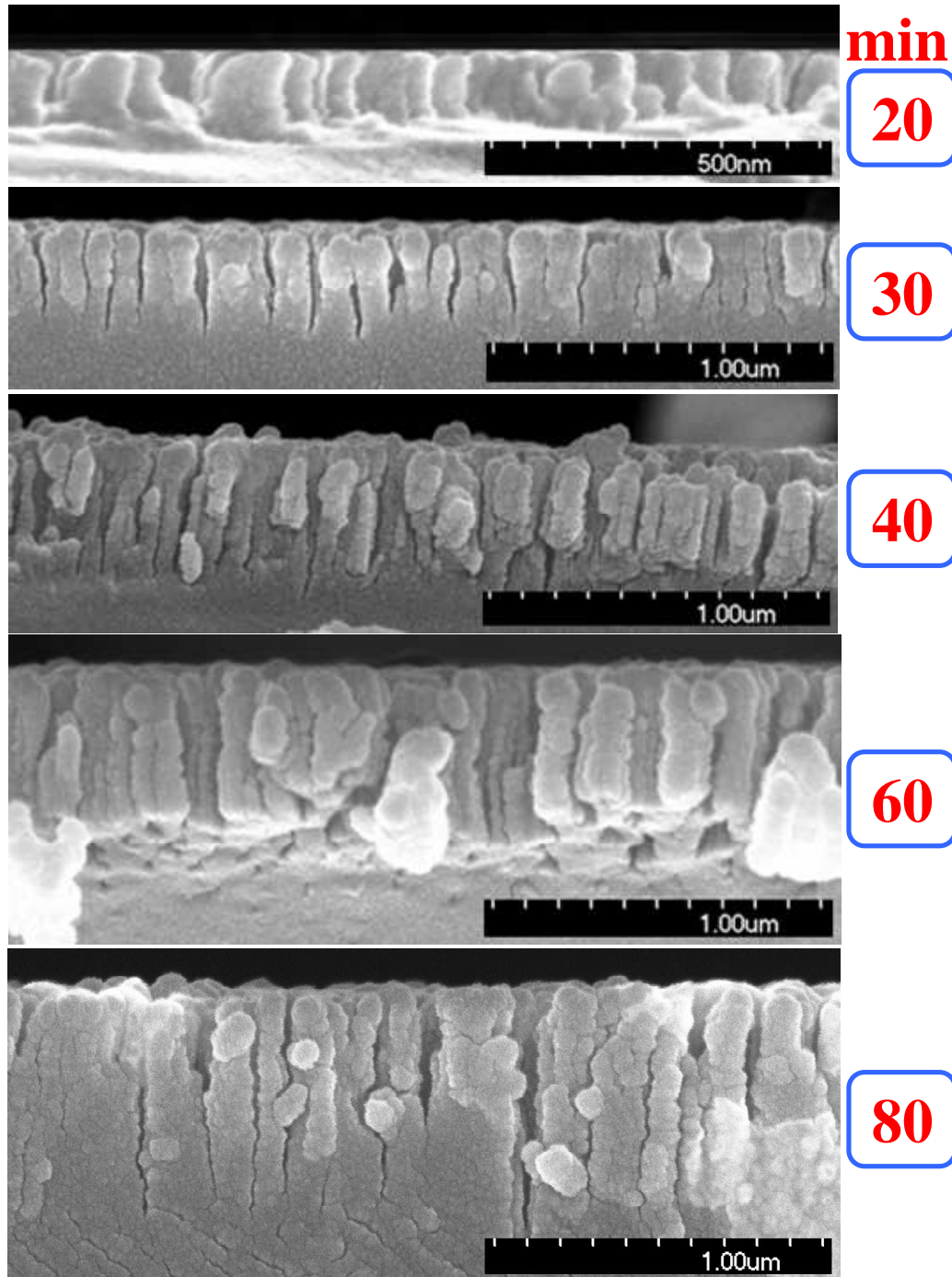


Fig. 3.28. SEM images of the nano-pillars aspect ratio dependence on the  $\text{CHF}_3$  plasma etching time from 20 to 80 min.

Nanostructured surface after  $\text{CHF}_3$  plasma etching was observed from an etching time of 20 min. Samples treated from 1 to 10 min did not show nanostructured surface. This result is in agreement with the transmittance enhancement shown in Fig 3.27 where only after 20 min transmittance enhancement was observed. This result also supports that between 10 to 20 min enough (Ca, F) self-generated mask was reached and surface nanostructuration began. As shown in Fig. 3.27, the optical properties of the nanostructured surface can be tuned by controlling the plasma etching time, which controls the aspect ratio of the nanostructures. The size of the nanostructures appeared approximately constant around 100 nm, while the aspect ratio increased with increasing  $\text{CHF}_3$  plasma etching time as shown in Fig. 3.29.

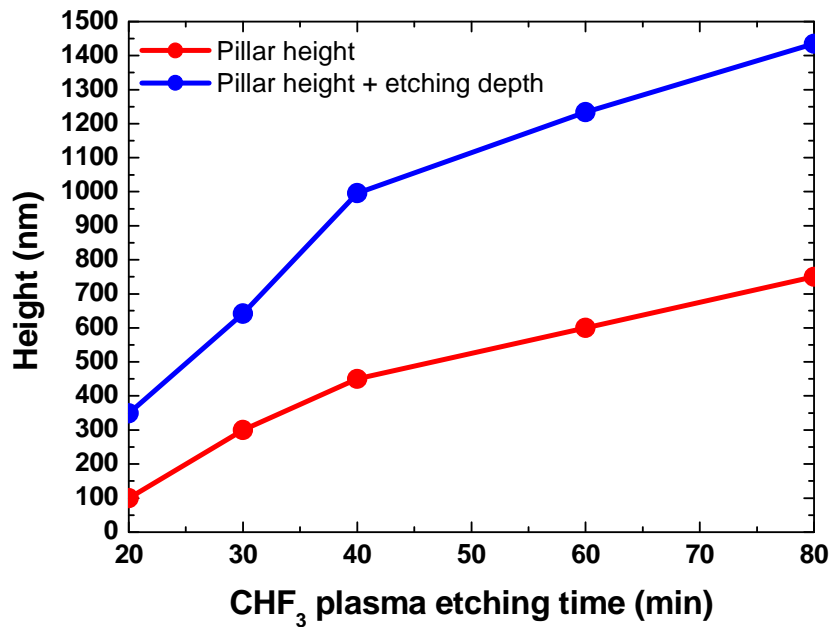


Fig. 3.29. Approximated pillar height measured on the SEM images of B270 substrates after  $\text{CHF}_3$  plasma etching from 20 to 80 min.

Figure 3.29 shows that at the beginning the aspect ratio of the nanostructures rapidly increases with time, but that the speed of the pillar height increase with time decreases as the  $\text{CHF}_3$  plasma etching time increases because as the nanostructures aspect ratio becomes larger and due to their high density and small inter-distance, it becomes harder for the ions to selectively remove Si and O at the bottom of the nanostructures. This is also evidenced by the narrowing of the gap between the bottom of the pillars.

## Fabrication process

Based on the XPS, STEM-EDX, Dektak, and SEM results, a model describing the fabrication process of random high density nanostructures with controllable aspect ratio using maskless  $\text{CHF}_3$  plasma etching on bare B270 glass is proposed in Fig. 3.30.

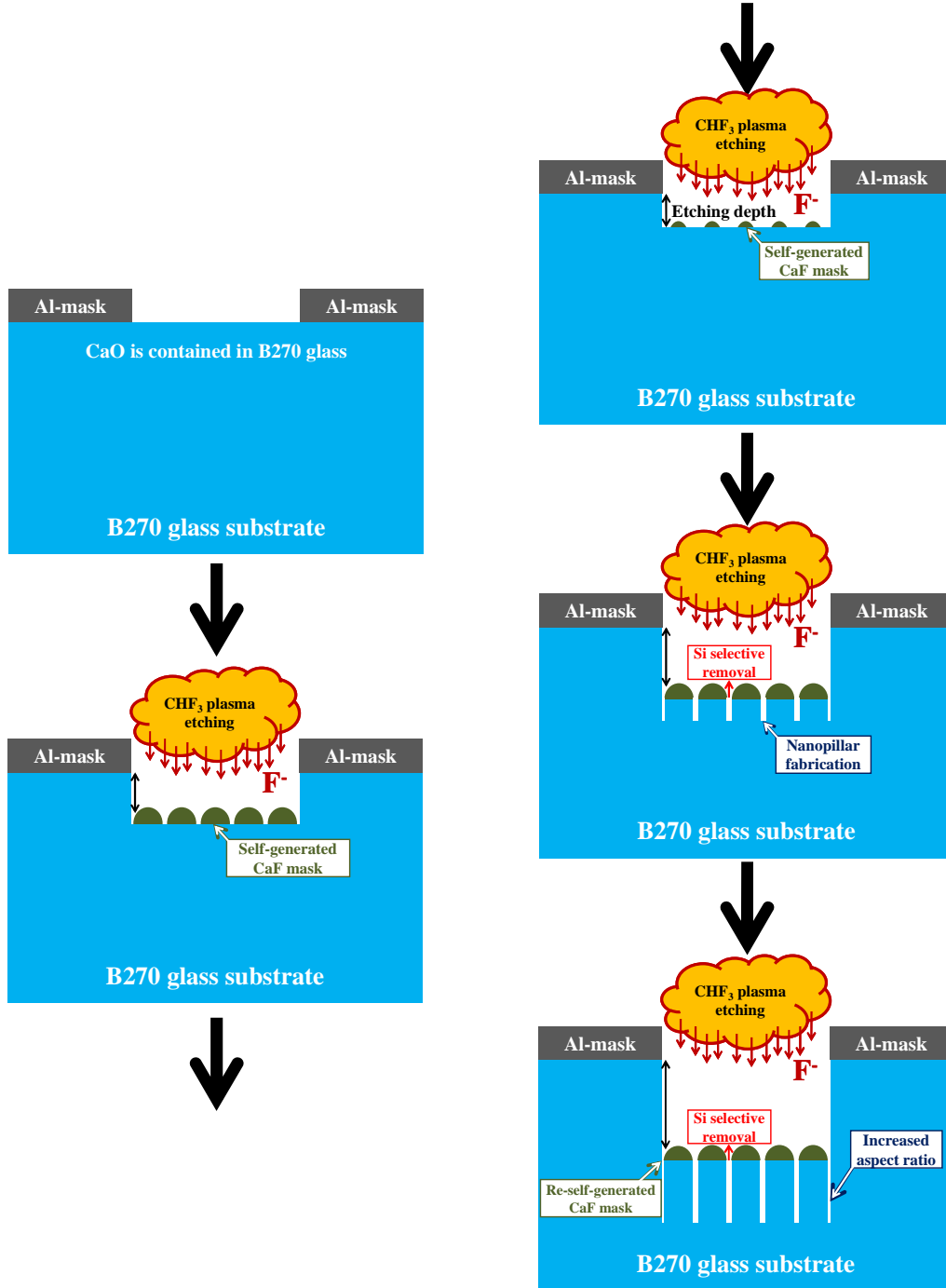


Fig. 3.30. Model of the surface nanostructuring process using  $\text{CHF}_3$  plasma etching on B270 glass, based on the XPS, STEM-EDX, Dektak, and SEM results.

The model proposed in Fig. 3.30 shows that from the beginning of the  $\text{CHF}_3$  plasma etching process, the whole surface of the B270 glass decreases creating the etching depth shown in Fig. 3.24. As the etching depth increases, from the available CaO in B270 glass, the (Ca, F) self-generated mask is formed and once it reaches a certain size or thickness, fabrication of the nanostructures can begin. The threshold from which enough (Ca, F) self-assembled mask formation and nanostructures formation began is between 10 to 20 min as supported the transmittance enhancement and SEM images shown in Fig. 3.27 and Fig. 3.28, respectively. Finally, with increasing  $\text{CHF}_3$  plasma etching time, the aspect ratio of the nanostructures increases as summarized in Fig. 3.29. One additional observation is that as the nanostructures aspect ratio increased with  $\text{CHF}_3$  plasma etching time, the etching depth also increased; meaning that the whole front of (Ca, F) self-generated mask is going downwards with increasing  $\text{CHF}_3$  plasma etching time. The (Ca, F) accumulation only at the tips of the nanostructures and the increasing etching depth with time suggests that the (Ca, F) self-generated mask at the tips of the nanostructures observed after 20 min  $\text{CHF}_3$  plasma etching is not the same as the one on the tips of the nanostructures observed after 80 min, which indicates that there is decomposition and re-self-generation of the (Ca, F) at the tips of the nanostructures under sustained  $\text{CHF}_3$  plasma etching. More analysis of the self-generated masks is introduced in section 3.4.

### Pillar and Tapered nanostructures shapes

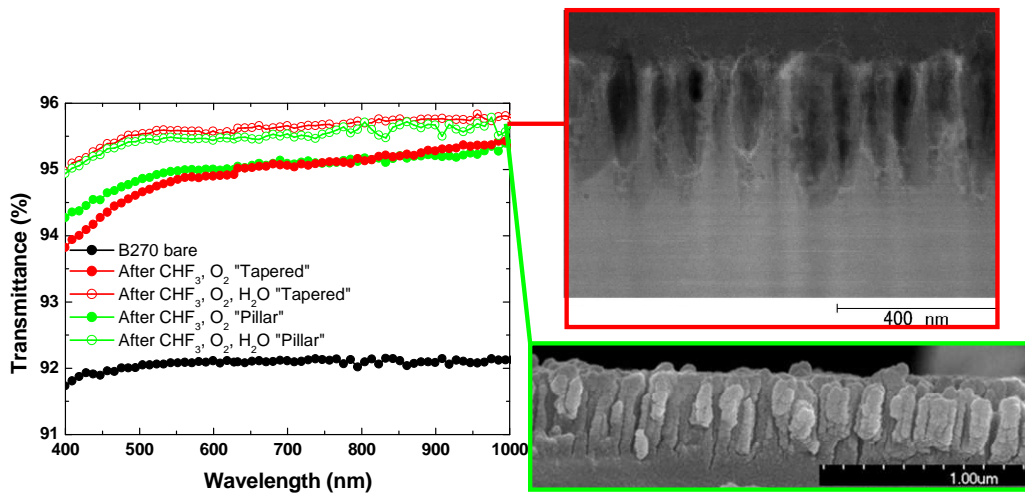


Fig. 3.31. Transmittance spectra and cross-section images of “Tapered” and “Pillar” nanostructures obtained after  $\text{CHF}_3$  (40 min) plasma etching. Subsequent 10 min  $\text{O}_2$  plasma etching and deionized water rinsing were applied on both samples.

The SEM cross section images of B270 glass substrates after  $\text{CHF}_3$  plasma etching show that pillar as well as tapered morphologies can be obtained as shown in Fig 3.31 and Fig. 3.32 for 40 and 80 min plasma etching time, respectively. The tapered shapes have sharper tips and the width of the nanostructures increases towards the bottom. The tapered geometry is in accordance with the “Moth-eye” principle to obtain antireflection effect in which a graded effective refractive index is obtained by the tapered shape [30, 31].

Pillar shapes are expected to have lower transmittance enhancement than tapered shapes because the pillar geometry creates a less gradient effective refractive index compared to the tapered shape. Unintuitively, the performance of the pillar nanostructures is about the same or even slightly better at short wavelengths than the tapered shape obtained after 40 min  $\text{CHF}_3$  plasma etching. Figure 3.23 showed that the nanostructures have graded  $\text{SiO}_2$  density from low density at the tips and increasing towards the bottom of the nanostructures, which enhances the antireflection effect of the nanostructured surface. The graded  $\text{SiO}_2$  density and the transmittance enhancement shown in Fig. 3.31 suggest that independently of the shape, the graded  $\text{SiO}_2$  density plays the main role that achieves broadband transmittance enhancement. In some cases, the tapered shape outperforms the pillar shape as shown in Fig. 3.32, but both characteristics the shape and the composition of the nanostructures should be evaluated to consider the influence of each to the transmittance enhancement.

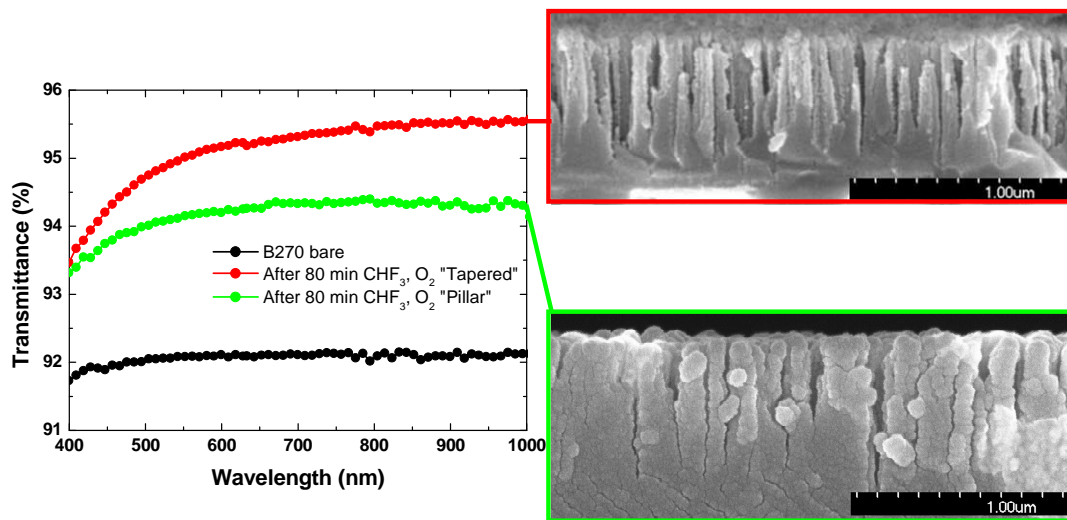


Fig. 3.32. Transmittance spectra and cross-section images of “Tapered” and “Pillar” nanostructures obtained after  $\text{CHF}_3$  (80 min) plasma etching. Subsequent 10 min  $\text{O}_2$  plasma etching was applied on both samples.

### RF power dependence and threshold

Typically, RF power equal to 800 W has been employed. RF equal to 1000 W (the maximum RF power of the Anelva DEA 507L machine) was also tested applying  $\text{CHF}_3$  plasma etching during 40 and 80 min to see if by increasing the RF power the fabrication process could be accelerated, but the same etching depth was obtained as shown in Fig. 3.24 (blue).

The reproducibility of the fabrication process on a lower RF power RIE machine (SAMCO, RIE-10NR) was also evaluated. In this machine, the maximum RF power is 300 W. RF power equal to 125 and 200 W was tested applying  $\text{CHF}_3$  plasma etching during 20 min. Figure 3.33 shows that only when employing RF power equal to 200 W a significant transmittance enhancement was obtained, which indicates that there is a certain RF power threshold from which surface nanostructuring process can take place. On the same machine, subsequent 10 min  $\text{O}_2$  plasma etching was also applied as cleaning process and increase of the transmittance was obtained as shown in Fig. 3.33.

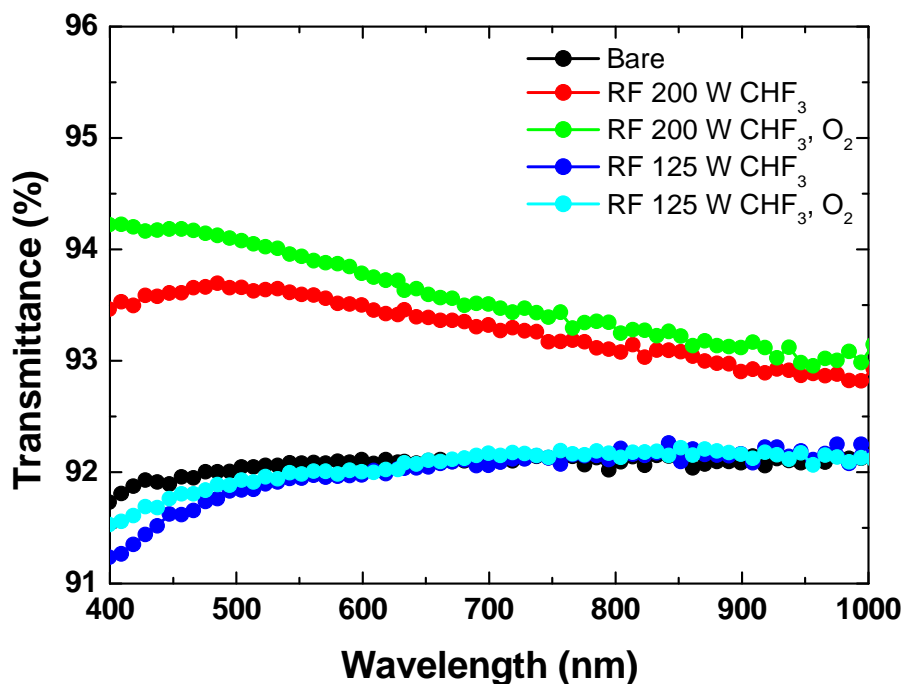


Fig. 3.33. Transmittance spectra and cross-section images of bare B270 substrates and after  $\text{CHF}_3$  (40 min) and  $\text{O}_2$  (10 min) plasma etching using a different RIE machine and at two lower RF power conditions.

### 3.3. Maskless plasma etching on various glasses

#### 3.3.1. LIBA 2000 glass

##### Optical properties

LIBA 2000 glass is the same material as the SOE in the Ventana CPV system. Since the composition of LIBA 2000 is close to the one of B270, the developed maskless  $\text{CHF}_3$  plasma etching surface nanostructuration process had potential applicability on LIBA 2000 as well.  $\text{CHF}_3$  plasma etching process was also tested during 40 min on LIBA 200 glass substrates provided by LPI. Subsequent 10 min  $\text{O}_2$  plasma etching and deionized water rinsing cleaning processes were also applied.

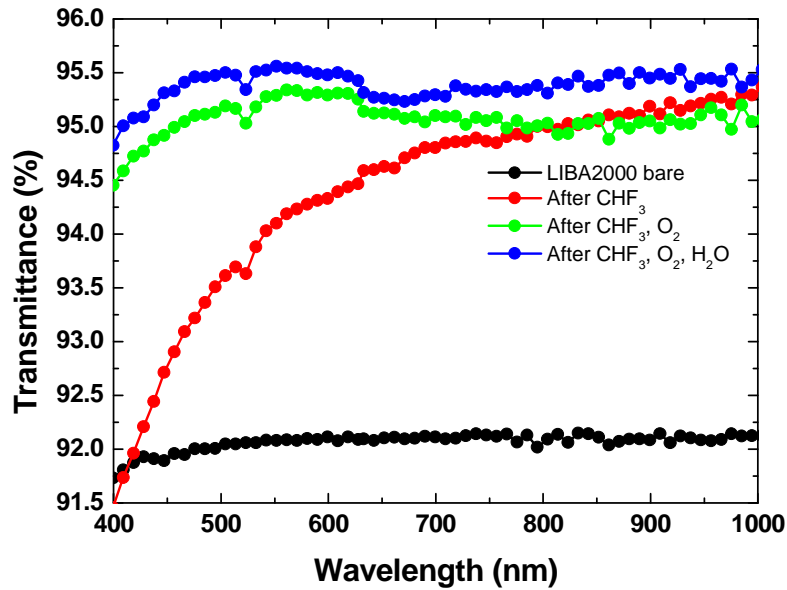


Fig. 3.34. Transmittance spectra after  $\text{CHF}_3$  (40 min) and  $\text{O}_2$  (10 min) plasma etching, and deionized water rinsing processes on one side of LIBA 2000 glass.

Figure 3.34 shows that on LIBA 2000 glass a transmittance enhancement comparable to the one obtained in B270 glass, shown in Fig 3.11, was obtained. As in B270, subsequent 10 min  $\text{O}_2$  plasma etching and deionized water rinsing cleaning processes recovered the transmittance at short wavelengths and further increased it, respectively.



### Surface morphology by AFM

Figure 3.35 shows the surface morphology on bare LIBA 2000 and after 40 min  $\text{CHF}_3$  plasma etching. The randomness and size of the top surface nanostructures obtained on LIBA 2000 after 40 min  $\text{CHF}_3$  plasma etching are comparable to the surface morphology obtained on B270 glass shown in Fig. 3.16.

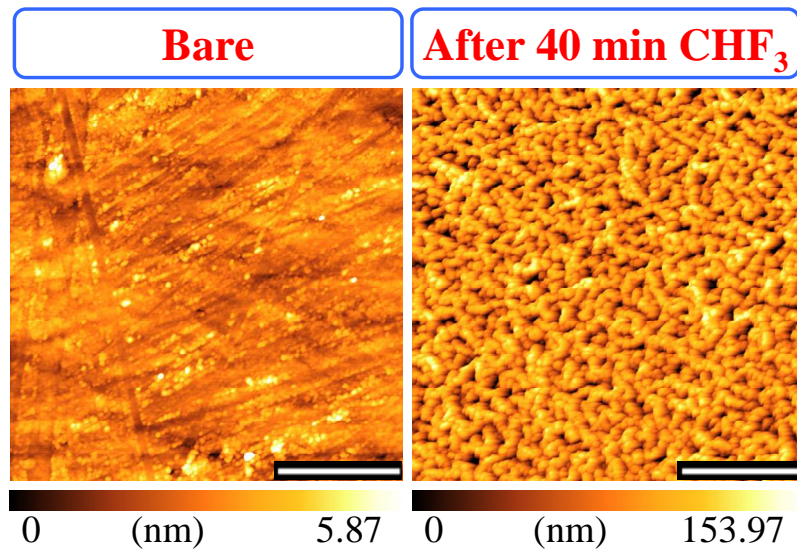


Fig. 3.35. AFM images of bare LIBA 2000 substrates (left) and after  $\text{CHF}_3$  (40 min) and  $\text{O}_2$  (10 min) plasma etching processes (right). The white bar represents  $1\mu\text{m}$ .

The transmittance enhancement and the surface morphology obtained on LIBA 2000 after 40 min  $\text{CHF}_3$  plasma etching supports the applicability of this process to glasses with similar composition to B270 glass.

The applicability of the maskless  $\text{CHF}_3$  plasma etching surface nanostructuration process on LIBA 2000 shows that this process is also potentially applicable to the curved surface of LPI's SOE or curved optical elements with compositions close to the composition of B270 glass.



### 3.3.2. Na<sub>2</sub>O-free B270 glass

A customized glass composition, Na<sub>2</sub>O-free B270, was prepared and CHF<sub>3</sub> plasma etching was applied during 40 and 80 min. The XPS results showed strong Ca 2*p*, Ca 2*s*, Auger Na KLL, and F 1*s* peaks on the surface of B270 glass after 40 min CHF<sub>3</sub> plasma etching. Figure 3.19 showed that there were NaF crystals distributed on the surface and Fig. 3.23 showed that there was not any particular accumulation of Na in the nanostructures.

There were two purposes to prepare the Na<sub>2</sub>O-free B270 sample. The first one was to elucidate whether assistance of Na<sub>2</sub>O had any particular effect on the CaF mask formation or on the surface nanostructuring process. Secondly, the Na<sub>2</sub>O-free B270 sample would help understand better the transmittance enhancement obtained after deionized water cleaning, shown in Fig. 3.11 (blue), that was attributed to the dissolution of the NaF crystals observed on the surface.

In the Na<sub>2</sub>O-free B270 sample NaF crystals are not expected to be formed, therefore no deionized water cleaning effect and maximum transmittance after the O<sub>2</sub> plasma etching cleaning process.



Fig. 3.36. Picture of the 200 g Na<sub>2</sub>O-free B270 sample just after fabrication and before cutting and polishing it for testing the role of CaO alone.

Figure 3.36 shows the 200 g Na<sub>2</sub>O-free B270 sample. The absence of Na<sub>2</sub>O modified the melting temperature, which resulted in small bubbles in the sample. Na<sub>2</sub>O-free B270 substrates were cut from the region with low bubble density and they were polished below 1 mm to reduce the effect of the bubbles. In addition, the transmittance was measured at the same point of the substrates before and after the plasma etching processes and deionized water cleaning step to limit the effect of the bubbles distribution on the optical measurements.

### Optical properties

Broadband transmittance enhancement was obtained on Na<sub>2</sub>O-free B270 glass substrates after CHF<sub>3</sub> and subsequent O<sub>2</sub> plasma etching as shown is Fig. 3.37. Figure 3.37 also shows no significant transmittance profile modification after deionized water rinsing.

These results supports that the origin of the transmittance enhancement after deionized water rinsing observed in Fig 3.11 (blue) was de dissolution of NaF crystals and that despite the decrease of the Ca 2*p*, Ca 2*s* peaks in the XPS spectra after deionized water rinsing, the plausible partial (Ca, F) self-generated mask removal from the tips of the nanostructures has no significant effect on the transmittance profile.

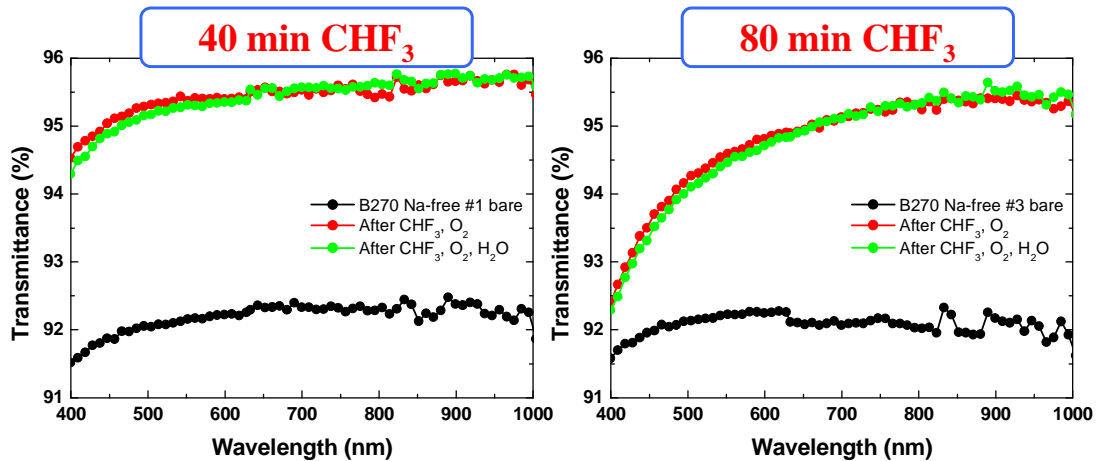


Fig. 3.37. Transmittance spectra after CHF<sub>3</sub> (40-80 min) and O<sub>2</sub> (10 min) plasma etching, and deionized water rinsing processes on one side of Na<sub>2</sub>O-free B70 substrates.

## Surface morphology by AFM

The transmittance enhancement obtained after 40 min is comparable to the one obtained in B270 glass shown in Fig. 3.11, but even after the  $O_2$  plasma etching process the transmittance enhancement is still low at short wavelengths after 80 min treatment. This decrease could be explained by the larger structures observed on Fig. 3.38 (right). Figure 3.38 also shows that after 40 min  $CHF_3$  plasma etching treatment the morphology is comparable to the one obtained in B270, which indicates that after sustained  $CHF_3$  plasma etching there is a structure size increase that was not observed in B270.

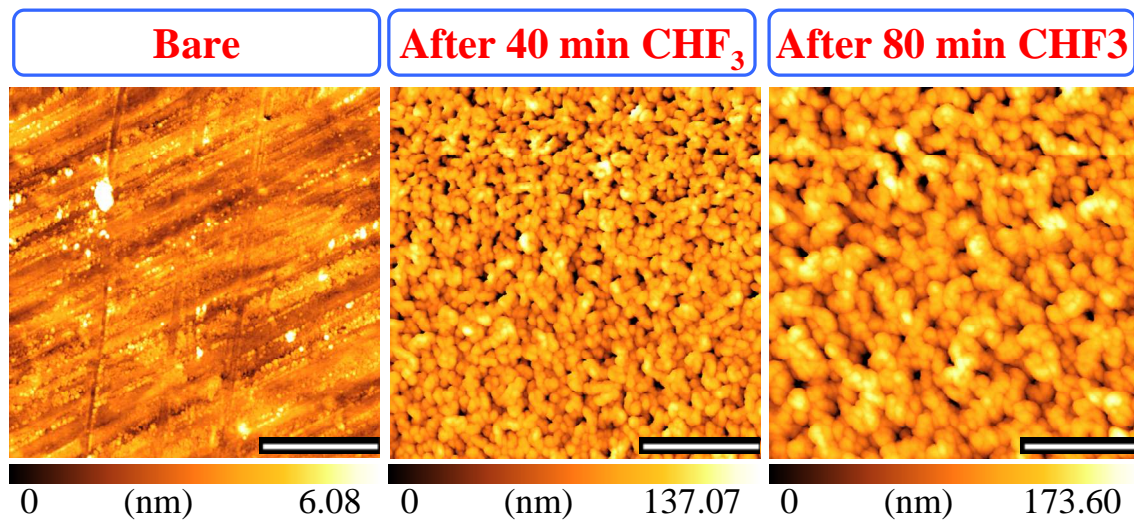


Fig. 3.38. AFM images of bare  $Na_2O$ -free B70 substrates (left), after  $CHF_3$  (40 min) and  $O_2$  (10 min) (middle), and after  $CHF_3$  (80 min) and  $O_2$  (10 min) (right) plasma etching processes. The white bar represents 1  $\mu m$ .

In conclusion, broadband transmittance enhancement was also obtained on  $Na_2O$ -free B270 glass, which means that  $CaO$  alone contained in the glass, under  $CHF_3$  plasma etching forms the (Ca, F) self-generated mask and allows the fabrication of high aspect ratio nanostructures. On treated  $Na_2O$ -free B270 substrates, the absence of transmittance profile modification after deionized water rinsing confirmed that the transmittance gain observed in B270 resulted from the dissolution of  $NaF$  crystals and that dissolution of (Ca, F) does not affect the transmittance. Finally, the absence of  $Na_2O$  may accelerate or modify the fabrication over 40 min  $CHF_3$  plasma etching where larger structures appeared.

### 3.3.3. Quartz

#### Surface morphology by AFM

To evaluate the  $\text{CHF}_3$  plasma etching process on high purity bulk  $\text{SiO}_2$  samples, quartz substrates were also tested. Fig. 3.39 shows that the surface of quartz was not textured after the  $\text{CHF}_3$  plasma etching process, only very small sparsely dots appeared.

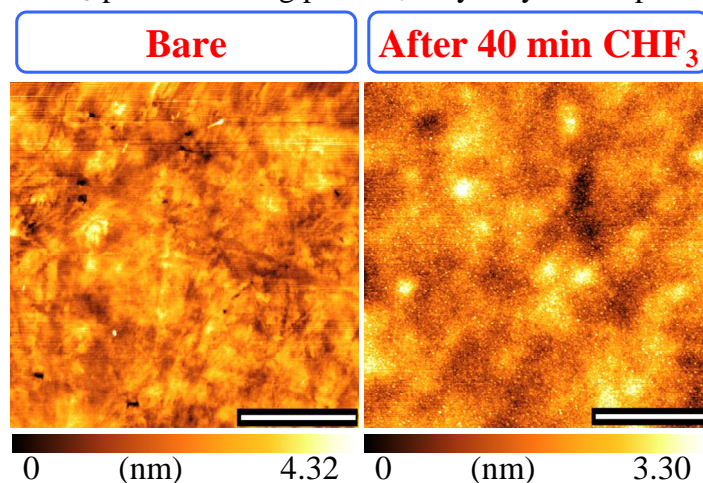


Fig. 3.39. AFM images of bare quartz substrates (left) and after  $\text{CHF}_3$  (40 min) and  $\text{O}_2$  (10 min) plasma etching processes (right). The white bar represents 1  $\mu\text{m}$ .

#### Surface composition by XPS

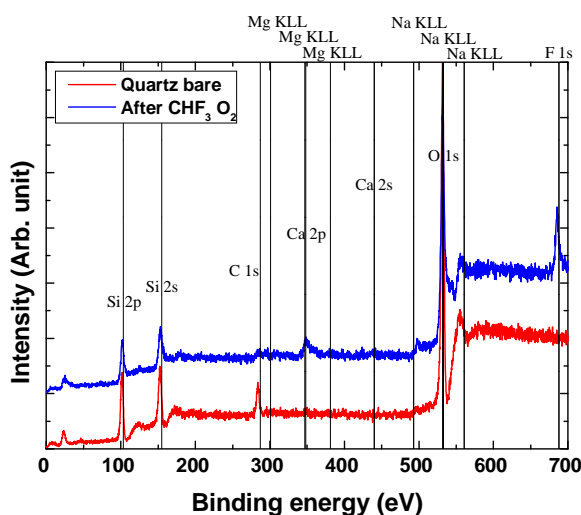


Fig. 3.40. XPS spectra carried out on quartz substrates before and after the  $\text{CHF}_3$  (40 min) and  $\text{O}_2$  (10 min) plasma etching processes.

Figure 3.40 shows the XPS results on quartz before and after  $\text{CHF}_3$  and  $\text{O}_2$  plasma etching processes. In bare quartz substrates, the Si  $2p$  (103.5 eV), Si  $2s$  (155 eV), and O  $1s$  (533 eV) peaks were clearly observed. Also, a contamination related C  $1s$  (287 eV) peak was observed. After  $\text{CHF}_3$  and  $\text{O}_2$  plasma etching processes, Si  $2p$ , Si  $2s$ , and O  $1s$  peaks are reduced, but remained dominant. On treated quartz, the observed small Ca  $2p$ , Ca  $2s$ , Auger Na KLL, and F  $1s$  peaks may correspond to the small dots observed in Fig. 3.39 that arised from Ca and Na impurities on the quartz substrates or from volatized species from neighbor samples.

### 3.3.4. Soda Lime glass

#### Optical properties

According to the MSDS data shown in Table 1, the main difference between soda-lime and B270 compositions is the MgO content, which is absent in B270. Typical soda-lime glasses used for windows contain over 5% of MgO, which reduces the melting point and reduces the fabrication costs.

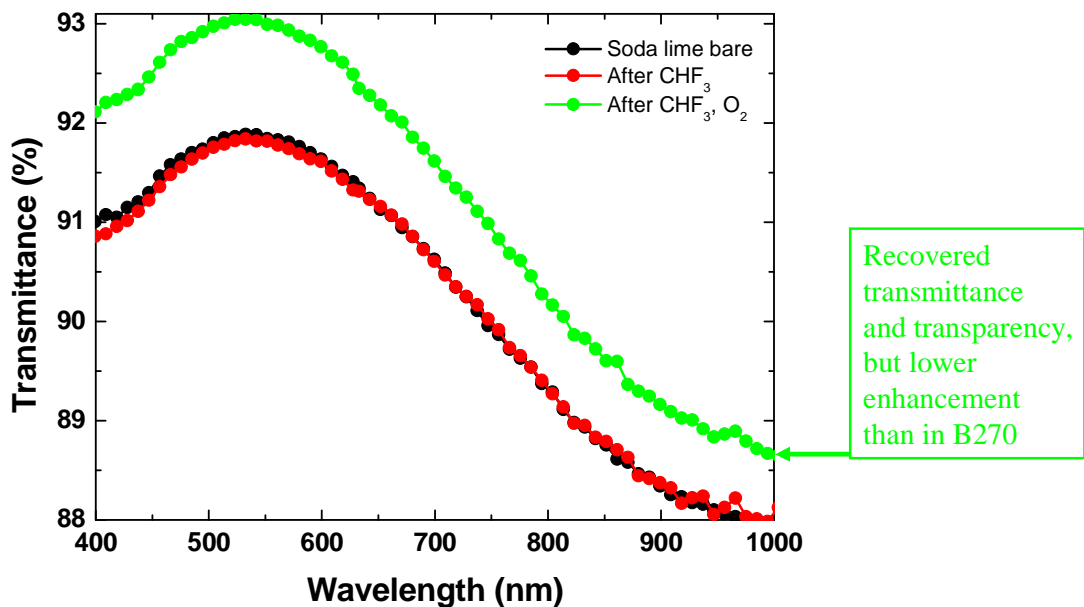


Fig. 3.41. Transmittance spectra after  $\text{CHF}_3$  (40 min) and  $\text{O}_2$  (10 min) plasma etching on one side of soda lime glass.



After applying  $\text{CHF}_3$  and  $\text{O}_2$  plasma etching processes on soda-lime glass, Fig. 3.41 shows that the transmittance enhancement in textured soda-lime was lower than in textured B270. Since the sole composition difference between B270 and soda-lime is the MgO content, this result means that MgO content and its (Mg, F) self-generated mask under  $\text{CHF}_3$  plasma etching had a negative effect on the surface nanostructuration process. More analysis of the self-generated masks is introduced in section 3.4.

### Surface morphology by AFM and SEM

The subwavelength nature of the structures formed in soda-lime that originated the small antireflection effect is shown in Fig. 3.42, which appears to be like high density aggregation of small dots. From the AFM image and the low transmittance enhancement, the formation of high aspect ratio nanostructures on treated soda-lime, seems unlikely.

Figure 3.43 shows an SEM image of the surface of soda-lime after 40 min  $\text{CHF}_3$  plasma etching where NaF crystals and untextured areas can be observed.

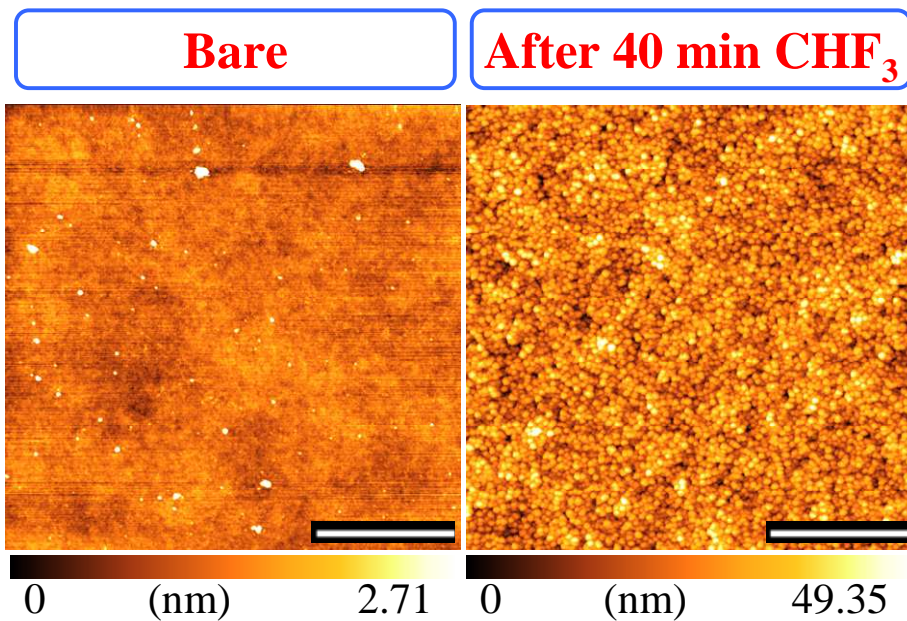


Fig. 3.42. AFM images of bare Soda Lime substrates (left) and after  $\text{CHF}_3$  (40 min) and  $\text{O}_2$  (10 min) plasma etching processes (right). The white bar represents 1  $\mu\text{m}$ .

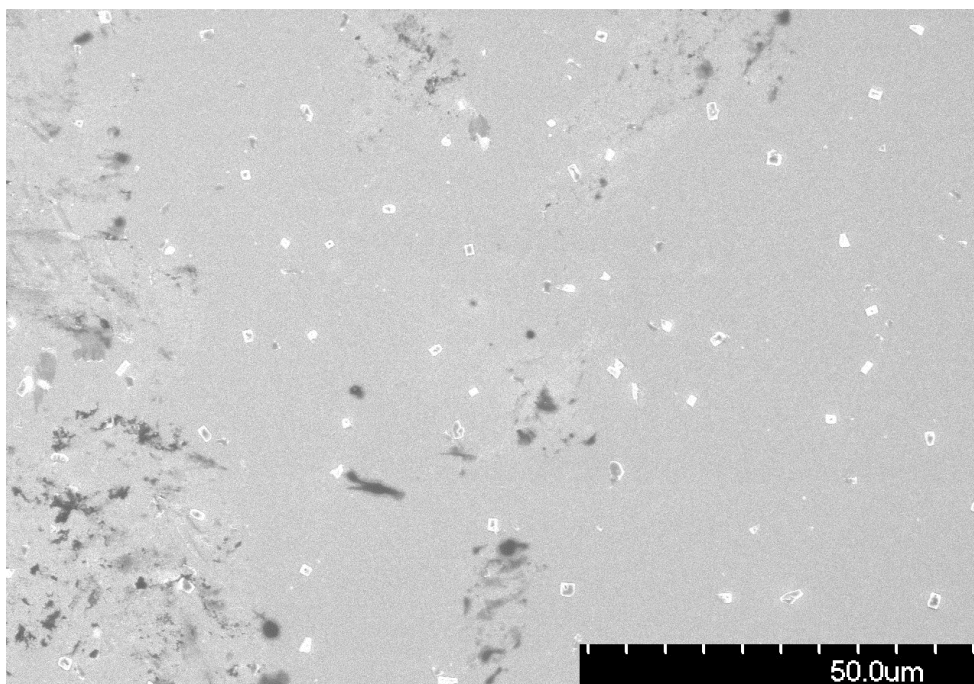


Fig. 3.43. SEM image of the surface of Soda Lime after 40 min  $\text{CHF}_3$  plasma etching.

### Surface composition by XPS

Figure 3.44 shows the XPS results on soda-lime substrate before and after  $\text{CHF}_3$  and  $\text{O}_2$  plasma etching processes. In agreement with the MSDS data summarized in Table 1, on bare soda-lime, small Auger Mg KLL (301 eV, 347 eV, 381 eV), Ca 2p, Ca 2s, and Auger Na KLL peaks were observed. After  $\text{CHF}_3$  and  $\text{O}_2$  plasma etching processes, Auger Mg KLL, Ca 2p, Ca 2s, Auger Na KLL, and F 1s peaks became dominant, but Si 2p, Si 2s, and O 1s peaks were still visible.

SEM-EDX surface analysis on soda-lime, determined that the crystals on the surface were NaF as in B270 and that on the soda-lime treated surface the untextured areas had similar composition compared to the bulk, which explains the presence of these peaks after the plasma etching processes. The diameter of the XPS beam is approximately 500  $\mu\text{m}$ ; therefore the untextured areas in soda-lime are unavoidably included in the measurements. In B270 glass, the Ca 2p, Ca 2s, Auger Na KLL, and F 1s peaks were observed after  $\text{CHF}_3$  and  $\text{O}_2$  plasma etching processes, but in soda-lime in addition to those peaks, the Auger Mg KLL peaks are also observed, which means that, in some form, the surface composition of treated soda-lime also contains the self-generated (Mg, F) mask.

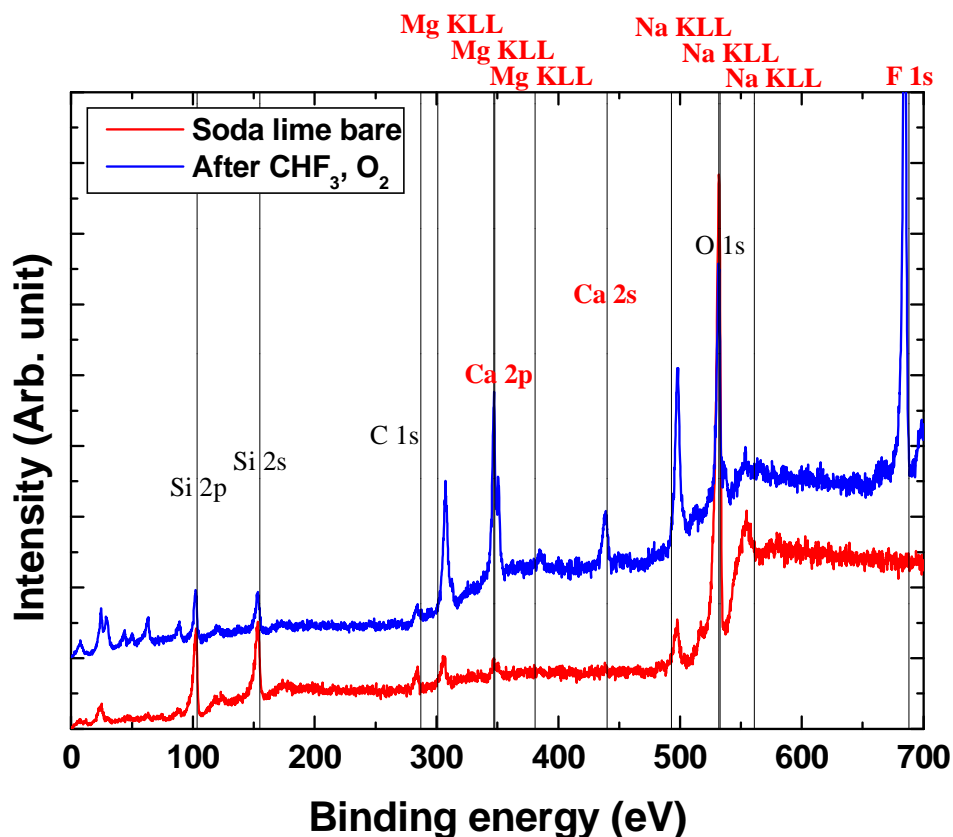


Fig. 3.44. XPS spectra carried out on Soda Lime substrates before and after the  $\text{CHF}_3$  (40 min) and  $\text{O}_2$  (10 min) plasma etching processes.

### 3.3.5. D263 glass

D263 (Schott AG) glass is a type of borosilicate glass. According to the MSDS data shown in Table 1, the main difference between D263 and B270 compositions is the absence of CaO content in D263, which is present B270. B270 glass contains CaO and  $\text{Na}_2\text{O}$ . Section 3.3.2 described the effect of the absence of  $\text{Na}_2\text{O}$  in B270 that was studied by the preparation of a  $\text{Na}_2\text{O}$ -free B270 glass sample.

Detailed composition of D263 showed very low MgO content, but it is not shown here due to intellectual property reasons.

Within some approximation, D263 glass represents the CaO-free B270 glass composition, which allows to study the effect of the absence of CaO in B270 and also the behavior of the (Na, F) self-generated mask alone.



## Optical properties

Figure 3.45 shows the transmittance and the diffuse reflectance measured on D263 textured surfaces, which is consistent with the one reported using  $\text{CF}_4$  plasma etching in [50]. After applying  $\text{CHF}_3$  and  $\text{O}_2$  plasma etching processes on D263 glass, the transmittance decreased owing to the light scattering that resulted from large structures on the treated surface shown in Fig. 3.46. In fact, textured D263 substrates showed white surface after the  $\text{CHF}_3$  process. In the case of treated D263 glass, the  $\text{O}_2$  plasma etching process appears to be wavelength dependent, though no significant morphological change was observed before and after  $\text{O}_2$  plasma etching.

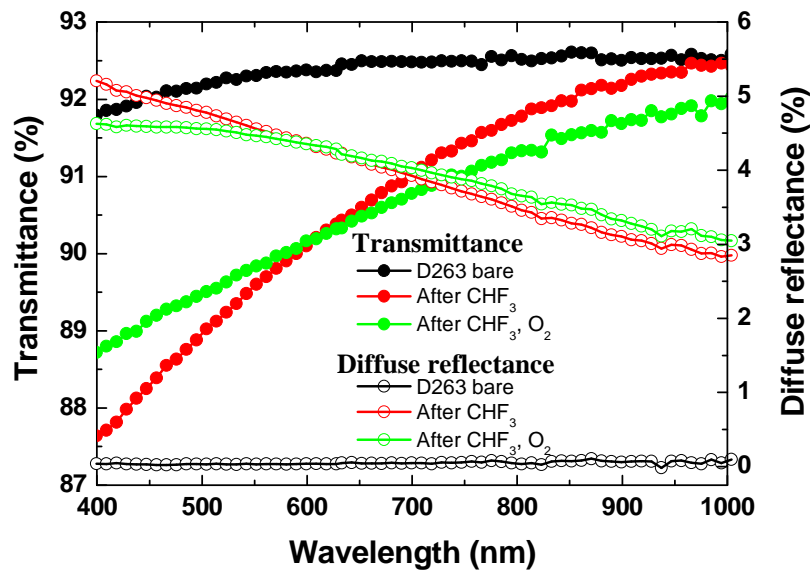


Fig. 3.45. Transmittance and diffuse reflectance spectra after  $\text{CHF}_3$  (40 min) and  $\text{O}_2$  (10 min) plasma etching on one side of D263 glass.

## Surface morphology by AFM and SEM

Figure 3.47 shows an enlarged SEM image of the large size structures on the treated D263 surface after 40 min  $\text{CHF}_3$  plasma etching that originated the scattering effect. It has been reported that the scattering properties can be tuned by adjusting the plasma etching parameters or the assistance mask characteristics to achieve desired scattering properties that can be applied to improve solar cells, OLEDs, or other applications [44, 49].

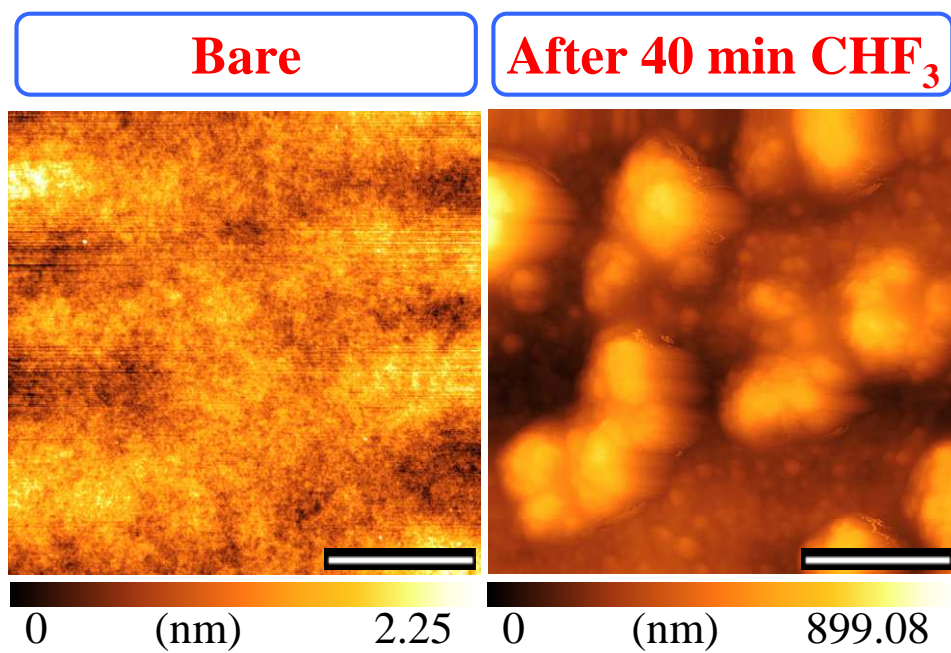


Fig. 3.46. AFM images of bare D263 substrates (left) and after CHF<sub>3</sub> (40 min) and O<sub>2</sub> (10 min) plasma etching processes (right). The white bar represents 1 μm.

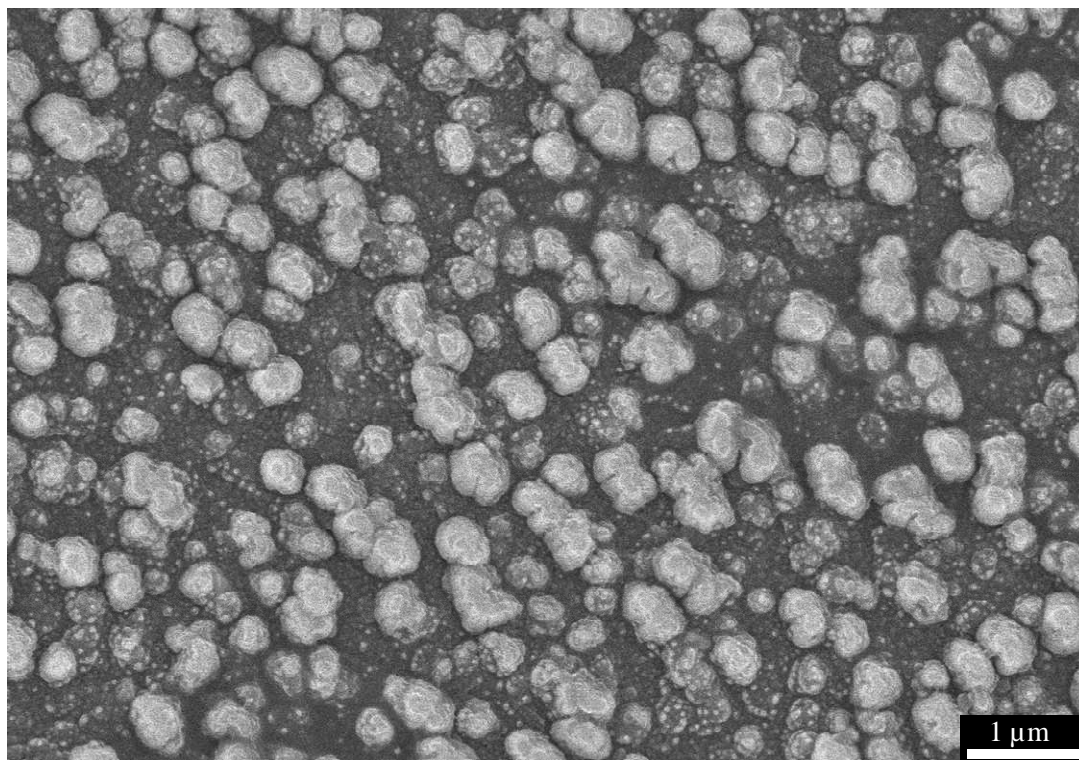


Fig. 3.47. SEM image of the surface of D263 after 40 min CHF<sub>3</sub> plasma etching.

## Surface composition by XPS

Figure 3.48 shows the XPS results on D263 glass before and after  $\text{CHF}_3$  and  $\text{O}_2$  plasma etching processes. In agreement with the MSDS data summarized in Table 1, on bare D263, small Auger Na KLL peaks were observed. After  $\text{CHF}_3$  and  $\text{O}_2$  plasma etching processes, Auger Na KLL, and F 1s peaks became dominant indicating that the surface is mostly covered by the self-generated (Na, F) mask. On B270 and soda-lime, the Auger Na KLL peaks corresponded to NaF crystals, but NaF crystals were not observed on the surface of treated D263 as shown in Fig. 3.47. D263 samples were also immersed in ultrasonic bath of deionized water, but the transparency was not recovered, which indicates the large structures shown in Fig. 3.47 are not made of (Na, F), but that the (Na, F) self-generated mask induced their fabrication and (Na, F) remained on their surface. Scattering surface on D263 has also been reported using  $\text{CF}_4$  maskless plasma etching [49]. More analysis of the self-generated masks is introduced in section 3.4. Compared to the XPS spectra obtained on soda-lime after  $\text{CHF}_3$  and  $\text{O}_2$  plasma etching processes, on the surface of treated D263 there is no strong (Mg, F) content, which supports the low MgO content in D263.

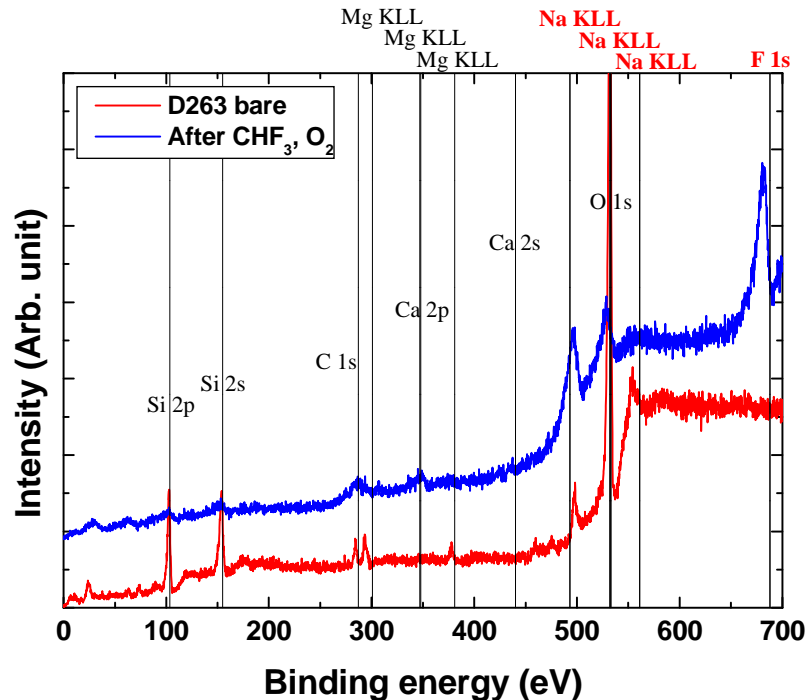


Fig. 3.48. XPS spectra carried out on D263 substrates before and after the  $\text{CHF}_3$  (40 min) and  $\text{O}_2$  (10 min) plasma etching processes.

### 3.3.6. Qioptiq space cover glasses

The  $\text{CHF}_3$  maskless plasma etching surface nanostructuring process was also tested on the three types cover glasses (CMG, CMX, and CMO), provided by Qioptiq that used to protect the solar cells in space. Due to intellectual property reasons, the detailed composition the three cover glasses employed to protect the solar cells in space is not disclosed. Although, it is known that in order to protect the solar cells in space the cover glasses are doped with a certain amount of  $\text{CeO}_2$  because it stands strong UV, electron, and proton irradiation condition in common in space.

#### Optical properties

The transmittance enhancement on CMG, CMX, and CMO after applying  $\text{CHF}_3$  during 40 min and subsequent 10 min  $\text{O}_2$  plasma etching and deionized water cleaning processes are shown in Fig. 3.49, Fig. 3.50, and Fig. 3.51, respectively. Also, the transmittance spectra of the bare glasses and their transmittance spectra when coated with typical AR coating are also shown in Fig. 3.49, Fig. 3.50, and Fig. 3.51.

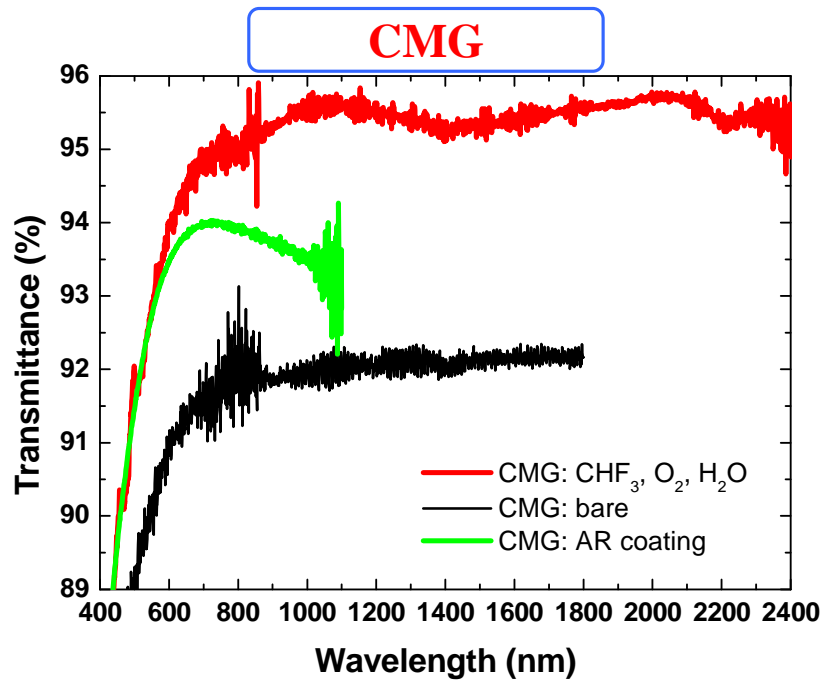


Fig. 3.49. Transmittance spectra of bare CMG substrate, CMG substrates using typical AR coating, and after  $\text{CHF}_3$  (40 min),  $\text{O}_2$  (10 min) plasma etching, and deionized water rinsing processes on one side.

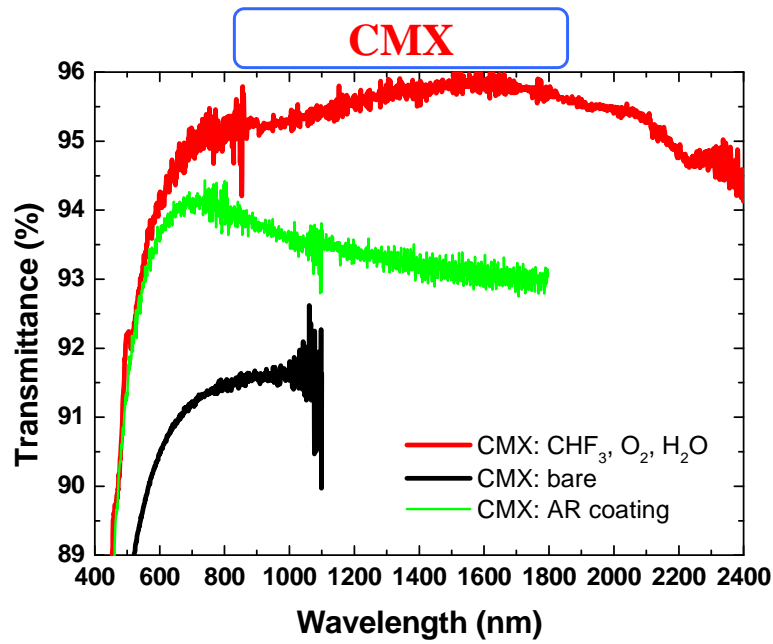


Fig. 3.50. Transmittance spectra of bare CMX substrate, CMX substrates using typical AR coating, and after CHF<sub>3</sub> (40 min), O<sub>2</sub> (10 min) plasma etching, and deionized water rinsing processes on one side.

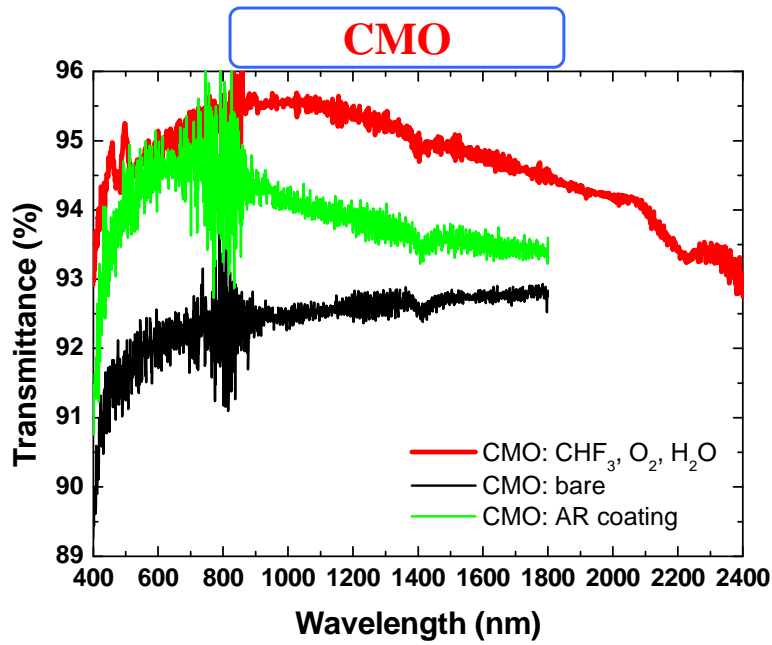


Fig. 3.51. Transmittance spectra of bare CMO substrate, CMO substrates using typical AR coating, and after CHF<sub>3</sub> (40 min), O<sub>2</sub> (10 min) plasma etching, and deionized water rinsing processes on one side.



The transmittance enhancement obtained by applying the developed  $\text{CHF}_3$  maskless plasma etching surface nanostructuring process outperformed the performance of typical AR coatings on the three space cover glasses as shown in Fig. 3.49, Fig. 3.50, and Fig. 3.51. In particular very broadband transmittance enhancement was obtained on CMG.

### Surface morphology by AFM and SEM

The subwavelength nature of the structures that originated the antireflection effect on CMG, CMX, and CMO after 40 min  $\text{CHF}_3$  plasma etching is shown in Fig. 3.52, Fig. 3.53, and Fig. 3.54, respectively. The bare surfaces on the three types of space cover glasses appear flat, but covered by high density nano-dots. This surface finishing is the one obtained after fabrication without further polishing. The size of the nanostructures formed on the surface of the three space cover glasses is smaller than the one of the obtained in B270 glass after 40 min  $\text{CHF}_3$  plasma etching. Also, the formation of some aggregates, especially on the treated surface of CMX and CMO, is shown in Fig. 3.52, Fig. 3.53, and Fig. 3.54, respectively.

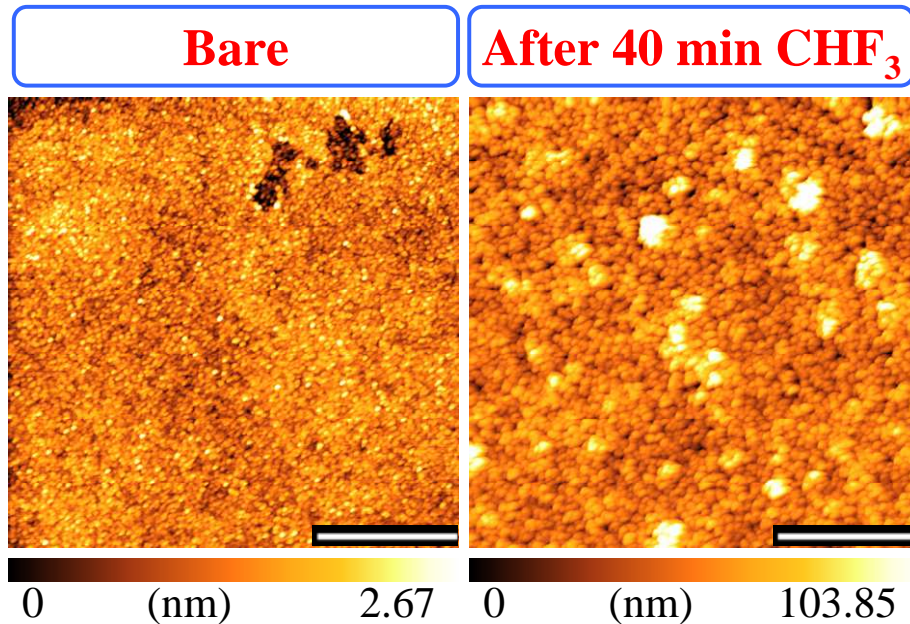


Fig. 3.52. AFM images of bare CMG substrates (left) and after  $\text{CHF}_3$  (40 min),  $\text{O}_2$  (10 min) plasma etching and deionized water rinsing processes (right). The white bar represents 1 μm.

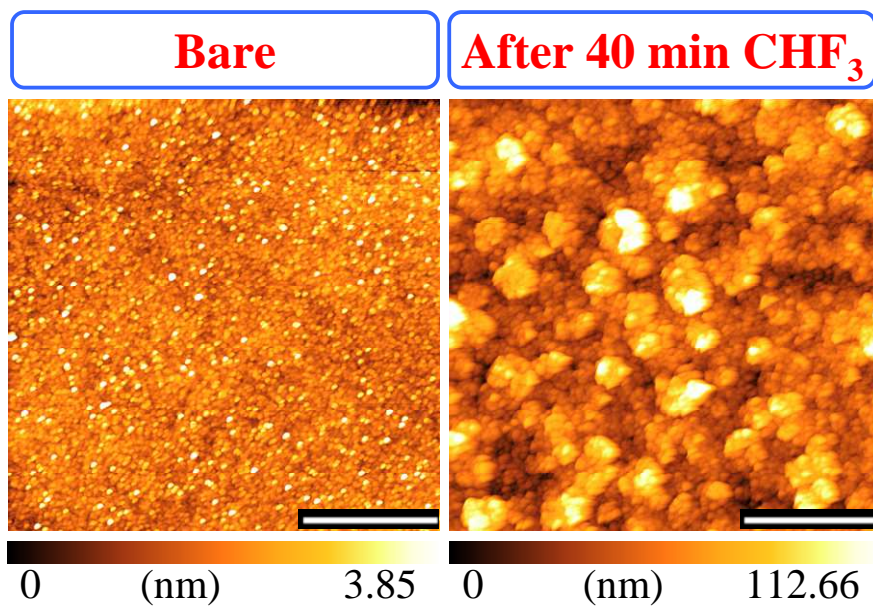


Fig. 3.53. AFM images of bare CMX substrates (left) and after CHF<sub>3</sub> (40 min), O<sub>2</sub> (10 min) plasma etching and deionized water rinsing processes (right). The white bar represents 1μm.

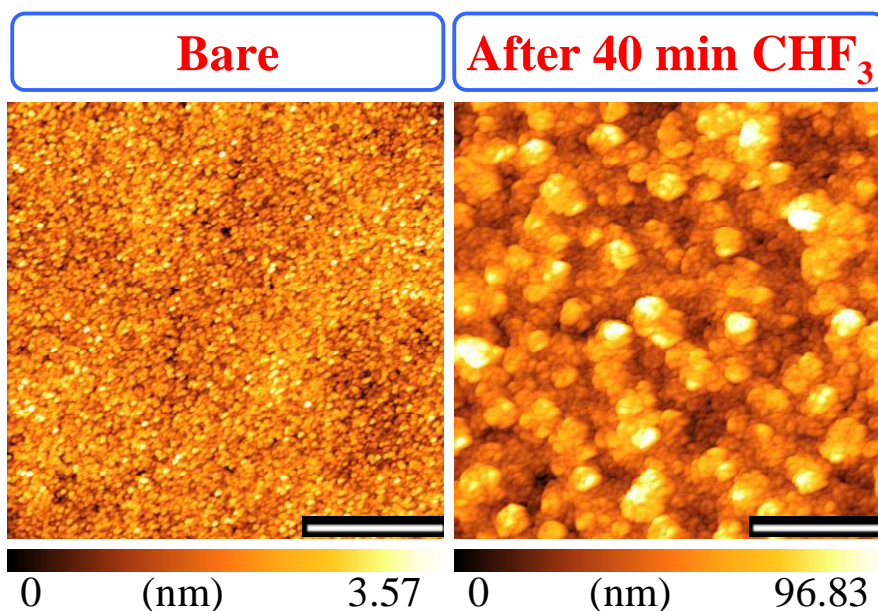


Fig. 3.54. AFM images of bare CMO substrates (left) and after CHF<sub>3</sub> (40 min), O<sub>2</sub> (10 min) plasma etching and deionized water rinsing processes (right). The white bar represents 1μm.

## Surface composition by XPS

On CMG, CMX, and CMO space cover glasses, the XPS spectra was measured on the bare surface and after  $\text{CHF}_3$  and  $\text{O}_2$  plasma etching and deionized water rinsing processes. On the bare surfaces, the Si 2p (103.5 eV), Si 2s (155 eV), and O 1s (533 eV) peaks were clearly observed as shown in Fig. 3.55, Fig. 3.56, and Fig. 3.57. Due to intellectual property reasons, the detailed composition is not disclosed, but CMG contains  $\text{Na}_2\text{O}$ , but does not contain CaO or MgO. CMX contains  $\text{Na}_2\text{O}$ , CaO, and MgO. CMO does not contain  $\text{Na}_2\text{O}$ , CaO, or MgO. Finally, the three of them contain  $\text{CeO}_2$ . After  $\text{CHF}_3$  and  $\text{O}_2$  plasma etching and deionized water rinsing processes, in agreement with the details on the composition, small peaks of each element are observed on the XPS spectra of each type of space cover glasses. Also, on the treated surfaces of the three space cover glasses small F 1s (688 eV), Auger F KLL (832 eV), Ce 3d<sub>5/2</sub> (884 eV) and Ce 3d<sub>3/2</sub> (902 eV) peaks are shown in the XPS spectra. In addition to these peaks, particularly in CMO, Ba 4d (91 eV), Ba 3d<sub>5/2</sub> (781 eV), and Ba 3d<sub>3/2</sub> (796 eV) peaks were observed. On B270, after rinsing the Ca, Na, and F peaks decreased. The results on space cover glasses show that mainly (Ce, F), but also (Ba, F) self-generated masks are still present on the nanostructured surfaces after deionized water rinsing, indicating that the (Ce, F) and (Ba, F) self-generated masks originated the nanostructured surface. The surface nanostructuration by (Ce, F) and (Ba, F) self-generated masks is in particular confirmed in CMG and CMO because they do not contain CaO.

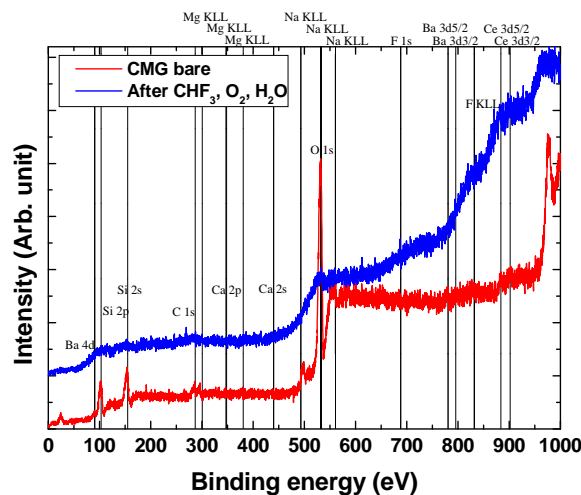


Fig. 3.55. XPS spectra carried out on bare CMG substrates and after  $\text{CHF}_3$  (40 min),  $\text{O}_2$  (10 min) plasma etching, and deionized water rinsing processes.



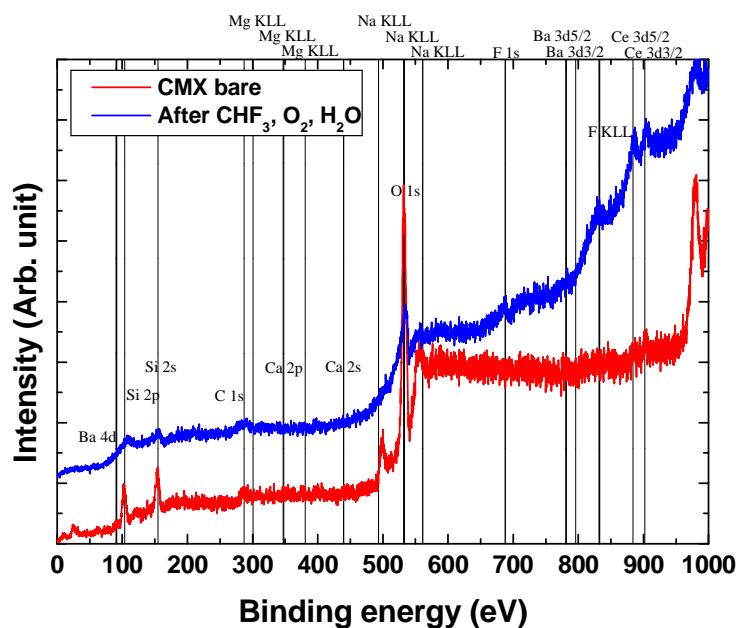


Fig. 3.56. XPS spectra carried out on bare CMX substrates and after CHF<sub>3</sub> (40 min), O<sub>2</sub> (10 min) plasma etching, and deionized water rinsing processes.

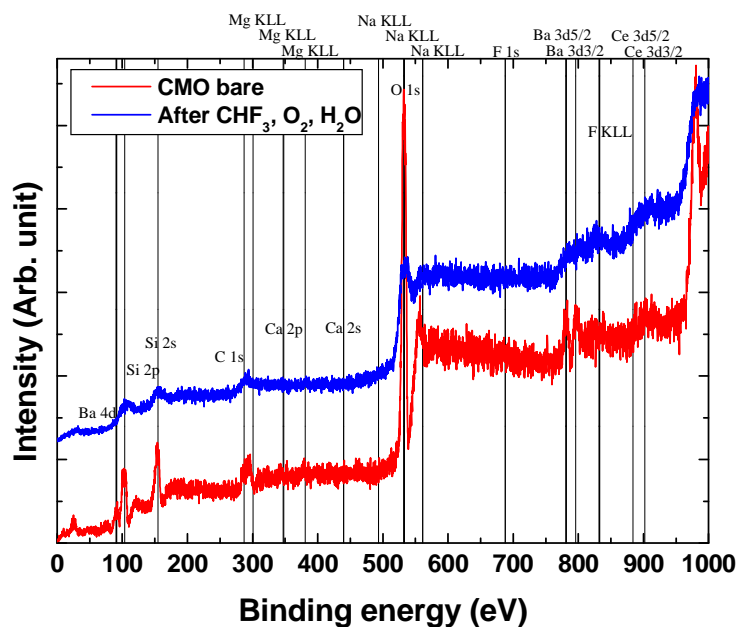


Fig. 3.57. XPS spectra carried out on bare CMO substrates and after CHF<sub>3</sub> (40 min), O<sub>2</sub> (10 min) plasma etching, and deionized water rinsing processes.

### 3.4. Self-generated masks under maskless plasma etching

The bare surface of all the glasses that were studied had high surface flatness and it was comparable for all samples. However, some of the obtained surface morphologies were considerably different after undergoing the same 40 min  $\text{CHF}_3$  plasma etching process. The difference between each glass is its composition and it was shown that there is a strong relation between the glass composition and the obtained surface morphology. Only in the case of quartz there was no surface nanostructuration owing to its high  $\text{SiO}_2$  purity. Also in quartz there was not significant surface composition modification after the plasma etching processes.

On all tested glasses it was shown that the surface nano-microstructuration was accompanied by the surface composition modification evidenced by the decrease of Si and O. The other elements were in the original glasses as oxides, but always found together with F indicating the fluoride formation. It is plausible that the sustained  $\text{CHF}_3$  plasma etching resulted in the fluoride compound formation on the surface of the nano-microstructures.

The boiling point is one of the characteristics that determine the volatility of reaction products during plasma etching [59]. For example,  $\text{SiF}_4$  and  $\text{BF}_3$  are highly volatile species [60] with low boiling points  $-86^\circ\text{C}$ , and  $-100.3^\circ\text{C}$ , respectively. For this reason, Si peaks in the XPS measurements decreased after plasma etching and B peaks were barely observed.

Thin metallic layers are used as assistance mask to obtain scattering surface.  $\text{CuF}$  is generated as a reactive product when thin Cu films are exposed to  $\text{CF}_4$  plasma etching. Despite its high boiling point of  $1100^\circ\text{C}$ , this mask is removed after several minutes of plasma etching [51, 52]. After  $\text{CHF}_3$  plasma etching, strong fluoride species with high boiling points could be formed as follows,  $\text{CaF}_2$   $2553^\circ\text{C}$ ,  $\text{CeF}_3$   $2300^\circ\text{C}$ ,  $\text{BaF}_2$   $2260^\circ\text{C}$ ,  $\text{MgF}_2$   $2260^\circ\text{C}$ , and  $\text{NaF}$   $1704^\circ\text{C}$ . All these fluorides have higher boiling points than  $\text{CuF}$ . The lattice energies of the fluoride species that could be formed by the interaction of the oxides in the glass and the  $\text{CHF}_3$  plasma etching are as follows:  $\text{CeF}_3$   $4915 \text{ kJmol}^{-1}$ ,  $\text{MgF}_2$   $2913 \text{ kJmol}^{-1}$ ,  $\text{CaF}_2$   $2609 \text{ kJmol}^{-1}$ ,  $\text{BaF}_2$   $2341 \text{ kJmol}^{-1}$ , and  $\text{NaF}$   $910 \text{ kJmol}^{-1}$  [61, 62]. Their ionic radius is as follows  $\text{Ba}^{2+}$   $1.35 \text{ \AA}$ ,  $\text{Ce}^{3+}$   $1.15 \text{ \AA}$ ,  $\text{Ca}^{2+}$   $1.00 \text{ \AA}$ ,  $\text{Na}^{1+}$   $0.99 \text{ \AA}$ , and  $\text{Mg}^{2+}$   $0.57 \text{ \AA}$  [63].

Based on the characteristic of the reactive products and the optical, morphological, and surface composition measurements, a possible explanation of the role of the glass composition is proposed as follows.

Depending on the specific oxides contained in each type of glass, after sustained  $\text{CHF}_3$  plasma etching, different surface morphologies can be obtained. In the fabrication process, F from the  $\text{CHF}_3$  plasma combines with the ionic species present in each type of glass *i.e.*  $\text{Si}^{4+}$ ,  $\text{B}^{3+}$ ,  $\text{O}^{2+}$ ,  $\text{Ca}^{2+}$ ,  $\text{Ce}^{3+}$ ,  $\text{Ba}^{2+}$ ,  $\text{Mg}^{2+}$ , and  $\text{Na}^+$ . Through their combination, owing to their low boiling point, some species are evaporated resulting in selective removal such as  $\text{SiF}_4$ ,  $\text{BF}_3$ , and,  $\text{OF}_2$ . Other species self-generate masks ( $\text{CaF}_2$ ,  $\text{CeF}_3$ ,  $\text{BaF}_2$ ,  $\text{MgF}_2$ , and  $\text{NaF}$ ) that are formed and deposited on the surface.

The high temperature induced by ion bombardment could activate surface diffusion of the ions and assist their migration to form the self-generated fluoride masks, as has been reported in Ga atoms that migrate and form aggregates on the surface of GaN films under Ar an  $\text{N}_2$  plasma etching [64]. The temperature assisted surface diffusion of the ions could also explain the formation of the NaF crystals on the surface of B270 and soda-lime glasses, where gradual  $\text{Na}^+$  ions migration resulted in NaF crystals growth on these treated surfaces. The absence of NaF crystals on the surface of D263 glass suggests that depending on the combination of ionic species migrating on the surface, different crystal or amorphous structures can be obtained. In the presence of  $\text{Ca}^{2+}$  or  $\text{Ca}^{2+}$  and  $\text{Mg}^{2+}$  species, NaF crystals were obtained, but in their absence (Na, F) self-generated mask was formed in amorphous phase. Also, this amorphous phase is at the origin of the large scattering surfaces observed on the surface of treated D263.

The combination of ionic species dependence, could also explain the reason why in the presence of  $\text{Mg}^{2+}$  ions, the formation of high aspect ratio nanostructures by the self-generated CaO mask was inhibited in soda-lime glass.

Under sustained  $\text{CHF}_3$  plasma etching, the self-generated masks undergo continuous physical and chemical etching. Since the self-generated masks are fluorides, the chemical etching is low or absent. Therefore, they are mainly subjected to physical etching, which decompose them in different proportions depending on their volatility, which depends on their boiling point [59]. Also, the lattice energy is a key parameter because the etching rate decreases for high lattice energy materials [65, 66].

In terms of boiling point and lattice energy, among the self-generated masks, (Na, F) is the weakest one, which means that it is the mask with the highest possibility to be decomposed under sustained physical etching. Re-self-generation of the (Na, F) mask is plausible because ions from the decomposed mask may remain on the surface and the glass itself contains  $\text{Na}_2\text{O}$  that can provide more ions to re-self-generate the (Na, F) mask. Sustained  $\text{CHF}_3$  plasma etching on D263 glass surface and the repetitive decomposition and re-self-generation processes of (Na, F) mask may explain the fabrication process to obtain the large scattering structures shown in Fig. 3. 47.

Re-self-generation of the (Ca, F) mask was introduced in section 3.2.7 where it was admitted that in order to 1) the etching depth to increase with CHF<sub>3</sub> plasma etching time, 2) the pillar aspect ratio to increase with CHF<sub>3</sub> plasma etching time, and 3) the (Ca, F) self-generated mask to be only accumulated at the tip of the nanostructures, (Ca, F) had to be decomposed and re-self-generated under sustained CHF<sub>3</sub> plasma etching while the aspect ratio of the pillars increased.

The same principle of repetitive decomposition and re-self-generation processes occur to the (Ca, F) and (Na, F) self-generated masks under sustained CHF<sub>3</sub> plasma etching, but, very different morphologies and antireflection and scattering effects were obtained, indicating that the nature of the mask itself determines the morphologies and therefore the corresponding optical properties obtained. The ion sizes of Ca<sup>2+</sup> and Na<sup>+</sup> are about the same therefore, the lower boiling point and lower lattice energy of NaF compared to CaF<sub>2</sub> could explain that higher etching ratio of (Na, F) results in the formation of a scattering surface made of large structures. Other parameters of the plasma etching process could also influence the geometries obtained, but they are outside the scope of this study.

In B270 and Na<sub>2</sub>O-free B270, broadband antireflection enhancement was obtained despite the fact that B270 contained both CaO and Na<sub>2</sub>O, but Na<sub>2</sub>O-free B270 only contained CaO. This result suggests that perhaps when several self-generated mask coexist, the effect of the strongest one prevails. The case of B270 and soda-lime is particularly interesting because in these two cases the presence of (Ca, F) and (Mg, F) resulted in the gradual growth of NaF crystals on the treated surfaces. The specific case of soda-lime is of particular importance because only in this case despite the high boiling points and high lattices energies of CaF<sub>2</sub> and MgF<sub>2</sub>, the transmittance enhancement was degraded by the inhibition of the fabrication of high aspect ratio nanostructures. The small ionic radius of Mg<sup>2+</sup> compared to the ionic radius of Ca<sup>2+</sup> could explain this result because the ionic radius of Mg<sup>2+</sup> is about half the ionic radius of Ca<sup>2+</sup>. Through the repetitive decomposition and re-self-generation processes of the (Ca, F) and (Mg, F) self-generated masks, the migration of a significantly smaller Mg<sup>2+</sup> ion may disrupt the fabrication of a strong mask that can sustain the physical etching to fabricate high aspect ratio nanostructures. In addition uncovered areas were observed on the surface of soda-lime after the CHF<sub>3</sub> and O<sub>2</sub> plasma etching processes, which may indicate that the Mg<sup>2+</sup> may have also affected the covering of the soda-lime surface making very difficult the fabrication of high aspect ratio nanostructures. This result suggests that in addition to high boiling point and high lattice energy, ionic size larger than the one of Mg<sup>2+</sup> is required to fabricate high aspect ratio nanostructures.

In particular, the very broadband transmittance enhancement obtained on CMG was extended up to 2.4  $\mu\text{m}$ . Graded refractive indexes achieve significant antireflection effect when the height of the nanostructures is 40% or higher compared to the wavelength [30, 31].

From the transmittance enhancement in CMG and the 40% rule, it is possible to infer that the thickness of the nanostructured surface on CMG is about 1  $\mu\text{m}$ . This thickness is more than twice the thickness obtained after treating B270 glass during 40 min with  $\text{CHF}_3$  plasma etching as shown in Fig. 3.29. Figure 3.29 also showed that the sum of the pillar height and the etching depth at 40 min  $\text{CHF}_3$  plasma etching is close to 1  $\mu\text{m}$ . Very low etching depth and higher etching ratio in CMG could explain such high thickness after 40 min  $\text{CHF}_3$  plasma etching. Figure 3.24 showed that in B270 after 80 min of sustained  $\text{CHF}_3$  plasma etching, the (Ca, F) self-generated created an etch-stop layer. If the generation of an etch-stop layer happened much faster in the case of (Ce, F), the thick graded layer could be explained. This hypothesis is plausible considering that  $\text{CeF}_3$  has the highest lattice energy among the self-generated masks and that  $\text{Ce}^{3+}$  ionic radius is larger than the  $\text{Ca}^{2+}$  ionic radius. Finally, other details of the space cover glasses compositions and the (Ba, F) self-generated mask may have also played a key role on the transmittance enhancement, but absence of composition details, especially regarding BaO, on each glass impedes further analysis.

### 3.5. Optical properties simulations using FDTD and RCWA

FullWAVE and DiffractMOD, and CAD are part of the Rsoft simulation package. The 3D structures were designed using the CAD interface; the Finite-difference time-domain (FDTD) simulations were performed using FullWAVE and the (Rigorous Coupled Wave Analysis) RCWA simulations using DiffractMOD. FullWAVE calculates an electromagnetic field in the structure as a function of time and space in response to a given excitation. FullWAVE is based on the FDTD method and on the Yee's mesh [67]. The Yee mesh is made of Yee cells where the electromagnetic field is calculated. In RCWA the structures are divided into several layers in the vertical direction; then the electromagnetic modes in each layer are calculated and they are analytically solved as they propagate through the layers [22].

#### 3.5.1. FDTD and RCWA shape dependence simulations

Figure 3.58 shows the CAD images of the pillar and tapered 2D simulations structures that were simulated. Their shape, size, and aspect ratio was based on the nanostructures observed on the SEM images shown in section 3.2.6.

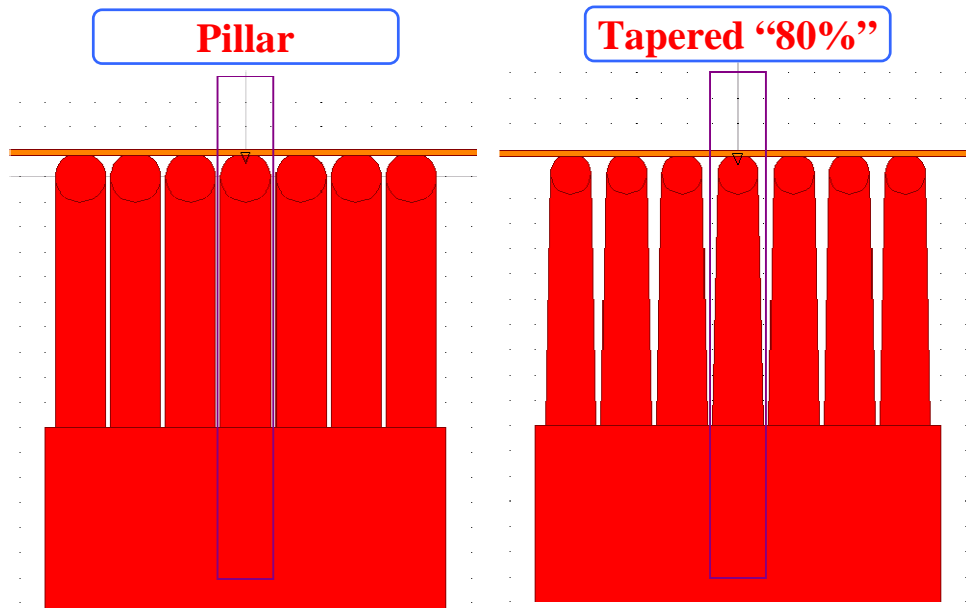


Fig. 3.58. Geometry of the Pillar and Tapered nanostructures simulated using FDTD and RCWA.

In FDTD simulations, a mesh size of  $1 \text{ nm}^2$  was employed. As for RCWA, the structures were discretized in layers of 1 nm and 20 harmonics were used. At first the FDTD and RCWA simulations were compared to compare the accuracy of both simulation methods.

Periodic nanostructures of 100 nm in size, separated by 10 nm and with a height from 100 to 500 nm were simulated. The refractive index available in the B270 MSDS data was employed.

The size of the tips of the tapered structures was 80% the size of the base *i.e.* 80 nm. Finally, in order to further approximate the morphologies observed in the SEM images, the tips of the nanostructures was rounded by placing a circle with the same diameter as the tip size. This circle increased 50 and 40 nm the height of the pillar and tapered nanostructures, respectively.

Very good agreement between the FDTD and RCWA simulation results is shown in Fig. 3.59. Since the FDTD calculations are more time consuming the wavelength step was 10 nm compared to 1 nm in the case of RCWA simulations.

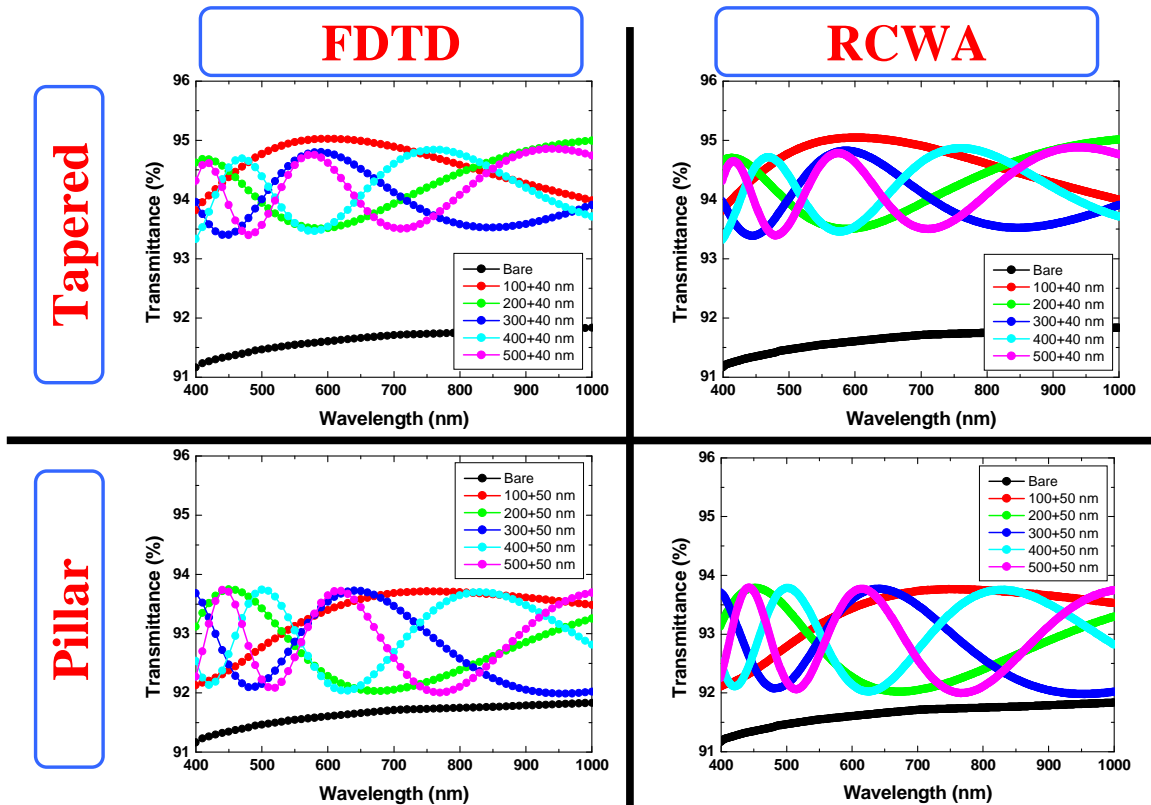


Fig. 3.59. FDTD and RCWA simulation results of Pillar and Tapered nanostructures with height from 100 to 500 nm.

The oscillations observed on the simulated transmittance spectra correspond to interferences originated by intermediate layers with effective refractive indexes and a non-perfect graded refractive index variation [27, 37].

Figure 3.59 shows that there is a significant increase in the transmittance for the tapered shape compared to pillar shape, but this increase is lower than the broadband transmittance enhancement shown in Fig. 3.27. Also, the cross section of the nanostructures that achieved it shown in Fig. 3.28 resembles more to the pillar shape.

### 3.5.2. Graded refractive index simulations

After  $\text{CHF}_3$  plasma etching process, a graded  $\text{SiO}_2$  density in the pillars was shown in Fig. 3.23. In order to emulate such graded density composition, pillar and tapered shapes with graded refractive index were simulated using RCWA as shown in Fig. 3.60. Using 100 layers, the refractive index was varied from 1.2 at the tips up to 1.5 at the bottom of the nanostructures for the whole spectral region.

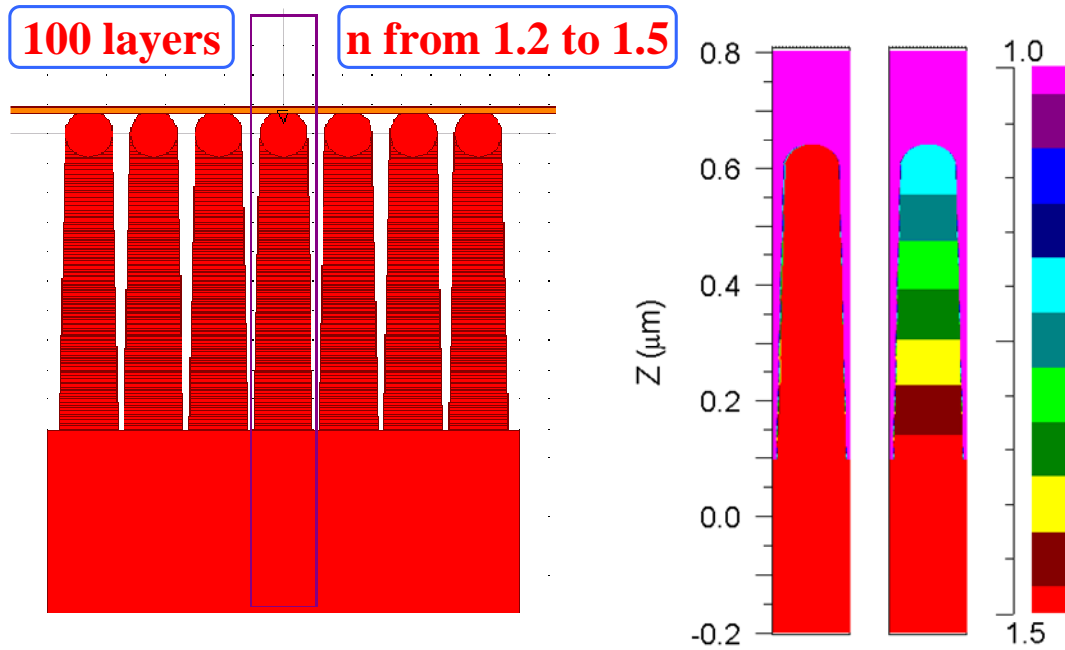


Fig. 3.60. Graded refractive index profile from 1.2 to 1.5 using 100 layers.

Figure 3.61 shows that with graded refractive index composition, even the pillar shape can achieve a similar transmittance enhancement compared to the one observed in Fig. 3.11.



Figure 3.61 also shows that for a graded refractive index composition, the effect of the pillar or tapered shape is much smaller than the shape dependence shown in Fig. 3.59. This simulated result is also in agreement with the similar transmittance enhancement observed for pillar and tapered shapes obtained after 40 min  $\text{CHF}_3$  plasma etching shown in Fig. 3.31. On the pillars with graded refractive index composition, the amplitude of the interferences was reduced owing to a more gradual refractive index compared to the structures with constant refractive index.

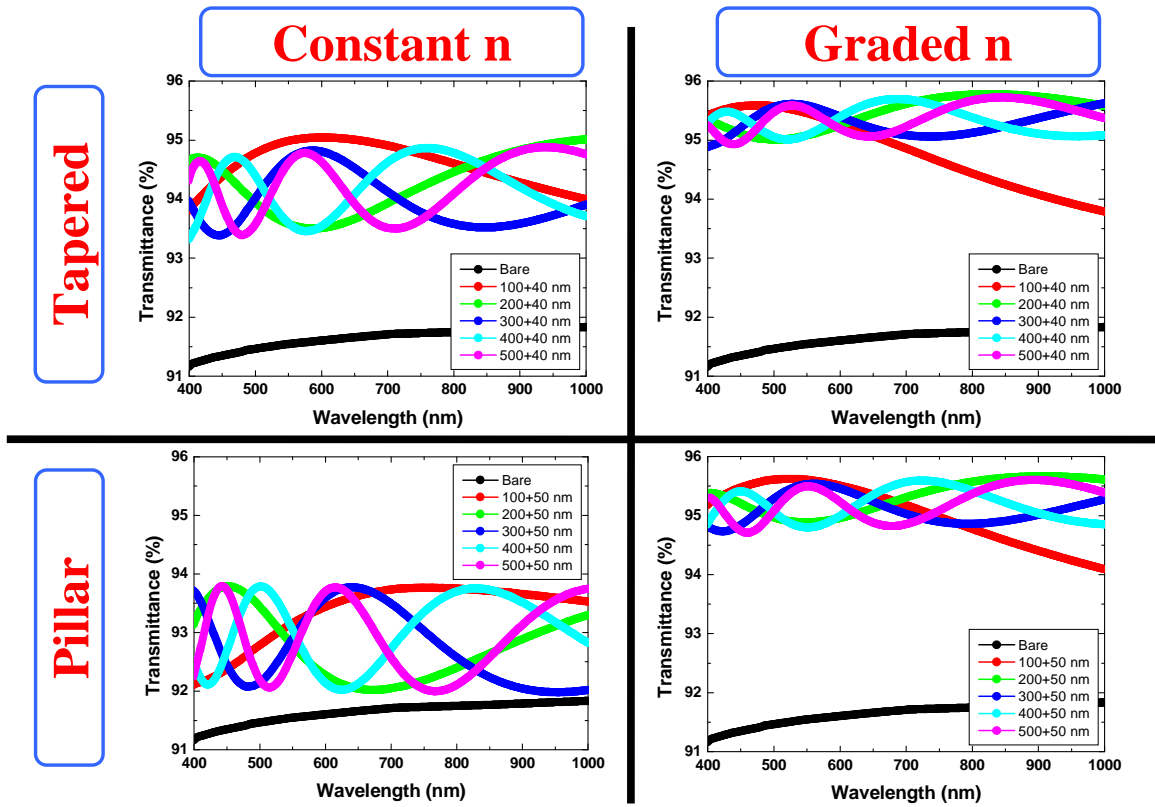


Fig. 3.61. RCWA simulation results of Pillar and Tapered nanostructures with constant and graded refractive index and height from 100 to 500 nm.

### 3.5.3. Comparison between experimental and simulation results

The measured transmittance spectra obtained on structures fabricated after 20 and 40 min  $\text{CHF}_3$  plasma etching was compared to simulations adjusting the height of the tapered shapes to 100 and 450 nm, respectively. Figure 3.62 shows that despite the approximations, somehow comparable results can be obtained. The experimental results do not show interferences owing to the randomness of the fabricated nanostructures. On the bare surface, especially at short wavelengths, there is about 1% difference between the simulated and experimental results. With more accurate refractive index data on B270 and better graded refractive index approximation, improved match between the simulated and experimental results is expected.

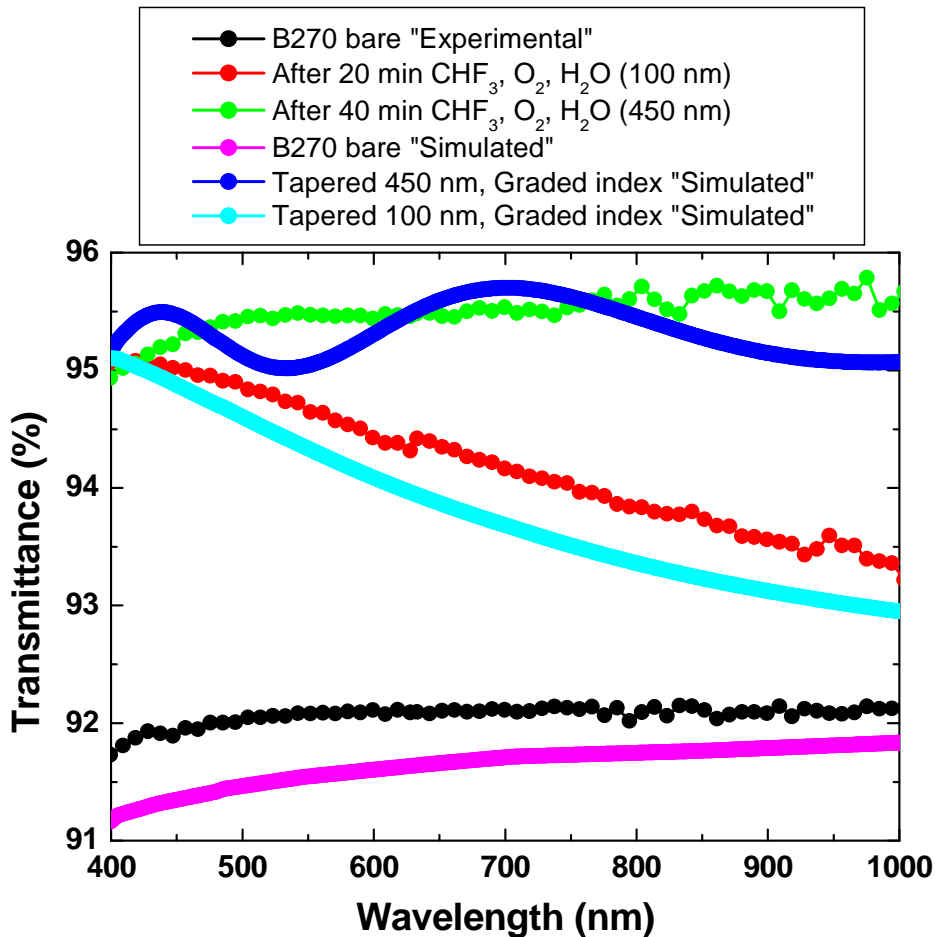


Fig. 3.62. Comparison between experimental and RCWA simulation results of Tapered nanostructures with 100 and 450 nm in height.

### 3.6. Controllable wettability of nanostructured B270 glass surface

The high aspect ratio nanostructures on the surfaces of fused silica and quartz show hydrophilic behavior as-fabricated, but after molecular functionalization by vapor deposition of 1H, 1H, 2H, 2H-Perfluorodecyltrichlorosilane (FDTS) superhydrophobic surface wettability can be achieved as shown in Fig. 3.63 and Fig 3.64, respectively. Superhydrophobic surface can have self-cleaning or anti-fog properties [29, 35].



Fig. 3.63. Top (left) and oblique (right) images of water droplets on nanostructured fused silica with as-fabricated hydrophilic and functionalized hydrophobic wettability properties. Figure is from Ref. [29].

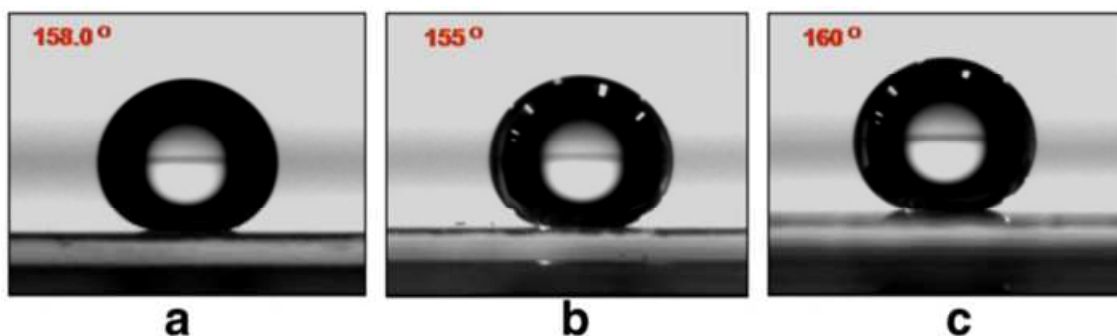


Fig. 3.64. Contact angle measurements of the structured quartz surface. Prepared using (a) on nanostructures on quartz fabricated using PMMA with different thicknesses and plasma etching. Figure is from Ref. [35].

Fused silica and quartz are both examples of pure  $\text{SiO}_2$  materials, which is advantageous when functionalizing with self-assembled molecular monolayers, such as FDTS. In the case of B270, it is not pure  $\text{SiO}_2$  and in particular the composition of the nanostructured surface as fabricated is quite complex as shown in Fig. 3.23, where especially CaF at the tips of the nanostructures was observed.

The deionized water contact angle was comparable on bare B270 glass and on the nanostructured surface obtained after 80 min  $\text{CHF}_3$  plasma etching and 10 min  $\text{O}_2$  plasma etching. (Ca, F) is soluble in  $\text{H}_2\text{SO}_4$ , therefore by carrying out the SPM process; the (Ca, F) can be totally removed, which was confirmed by the XPS spectra shown in Fig. 3.22.

The SPM process in addition to removing (Ca, F), oxidizes the  $\text{SiO}_2$  surface creating hydroxyl endings, which in the case of bare glass, it makes it superhydrophilic as shown in Fig. 3.65. The SPM process turned the nanostructured surface even more hydrophilic than the bare surface, confirming the (Ca, F) removal and oxidization of the  $\text{SiO}_2$  surface of the nanostructures. An additional effect of the SPM process is that the hydroxyl surface is advantageous for the FDTS functionalization. Vapor FDTS deposition was carried out on the bare and nanostructured surfaces under vacuum, at room temperature, and during 16 hours reaching a contact angle of  $106.6^\circ$  and  $144.3^\circ$  on bare and nanostructured surfaces, respectively.

The standard of superhydrophobic contact angle is over  $150^\circ$ . After longer or higher temperature vapor FDTS deposition over  $150^\circ$  deionized water contact angle could be possible on the B270 nanostructured surface.

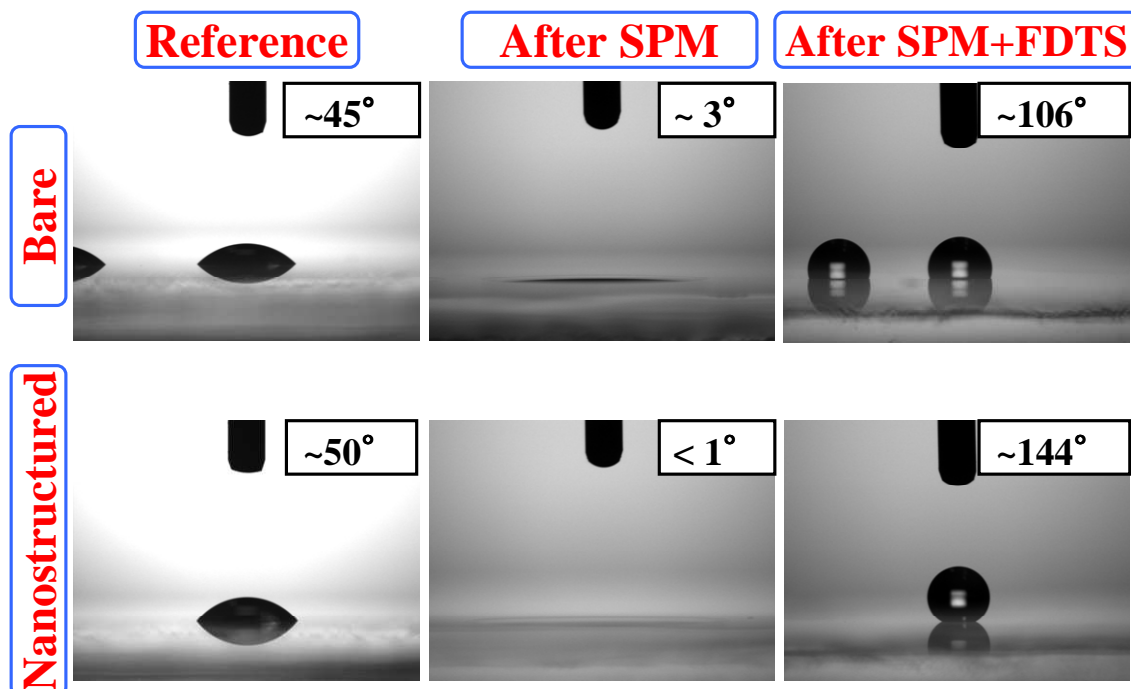


Fig. 3.65. Deionized water contact angle on bare and nanostructured B270 substrates on three conditions: Reference, SPM, and SPM + FDTS.

### 3.7. Previous researches on antireflection methods for flat PMMA surfaces

PMMA is the main material to fabricate Fresnel lenses such as LPI's FK primary [13]. In order to achieve high performance, antireflection at the Fresnel lenses interfaces are also required. To reduce the reflectance on PMMA surface, several techniques have been developed such as co-polymer [68], sol-gel [69] and plasma etching [19-21]. Fresnel lenses have large size; for this reason a scalable and low-cost fabrication technique such as plasma etching was selected to apply antireflection structures on the front and back side of Fresnel lenses.

In addition, scattering by these structures should be minimized to avoid reducing the optical efficiency of the system and the antireflection effect should be broadband because the multi junction solar cells placed below the homogenizers absorb most of the solar spectrum *e.g.* from 300 to 1900 nm in the case of GaInP (1.88 eV) / GaInAs (1.41 eV) / Ge (0.67 eV) triple junction solar cell.

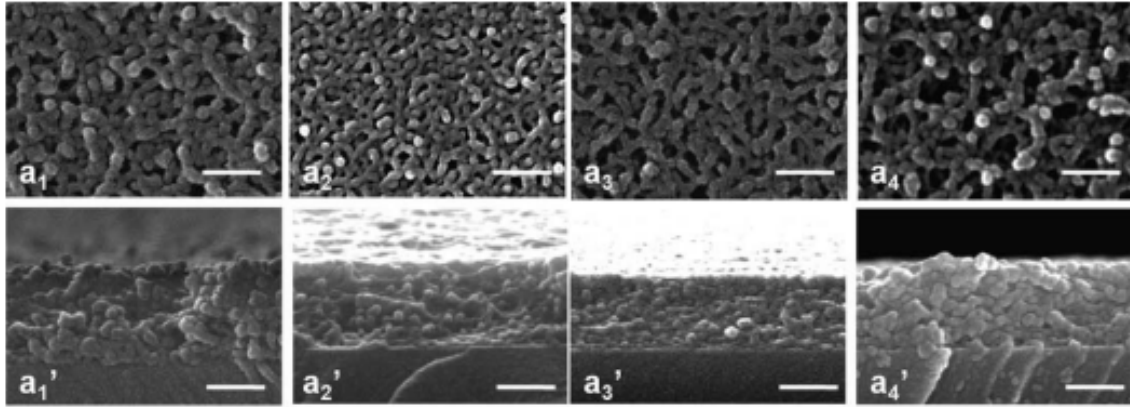


Fig. 3.66. SEM top and cross-section images of porous films achieved by copolymer films and removal of the PMMA domains having different weight percentages and achieving different effective refractive indexes. White bar represents 200 nm and figure is from Ref. [68].

Figure 3.66 shows the porous structure with and effective refractive index that can be obtained by co-polymer process and Fig. 3.67 shows the transmittance enhancements than can be obtained by employing thin sputtered or sol gel antireflection layers.

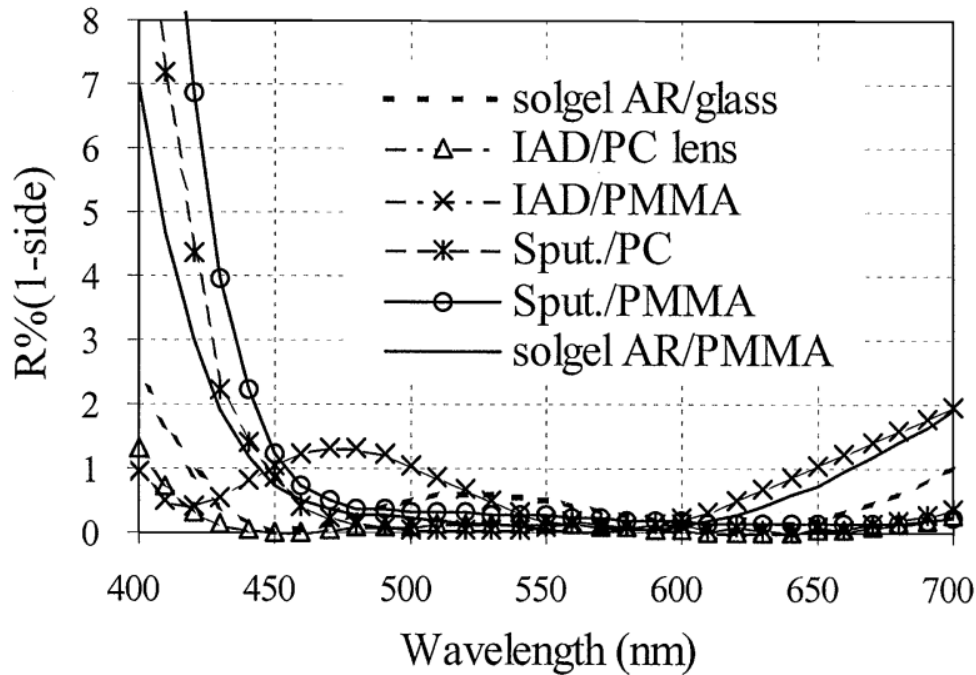


Fig. 3.67. Reflectance spectra of one-side antireflection treatment polycarbonate and PMMA using solgel, ion-assisted deposition, and sputtering. Figure is from Ref. [69].

### 3.8. Maskless and $\text{TiO}_2$ -assisted plasma etching on PMMA substrates

PMMA substrates and Fresnel lenses were textured by using a self-organized etching process (structure S1) [20] as well as a two-step process, whereas a self-organized etching mask is deposit before the etching process (structure S2) [19]. The pre-coating and etching process was carried out in an APS 904 vacuum evaporation plant from Leybold Optics, equipped with the Advanced Plasma Source. Argon and oxygen were used as plasma gases. A thin film of  $\text{TiO}_2$  was deposit as masking material for S2. Depending on the fabrication process, two types of antireflection structures were generated and applied on one-side and both-sides of PMMA substrates and Fresnel lenses. Typical SEM images of the achieved surfaces are shown in Fig. 3.69. Figure 3.69 also shows the potential transmittance enhancement achievable by of optimizing the fabrication of S1 and S2 nanostructures on PMMA.

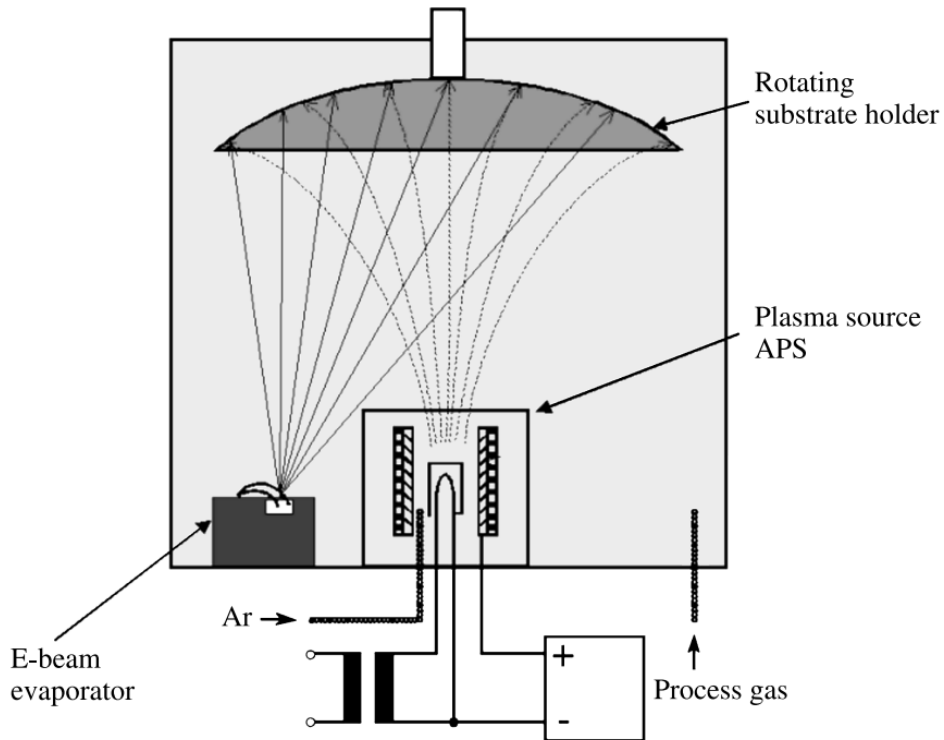


Fig. 3.68. Schema of the equipment used at Fraunhofer IOF to fabricate antireflection nanostructured surfaces on PMMA by maskless and TiO<sub>2</sub> assisted plasma etching processes. Figure is from Ref. [21].

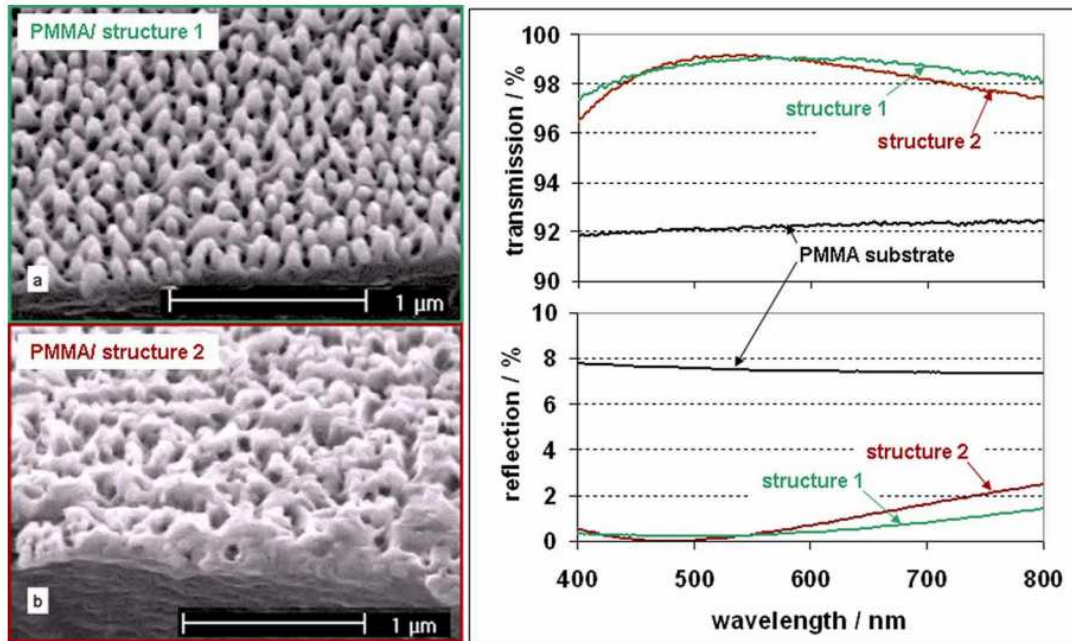


Fig. 3.69. SEM images of structure 1 and structure 2 on PMMA surface (left) and their transmittance and reflectance spectra (right). Figure is from Ref. [19].

## Optical properties

The transmittance spectra of bare and textured PMMA substrates were measured in the 400-1650 nm spectral region as shown in Fig. 3.70. For the substrates with only one side textured, the transmittance was improved by about 2-3% for S1 and up to more than 3% for S2. Both antireflection structures were applied on flat PMMA substrates and Fresnel lenses at the same time in order to analyze the effect in both, the flat and the textured sides of the Fresnel lenses. For reference they were noted front-side (side1), back-side (side2), and both-sides.

Both structures increased the transmittance in the measured spectral region but they show different wavelength dependence. The transmittance peaks of S1 are at lower wavelengths than those of S2. This peak shift is related to the geometry and size of the nanostructures, particularly observed in sample S2-side1, in which the red-shift was largest and blue light scattering was observed. Multiplying the increase of the transmittance for one-side samples using S1 and S2 was in good agreement with the measurement of the samples having both sides textured. Therefore, the processing of the second side does not affect the textures of the first one.

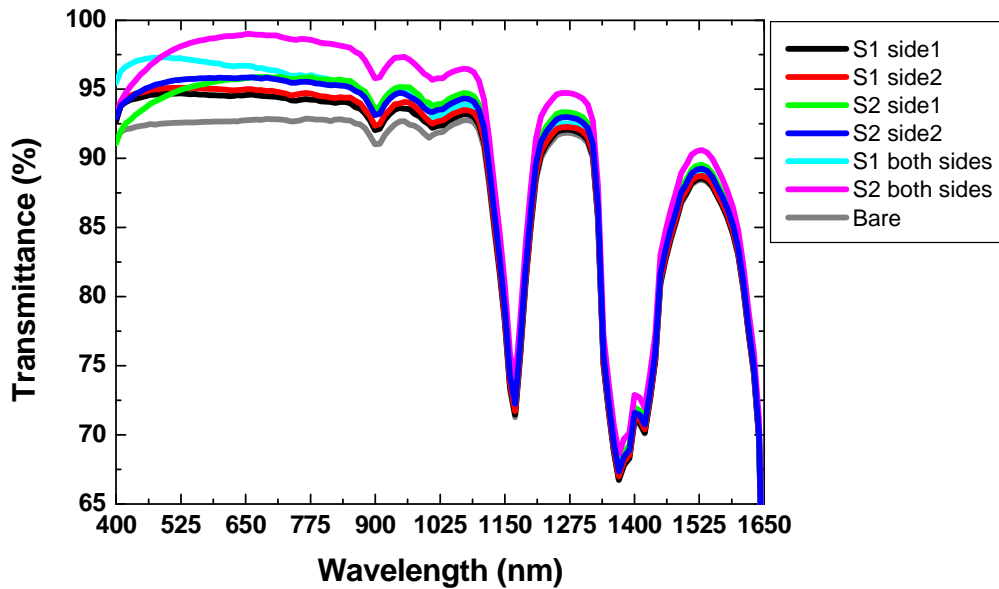


Fig. 3.70. Transmittance spectra of bare and on PMMA substrates treated with S1 or S2 on one or both sides.



Figure 3.69 and Fig. 3.70 show that the transmittance enhancement obtained in the tested samples using S1 is considerably lower than the optimized condition. As for S2, it is close to the optimized condition except that at short wavelengths the transmittance is slightly lower. For better visualization of the transmittance enhancement, Fig. 3.71 shows the transmittance ratio between the bare PMMA and each of the textured samples.

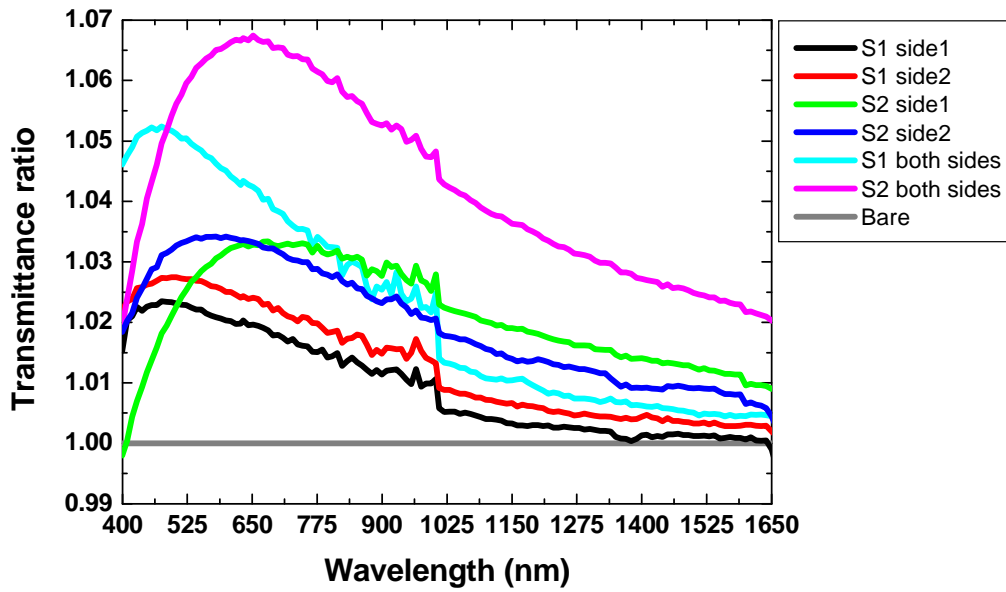


Fig. 3.71. Transmittance ratio of bare and on PMMA substrates treated with S1 or S2 on one or both sides.



# **Chapter 4**

## **4. Nanostructuring surfaces of the POE and SOE**

## 4.1. Texturing the flat and corrugated surfaces of LPI's PMMA POE

The nanostructures on PMMA substrates were also applied on the front and back sides of the latest generation Fresnel lenses [13]. Transmittance improvement was measured on the textured Fresnel lenses. Finally, field tests were carried out and enhancements of  $J_{sc}$  and efficiency were demonstrated.

### 4.1.1. Optical properties

LPI's FK primary Fresnel lenses were used to evaluate the effect of the antireflection structures on PMMA. LPI's FK primary is a Fresnel lens with four-fold symmetry [13]. Each of the four sections measures  $80 \times 80 \text{ mm}^2$ . A collimated beam of 5 mm in diameter was used to scan one line from the center of the concentric textures of one of the four sections to the edge, by steps of 2.5 mm. Therefore, the scanned area was  $5 \times 80 \text{ mm}^2$  as shown in Fig. 4.1. The light was collected in an integrating sphere placed at the focal point of the Fresnel lenses.

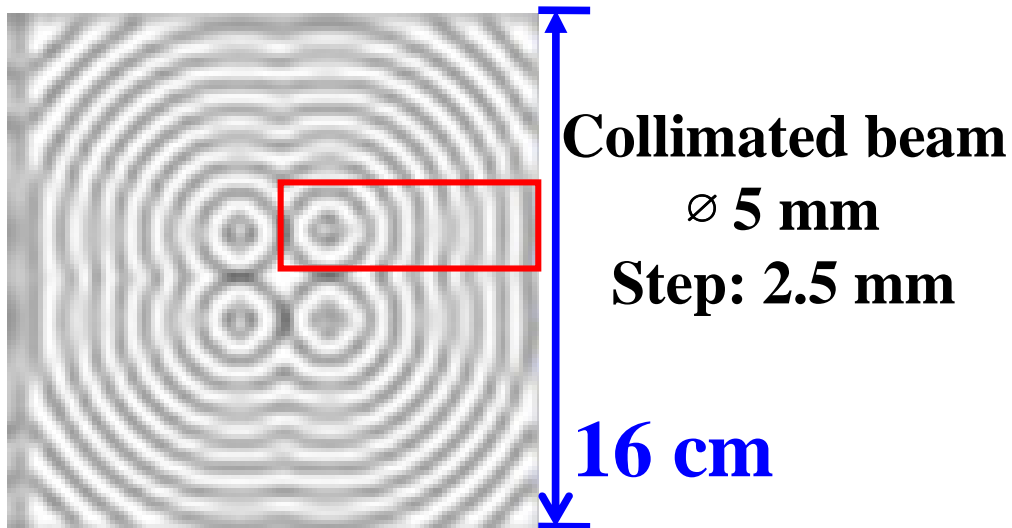


Fig. 4.1. Schema of the Fresnel lenses characterization in which a 5 mm collimated beam scanned a rectangular section on one of the 4-fold parts.

Figure 4.2 shows the transmittance spectra of the scanned areas for bare and textured Fresnel lenses. The transmittance spectra on the Fresnel lenses appears to be position dependent. Especially there is a dip between 20-30 mm and two peaks around 10 and 40 mm. In addition there is a decrease in the transmittance of short wavelengths compared to the flat substrates, which might correspond to scattering by the concentric structures of the Fresnel lenses.

As shown in Fig. 4.2, there is an overall increase in the transmittance reaching up to 99%. In most of the evaluated area the transmittance enhancement by applying S2 on both sides of the Fresnel lens followed a similar trend as the one shown in Fig. 3.71, reaching transmittance enhancements larger than 6%.

**Scanned area: 5 x 80 mm<sup>2</sup>, Collimated beam  $\varnothing$  5 mm, Step: 2.5 mm**

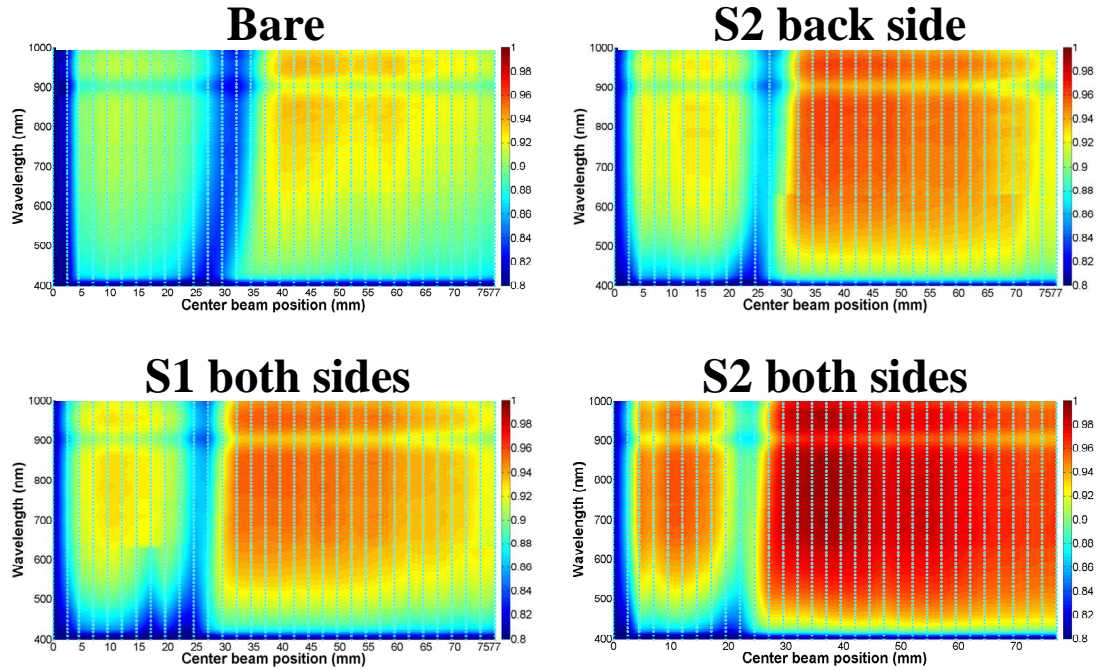


Fig. 4.2. Transmittance spectra of a 5 x 80 mm<sup>2</sup> section of bare Fresnel lens and the ones having structure S1 on one side, and S2 on one and both sides.

#### 4.1.2. Field tests

Field tests were carried out in Madrid at LPI-CeDint facilities. The same secondary optical element and Spectrolab C3MJ Concentrator Cell Assembly (CCA) were used to characterize the bare and each of the textured Fresnel lenses as shown in Fig. 4.3. The Current-Voltage curve was measured for each sample and the efficiencies were calculated.

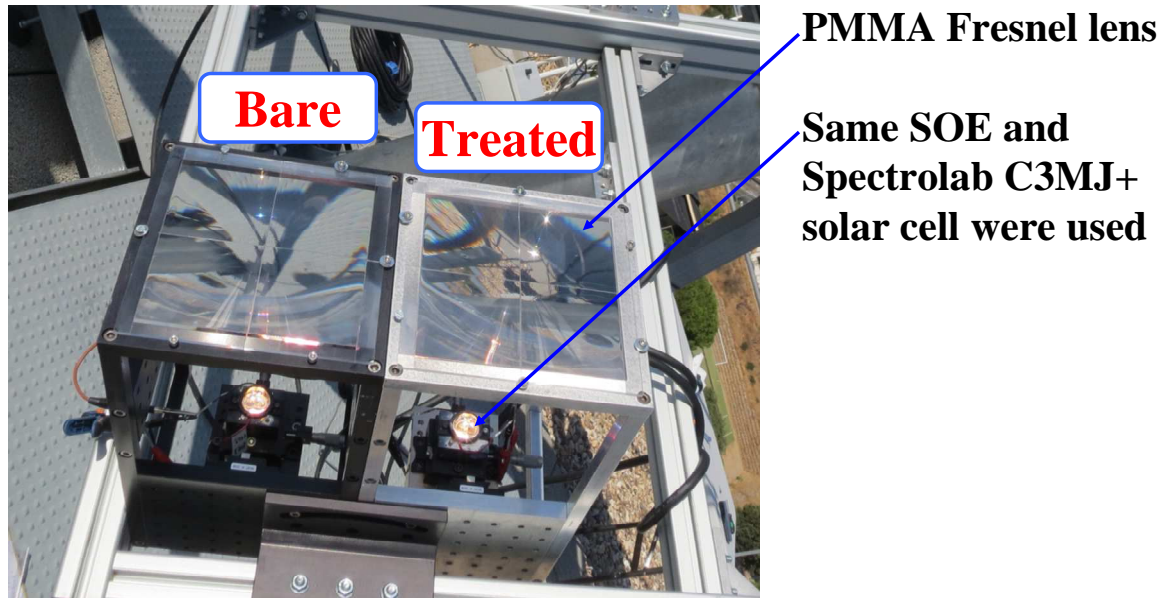


Fig. 4.3. Image of LPI's Ventana CPV system depicting the characterization of S1 and S2 nanostructuring methods applied on one and both sides of the PMMA Fresnel lenses.

Figure 4.4 shows the Current-Voltage curves obtained for the bare Fresnel lens and the one having S2 on both sides. Figure 4.4 shows a 6.56%  $J_{sc}$  relative gain by using S2 on both sides compared to the bare one,  $V_{oc}$  remained unchanged and there was a decrease in the Fill Factor (FF). These characteristics resulted in a 3.82% efficiency relative gain.  $J_{sc}$  was normalized at DNI 900 W/m<sup>2</sup> and the efficiency at 25°C.

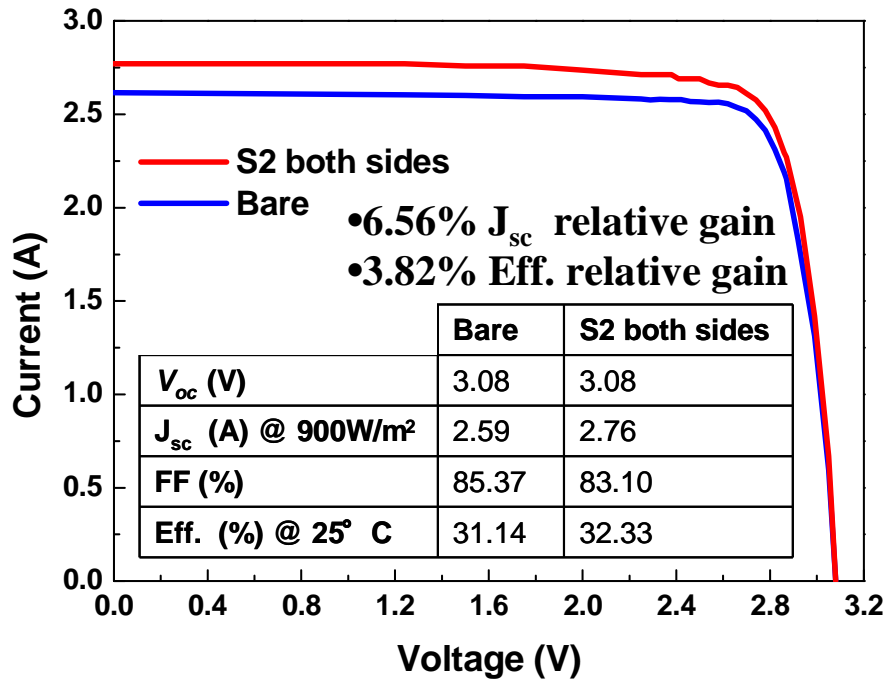


Fig. 4.4. Field tests Current-Voltage curves obtained using a bare Fresnel lens (blue), and the one having S2 on both sides (red).

Figure 4.5 summarizes the  $J_{sc}$  and efficiency relative gains obtained using each of the Fresnel lenses having S1 or S2 on the front side, back side, or both sides. In almost all the cases, the  $J_{sc}$  relative gains were larger than the efficiency ones. This resulted from the lower FF obtained using the treated samples. Further evaluation of the FF degradation is presented in section 4.5.

Figure 4.5 shows that the front side texturing had a larger improvement than the back side. Figure 3.71 showed the various transmittance enhancements on the tested one side PMMA substrates. Also, the effect of the tilted surfaces may have affected the optimum fabrication of the nanostructures compared to the flat surface. In all conditions a better improvement was obtained using S2 and the largest relative gains were obtained when applying S2 on both sides. In our tests, S2 appeared better than S1 in agreement with the transmittance spectra measured on the treated PMMA substrates as shown in Fig. 3.71. The performance of S1 and S2 could be optimized with further tests as shown in Fig. 3.69.

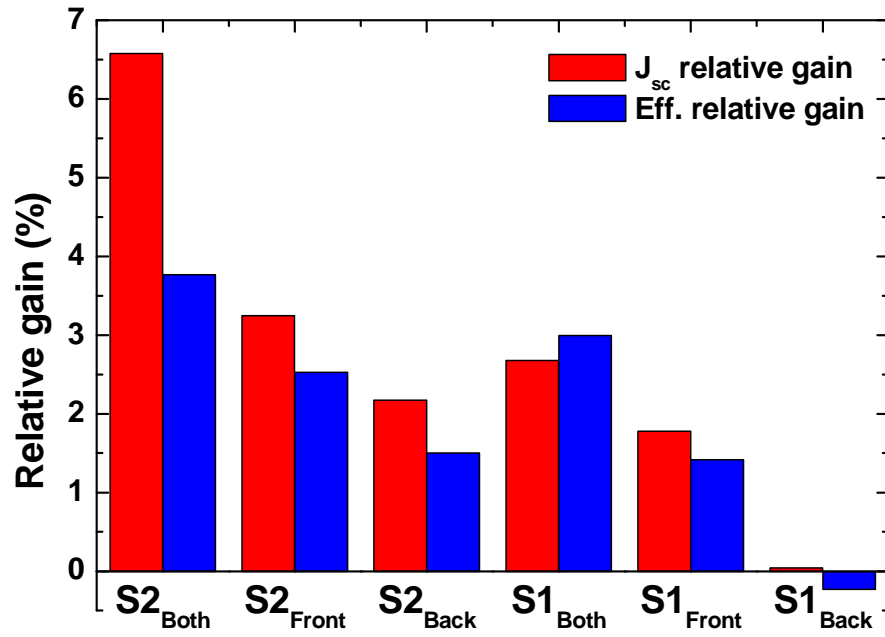


Fig. 4.5.  $J_{sc}$  and efficiency relative gains obtained on Fresnel lenses with S1 and S2 on one or both sides.



## 4.2. Texturing the curved surface of LPI's glass SOE

### 4.2.1. LPI's curved secondary optical element

LPI's secondary optical element (SOE) is made of LIBA 2000 glass and it has a curved surface. At the bottom of the SOE, there is a cavity that is filled with PDMS where the Spectrolab C3MJ CCA is bonded as shown in Fig. 4.6. In order to reduce the reflectance at the Air/SOE interface and enhance the CPV module efficiency, the  $\text{CHF}_3$  maskless plasma etching surface nanostructuration process was applied directly on the SOE inside the Anelva DEA 507L RIE chamber. Since the process was successfully applied on the surface of LIBA 2000 substrates, there was potential applicability on the curved surface and thicker sample.

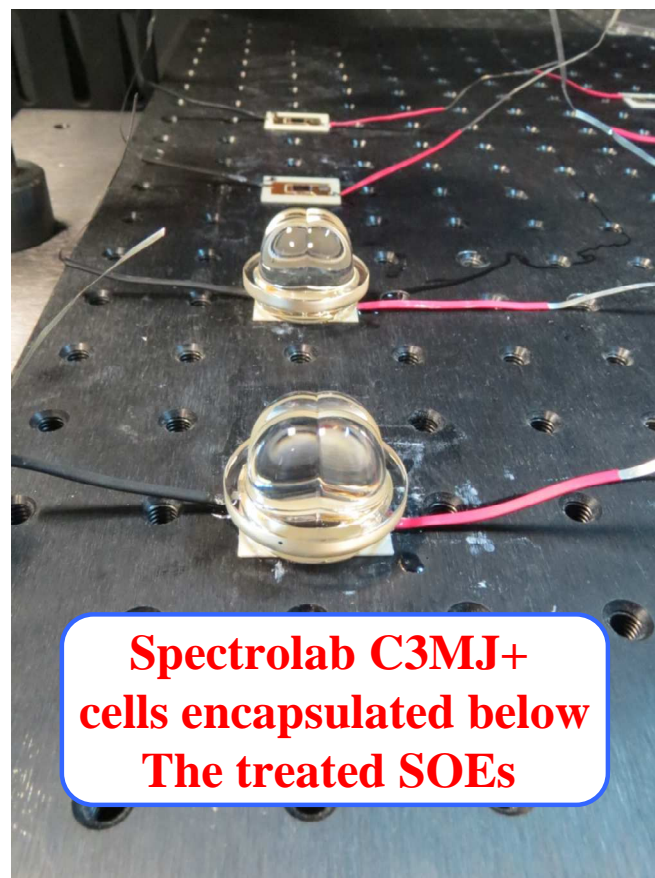


Fig. 4.6. Image of the textured SOEs with Spectrolab C3MJ+ solar cells encapsulated below them before field tests.

#### 4.2.2. Field tests

The same primary optical element was used to characterize the bare and each of the textured SOEs as shown in Fig. 4.7. The Current-Voltage curve was measured for each sample and the efficiencies were calculated.

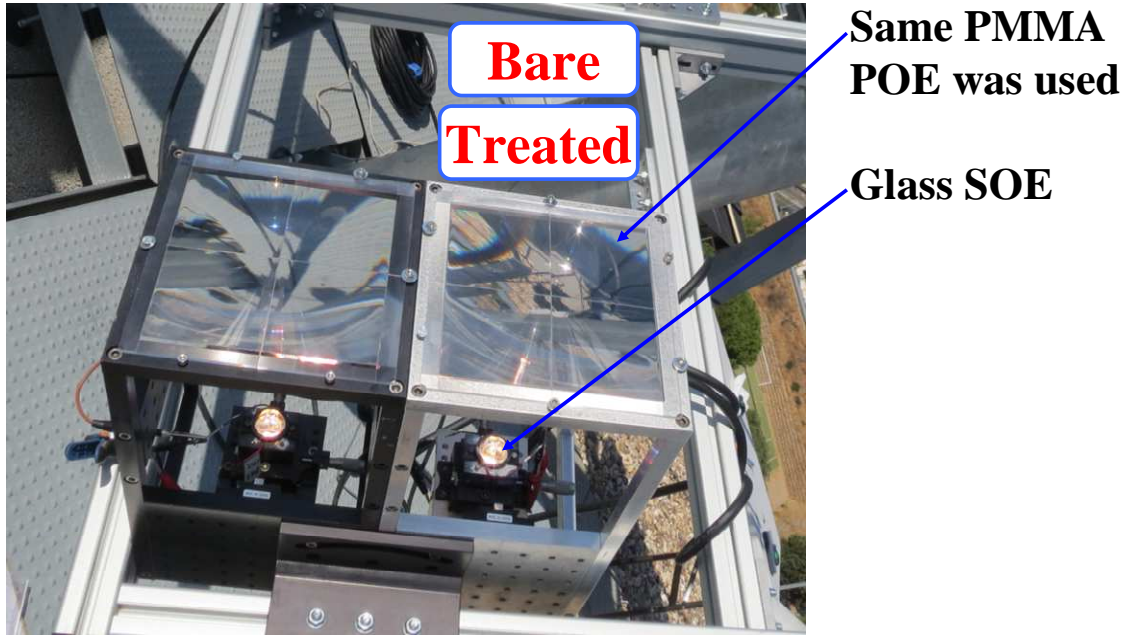


Fig. 4.7. Image of LPI's Ventana CPV system depicting the characterization of the nanostructuring process on the SOEs.

Figure 4.8 summarizes the  $J_{sc}$  and efficiency relative gains obtained using two different SOEs at different RF power. SOE1 was treated using the maximum RF power, whereas SOE2 was treated using the typical 800 W RF power. Both SOEs were measured twice at different times on the same date. Figure 4.8 shows that SOE2 achieved maximum 3.78% and 2.75%  $J_{sc}$  and efficiency relative gains, respectively.

The remarkable 3.78% maximum  $J_{sc}$  relative gain confirms the successful fabrication of nanostructures on the curved surface of LPI's SOE and can be understood by the broadband transmittance enhancement observed on B270 and LIBA 2000 glasses. The  $J_{sc}$  and efficiency relative gains were larger on SOE2 than in SOE1 and in all the cases, the  $J_{sc}$  relative gains were larger than the efficiency ones. This larger  $J_{sc}$  gains resulted from the lower FF obtained on the treated samples. Further evaluation of the FF degradation is presented in section 4.5.

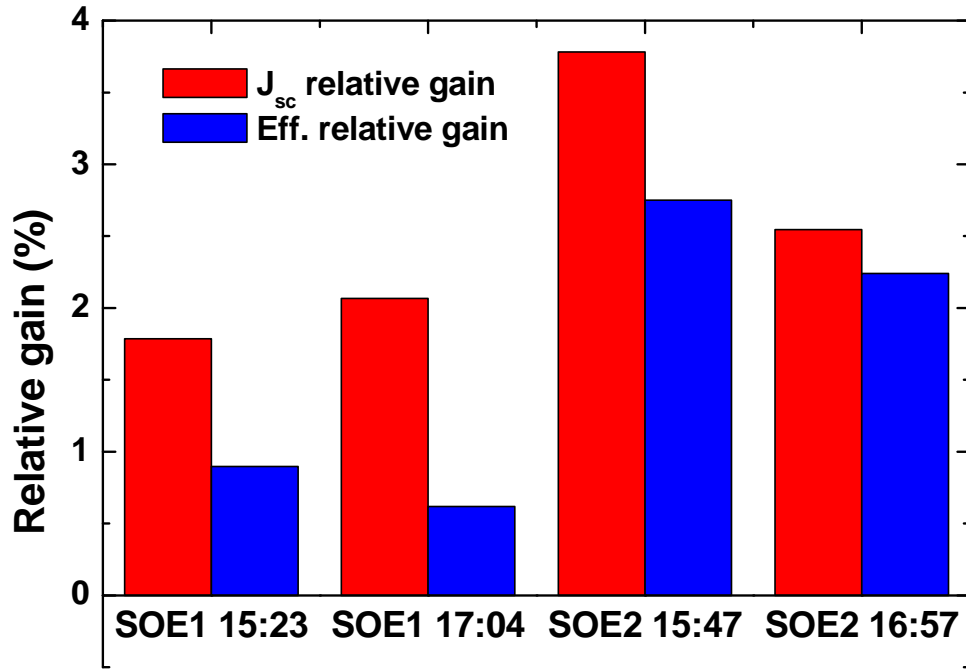


Fig. 4.8.  $J_{sc}$  and efficiency relative gains measured at two different times on SOEs treated during 80 min with  $\text{CHF}_3$  plasma etching using RF power 1000W (SOE1) and 800W (SOE2).

### 4.3. CPV module with all textured interfaces

#### 4.3.1. Field tests

An all textured interfaces CPV module was assembled using the Fresnel lens with S2 on both sides and the best treated homogenizer and its performance was compared to an all bare interfaces CPV module. In Madrid, on October 7<sup>th</sup> 2013, the Current-Voltage curve was measured from 11:38 to 12:45 every 5-10 min both modules and the  $J_{sc}$  and efficiency relative gains were calculated as shown in Fig. 4.9. The 10 measurements averaged  $J_{sc}$  and efficiency relative gains obtained on the all textured interfaces CPV module were 7.47% and 4.58%, respectively. The maximum  $J_{sc}$  and efficiency relative gains were 7.99% and 5.06%, respectively. The FF was also degraded on the all textured interfaces module as it happened for the textured individual optical elements, but still reproducible module relative efficiency enhancement of about 5% was achieved. Further evaluation of the FF degradation is presented in section 4.5.

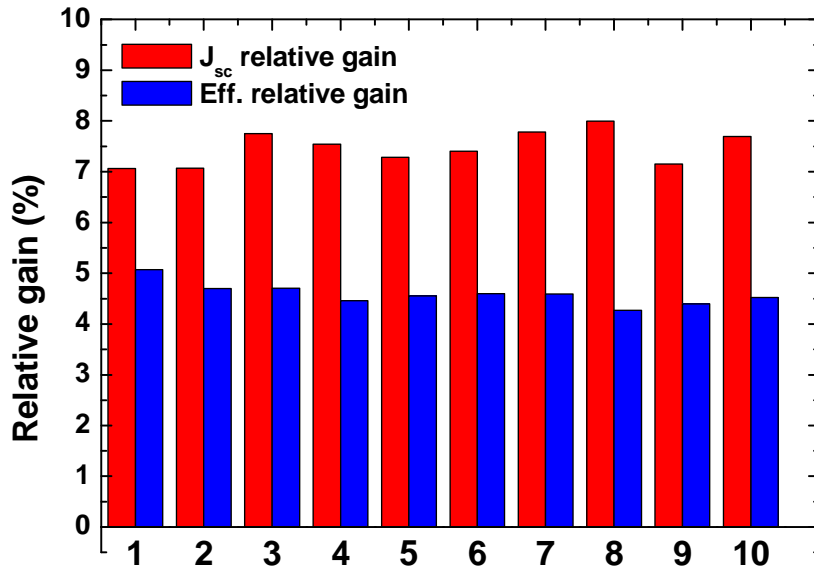


Fig. 4.9.  $J_{sc}$  and efficiency relative gains measured every 5-10 min from 11:38 to 12:45 on October 7<sup>th</sup> in Madrid, Spain using Fresnel lens with S2 on both sides and SOE2.

## 4.4. Hydrophobic coating

### 4.4.1. PMMA substrates

As an alternative solution to solve the dew accumulation on the back-side of the POE that occurs in CPV systems after rainy days [24, 25], the applicability of a hydrophobic coating was studied. As part of the collaboration with the Fraunhofer IOF, a hydrophobic coating was applied on the back-side of a Fresnel lens after fabricating S2 on the same back-side *i.e.* the hydrophobic coating was applied after the surface nanostructuration increasing the deionized water contact angle as shown in Fig. 4.10. In this manner both effects, antireflection and less dew condensation, could be achieved.

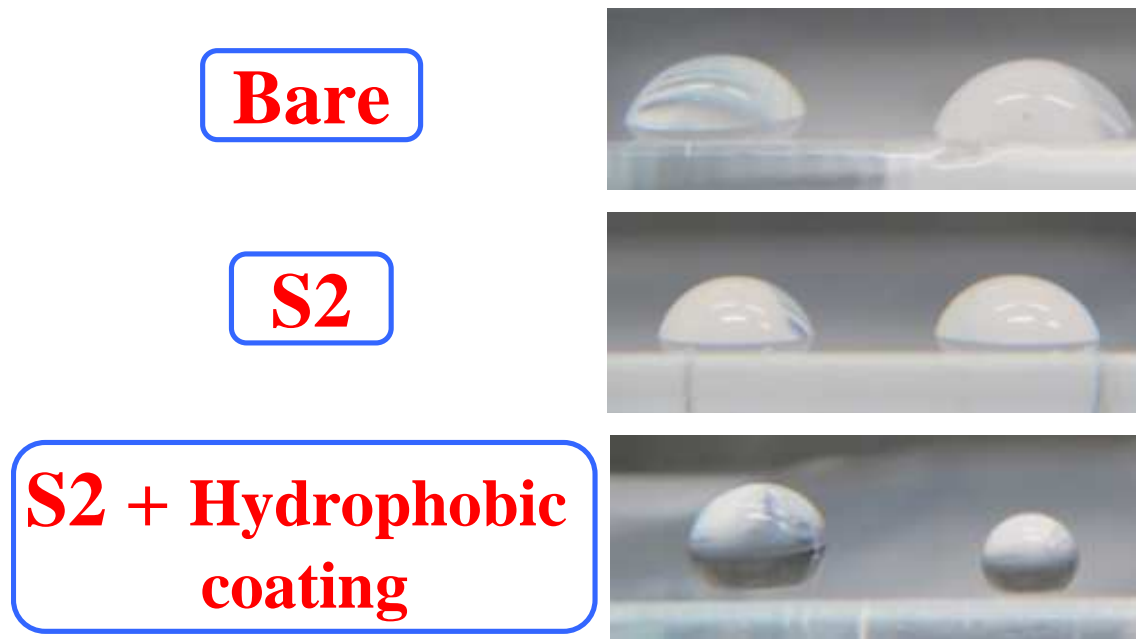


Fig. 4.10. Oblique images of water droplets on bare (top), S2 (middle), and hydrophobic functionalized S2 (bottom) PMMA surfaces.

### Optical properties on PMMA substrates

The transmittance spectra of bare, S2, and S2 + hydrophobic coating PMMA substrates were measured in the 400-1650 nm spectral region as shown in Fig. 4.11. For better visualization of the transmittance enhancement, Fig. 4.12 shows the transmittance ratio between the bare PMMA and both treated PMMA substrates.

Figure 4.12 also shows that S2 was successfully fabricated on both PMMA substrates, but the hydrophobic coating caused a slight decrease of the transmittance at short wavelengths, which could be the result of hydrophobic coating absorption or modification of the effective refractive index of the nanostructured surface. To clarify the origin of this transmittance decrease more detailed evaluation is needed.

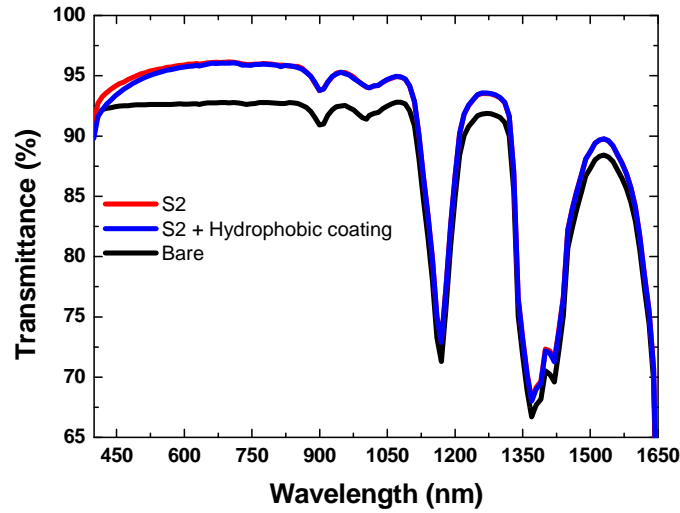


Fig. 4.11. Transmittance spectra on bare, S2, and hydrophobic functionalized S2 on PMMA substrates.

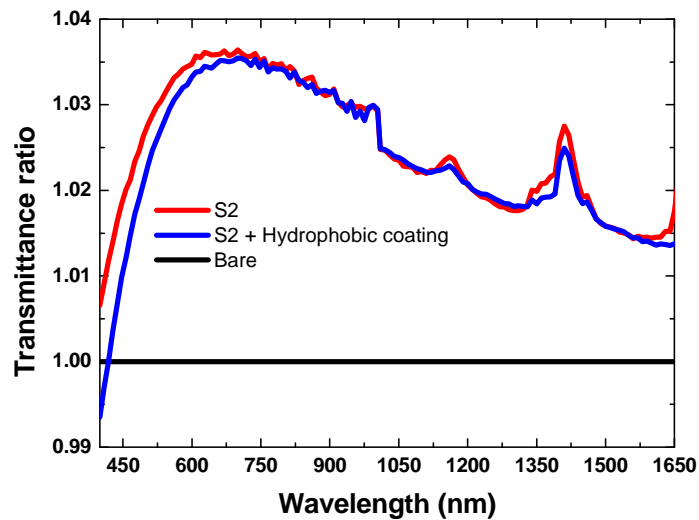


Fig. 4.12. Transmittance ratio of bare, S2, and hydrophobic functionalized S2 on PMMA substrates.

#### 4.4.2. Primary optical element of UT CPV system

##### Optical properties on Fresnel lenses

To evaluate the applicability of a hydrophobic coating a Fresnel lens of 10 x 10 cm<sup>2</sup> was employed. A collimated beam of 10 mm in diameter was used to scan one line from the center of the Fresnel lens to the edge, by steps of 5 mm. Therefore, the scanned area was 10 x 50 mm<sup>2</sup>. Figure 4.13 shows the transmittance spectra of the scanned areas for bare and treated Fresnel lenses, which shows transmittance enhancement for both treated Fresnel lenses and a decrease of the transmittance at short wavelengths on when applying the hydrophobic coating, as observed in the treated PMMA substrates.

**Scanned area: 10 x 50 mm<sup>2</sup>,  
Collimated beam  $\varnothing$  10 mm, Step: 5 mm**

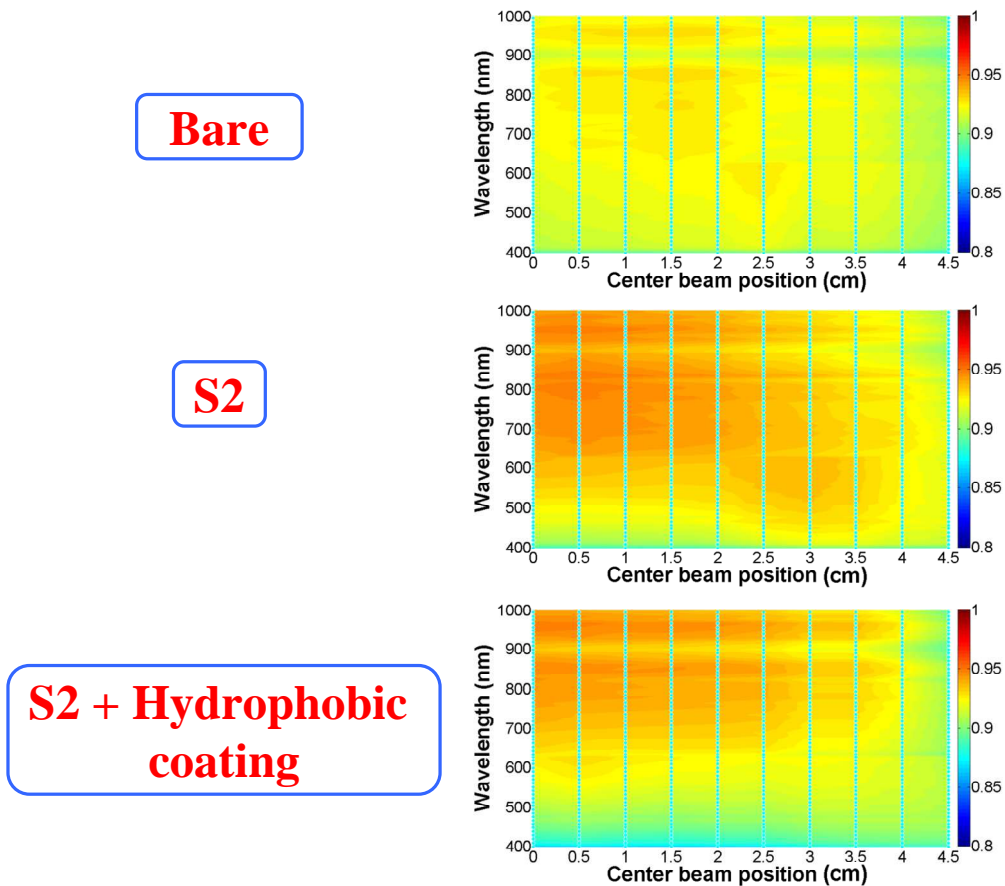


Fig. 4.13. Transmittance spectra of a 10 x 50 mm<sup>2</sup> section of bare (top) Fresnel lens and the ones having S2 (middle), and hydrophobic functionalized S2 (bottom) on the back-side.



## Field tests

To evaluate the applicability of a hydrophobic coating, field tests were carried out at the University of Tokyo employing the in-house UT-CPV system and dual-axis tracker shown in Fig. 4.14. The same homogenizer and lattice matched LM3JC InGaP / (In)GaAs / Ge solar cell was used. UT-CPV system employs a homogenizer made of PMMA in the truncated inverted pyramid configuration [12]. The Current-Voltage curve was measured for each sample, by exchanging the Fresnel lenses and the performance was evaluated as shown in Fig. 4.15.

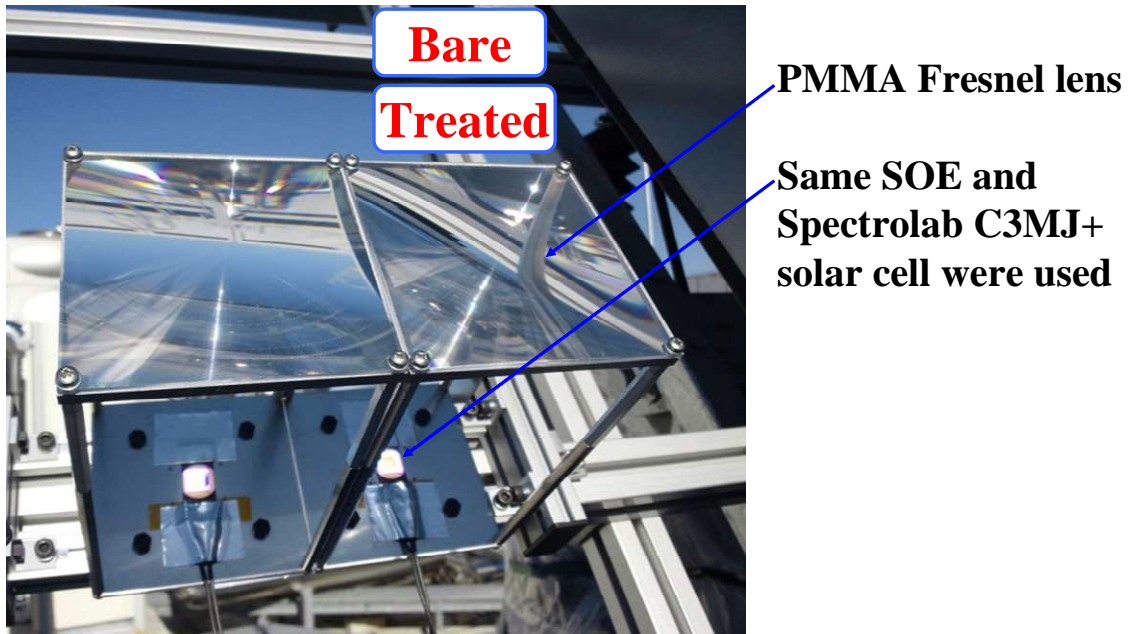


Fig. 4.14. Image of UTCPV system depicting the characterization of S2 and hydrophobic functionalized S2 back side of PMMA Fresnel lenses.

Figure 4.15 shows the Current-Voltage curves obtained for the bare Fresnel lens, the Fresnel lens with S2 on the back side, and the Fresnel lens with S2 + hydrophobic coating on the back side. Figure 4.15 shows a 2.87%  $J_{sc}$  relative gain by using S2 on the back side. This enhancement is similar, but slightly larger than the  $J_{sc}$  relative gain obtained by applying S2 on the back side of LPI's POE. Unexpectedly, the  $J_{sc}$  relative gain was much larger on Fresnel lens with S2 + hydrophobic coating on the back side reaching 7.73% as shown in Fig. 4.15. Despite the transmittance decrease at short wavelengths, about 5% additional  $J_{sc}$  relative gain was obtained.



A possible explanation of the additional gain could be a focal distance modification by the hydrophobic coating. In house tests showed that the UT-CPV system is quite sensitive to focal distance variations.

In S2 and S2 + hydrophobic coating Fresnel lenses, the gain in  $J_{sc}$  was also accompanied by a decrease in the FF as observed on the field tests using LPI's Ventana CPV system. The FF when using the bare Fresnel lens was 74.39%, but it decreased to 74.02% and 71.93% for 2 and S2 + hydrophobic coating Fresnel lenses, respectively. Despite the gain in  $J_{sc}$ , the FF decrease caused a decrease of the UT-CPV module efficiency when using the treated Fresnel lenses. The efficiency when using the bare Fresnel lens was 24.66% and it increased to 25.24% and 25.69% for S2 and S2 + hydrophobic coating Fresnel lenses, respectively. In conclusion, the  $V_{oc}$  remained unchanged and the  $J_{sc}$  enhancement was accompanied with a FF decrease, which limited the efficiency enhancement. DNI during measuring time was  $760 \text{ W/m}^2$ . Further evaluation of the FF degradation is presented in section 4.5.

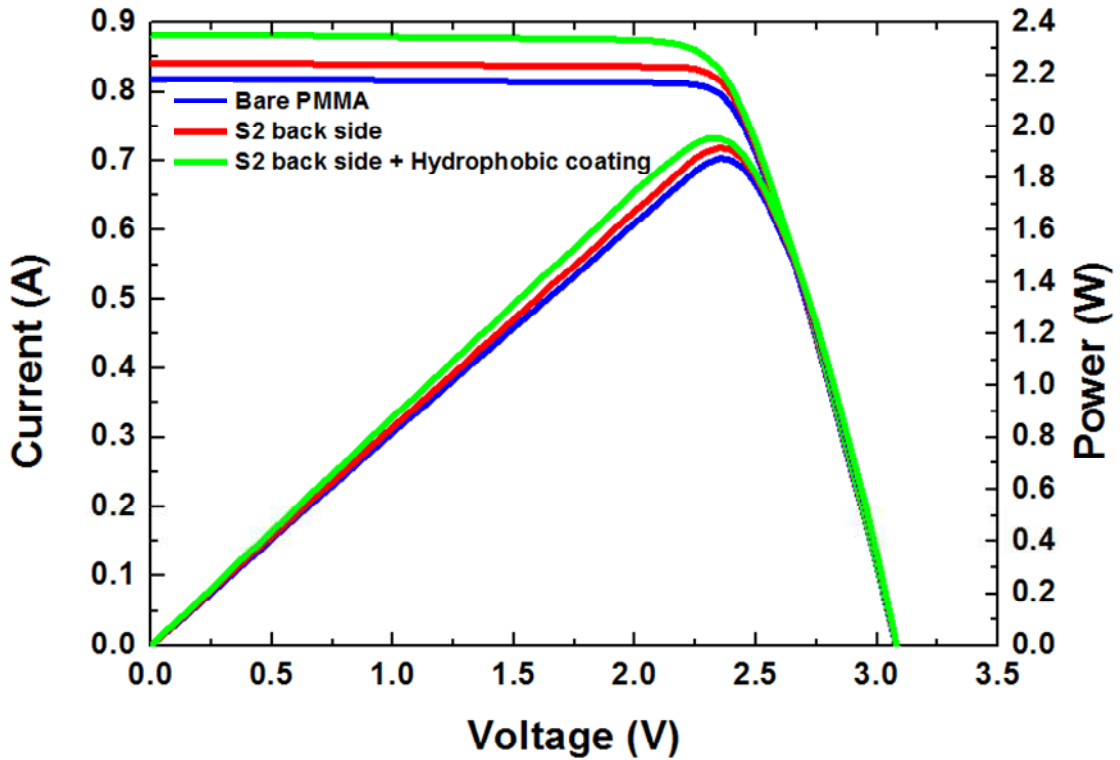


Fig. 4.15. Field tests Current-Voltage curves obtained using a bare Fresnel lens (blue), and the ones having S2 (red), and hydrophobic functionalized S2 (green) on the back-side.

## 4.5. Nanostructured surfaces' effect on the Fill Factor

Nanostructuring the three Air/Optical-elements interfaces in CPV modules and achieving  $J_{sc}$  enhancement was accompanied with a FF decrease. Despite the FF decrease, efficiency enhancement was achieved.

### 4.5.1. EQE measurement of 3JSC below bare and textured substrates

The Current-Voltage curve of the Ge bottom cell has a degraded FF due to shunt resistance in the Ge bottom cell. If below bare or treated PMMA substrates, the bottom cell became current-limiting cell; it could be possible to explain the degraded FF observed in the field tests. To evaluate this hypothesis, the EQE of the three sub-cells was measured without and below bare and all treated PMMA flat substrates as shown in Fig. 4.16. On each condition, from the EQE results, the  $J_{sc}$  of each sub-cell was calculated and compared to determine the current-limiting cell as shown in Table 3 and Table 4.

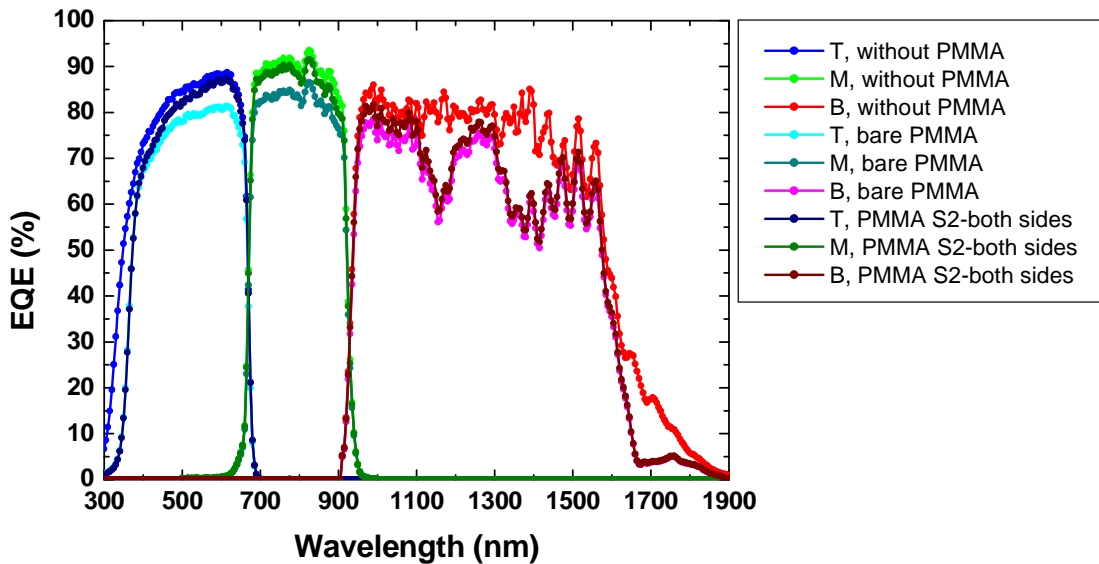


Fig. 4.16. EQE of each sub-cell without PMMA substrate, below bare PMMA substrate, and below PMMA substrate with S2 on both sides.

Figure 4.16 shows the EQE of each sub-cell without PMMA substrate, below bare PMMA substrate, and below the PMMA substrate with S2 on both-sides. Figure 4.16 shows the significant EQE decrease caused by the PMMA substrate refractive index creating around 8% or reduction, but also caused by the PMMA UV absorption and various absorption peaks in the near-IR region. Figure 4.16 also shows that after applying S2 on both-sides of the PMMA substrate the EQE is partially recovered.

Figure 4.17 compares the transmittance and the EQE ratios obtained by dividing the transmittance and EQE obtained using the PMMA substrate with S2 on both-sides by the transmittance and EQE obtained using the bare PMMA substrate. Very similar EQE and transmittance ratios are shown in Fig. 4.17 indicating good agreement between both measurements. Table 3 and Table 4 summarize the calculated  $J_{sc}$  using the measured EQE without and below bare and all treated PMMA flat substrates. Table 3 and Table 4 show the bottom-cell did not become current-limiting cell under any of the bare or treated PMMA substrates. Table 3 and Table 4 also show that without PMMA substrate the middle-cell is the current-limiting cell.

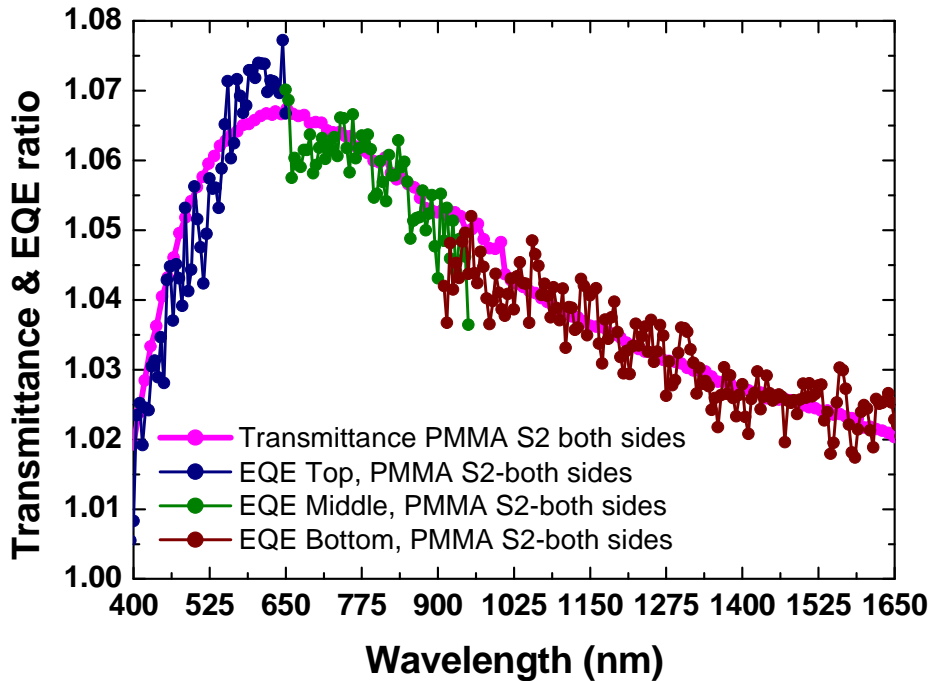


Fig. 4.17. EQE and Transmittance ratio comparison between bare PMMA substrate and PMMA substrate with S2 on both sides.

After placing the PMMA substrate, the top-cell became the current-limiting cell in all cases except when using S1 on both-sides of the PMMA substrate. The middle-cell became current-limiting cell because the PMMA substrate with S1 on both-sides mainly enhances the transmittance around the spectral region of the top-cell as shown in Fig. 3.71. This result suggests that the antireflection effect of S1 and S2 can be tuned to mainly enhance the top-cell or the middle-cell.

	Top-cell $J_{sc}$ (mA/cm <sup>2</sup> )	Middle-cell $J_{sc}$ (mA/cm <sup>2</sup> )	Bottom-cell $J_{sc}$ (mA/cm <sup>2</sup> )
<b>Without PMMA</b>	15.139	<b>15.027</b>	17.238
<b>Bare PMMA</b>	<b>13.745</b>	13.88	14.865
<b>S1 front</b>	<b>13.981</b>	14.035	14.963
<b>S1 back</b>	<b>14.046</b>	14.103	14.99
<b>S1 both</b>	14.162	<b>14.136</b>	15.002
<b>S2 front</b>	<b>14.111</b>	14.333	15.21
<b>S2 back</b>	<b>14.19</b>	14.282	15.126
<b>S2 both</b>	<b>14.5</b>	14.687	15.394

Table 3. Summarized  $J_{sc}$  in mA/cm<sup>2</sup> of each sub-cell without PMMA substrate and placed below bare and textured PMMA substrates. The limiting  $J_{sc}$  is indicated in red.

	Top -cell $J_{sc}$ (mA/cm <sup>2</sup> )	Middle-cell $J_{sc}$ (mA/cm <sup>2</sup> )	Bottom-cell $J_{sc}$ (mA/cm <sup>2</sup> )
<b>Without PMMA</b>	15.139	<b>15.027</b>	17.238
<b>Bare PMMA</b>	<b>13.709</b>	13.912	14.902
<b>S2 back</b>	<b>14.075</b>	14.349	15.205
<b>S2 back + hydrophobic</b>	<b>14.005</b>	14.352	15.208

Table 4. Summarized  $J_{sc}$  in mA/cm<sup>2</sup> of each sub-cell without PMMA substrate and placed below bare and textured PMMA substrates. The limiting  $J_{sc}$  is indicated in red.

#### 4.5.2. Irradiance and spectral homogeneity effect

The irradiance spectral and intensity homogeneity on each of the sub-cells, as well as the tracking precision can also severely affect the Current-Voltage curves depending on the type of CPV system as shown in Fig. 4.18 and Fig. 4.19. FF decrease was observed in both UT-CPV (RTP type) and LPI's Ventana CPV (FK type), despite large difference on their dependence on irradiance and spectral homogeneity shown in Fig. 4.18 and Fig. 4.19.

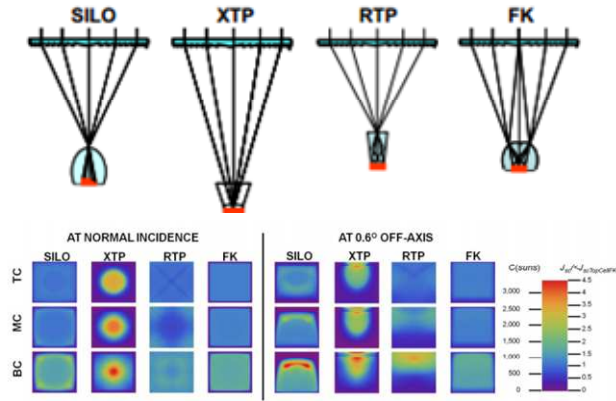


Fig. 4.18. Irradiance distribution on each sub-cell for different types of CPV systems at normal incidence and at 0.6° OFF-AXIS. Figures are from Ref. [12].

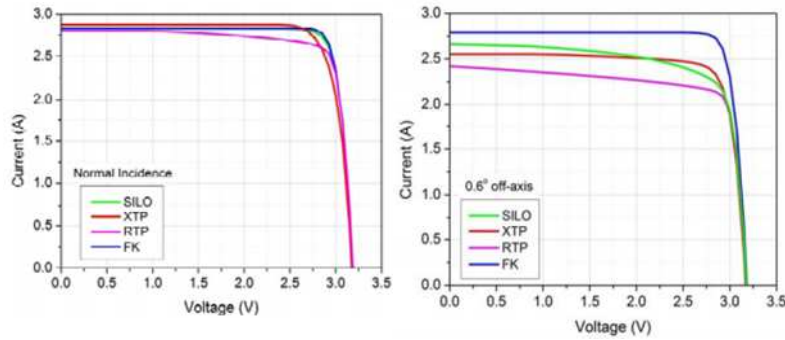


Fig. 4.19. Current-Voltage curves calculations based on the irradiance distributions on each sub-cell for different types of CPV systems at normal incidence and at 0.6° OFF-AXIS. Figures are from Ref. [12].

The FF decrease was not the results of a bottom-cell being current-limiting and it does not seem to be originated from irradiance or spectral inhomogeneity. In both UT-CPV and LPI's CPV system, lower concentration tests need to be carried out to confirm whether the FF decrease was actually a result of cell overheating caused by the additional current generated by the enhanced transmittance.



# **Chapter 5**

## **5. Applications of this research in other fields**

## 5.1. Flat PV

In order to evaluate the applicability to flat Photovoltaics (PV) of the obtained nanostructured surfaces on glass and PMMA, External Quantum Efficiency (EQE) measurements using an InGaAs / GaAsSb Quantum Dot solar cell (QDSC) placed below the bare and textured glass and PMMA substrates were carried out. The QDSC are also useful to evaluate the potential solar cell enhancement up to about  $1\mu\text{m}$ .

### 5.1.1. Quantum-Dot solar cells below glass substrates

The measurement setup employed to evaluate the EQE of an InGaAs / GaAsSb QDSC placed 4 cm below the bare and treated glass substrates is shown in Fig. 5.1.

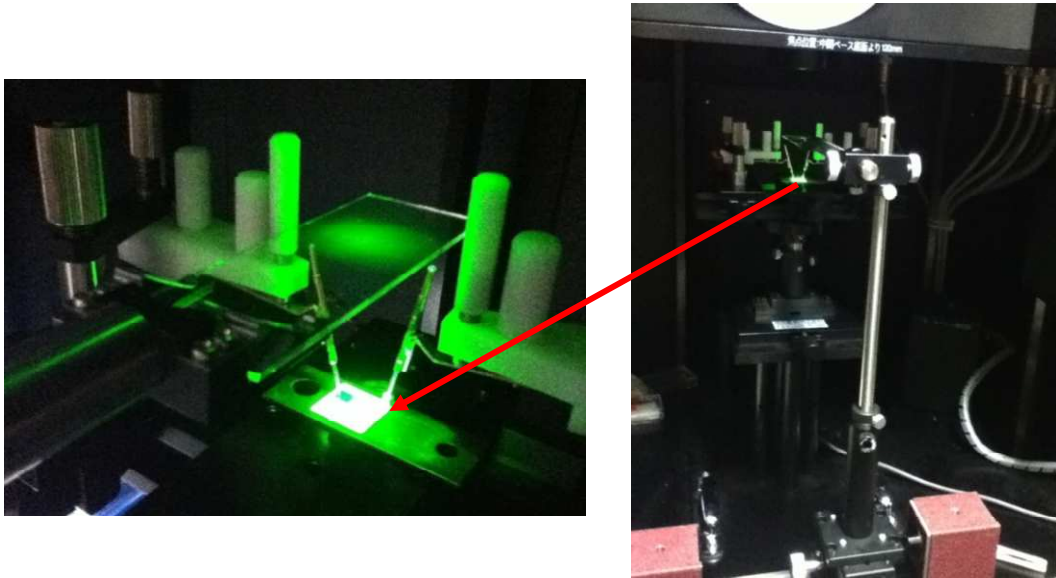


Fig. 5.1. Image of the treated glass substrates placed 4 cm above the InGaAs / GaAsSb QDSC during EQE measurements.

The transmittance spectra of the bare and treated samples just after 20, 40, and 60 min  $\text{CHF}_3$  plasma etching is shown in Fig. 5.2 (left). The increased transmittance enhancement after 10 min  $\text{O}_2$  plasma etching cleaning process is shown in Fig. 5.2 (right). In the case of substrates etched during 40-60 min, broadband transmittance enhancement of 3-4%, which is close to the ideal case, was obtained.



The sample treated during 40 min showed slightly higher transmittance at short wavelengths than the one treated during 60 min. This may correspond to scattering of short wavelengths by slightly larger nanostructures obtained after 60 min  $\text{CHF}_3$  plasma etching.

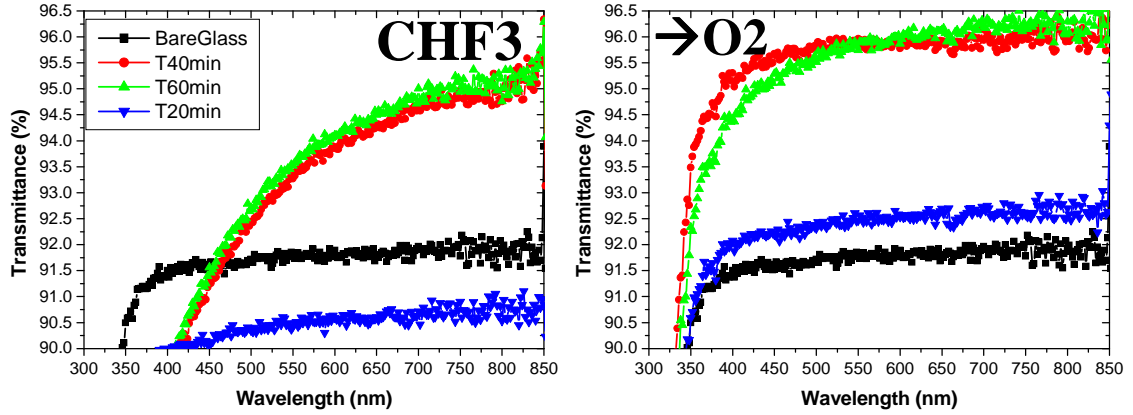


Fig. 5.2. Transmittance spectra of the bare glass substrates and after  $\text{CHF}_3$  (left) and subsequent  $\text{O}_2$  (right) plasma etching processes.

The measured EQE of an InGaAs / GaAsSb QDSC placed 4 cm below the textured and bare substrates is shown in Fig. 5.3. The enlarged EQE region in Fig. 5.3 shows clearly the EQE enhancement obtained for the case of substrates having one side etched during 40 and 60 min. The increase obtained after 20 min etching is much lower.

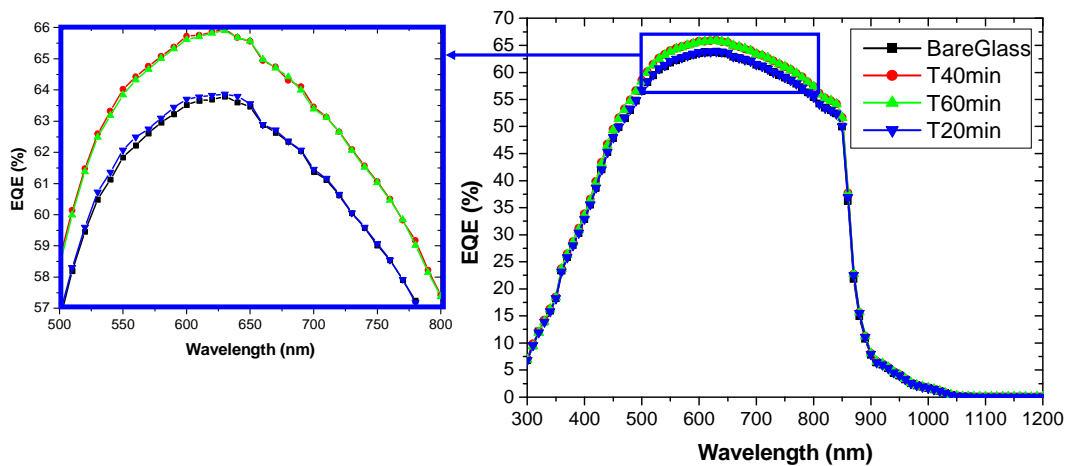


Fig. 5.3. EQE measurements of an InGaAs / GaAsSb QDSC placed 4 cm below the bare and textured substrates.

The calculated  $J_{sc}$  from the EQE measurements is summarized in Table 5. The current increased for all texturing conditions and the largest increase, 3.40%, was obtained for the texture obtained after 40 min etching.

Table 5			
Sample	$J_{sc}$ (mA/cm <sup>2</sup> )	Relative (%)	Absolute (mA/cm <sup>2</sup> )
Bare	17.93	Ref.	Ref.
T 20 min	17.97	0.22	0.04
T 40 min	18.54	3.40	0.61
T 60 min	18.51	3.23	0.58

Table 5. Summarized relative and absolute  $J_{sc}$  gains of the textured glass substrates compared to the bare one.

The EQE obtained placing the InGaAs / GaAsSb QDSC below the bare glass substrate was used as reference to normalize the EQE obtained when placing the textured substrates as shown in Fig. 5.4.

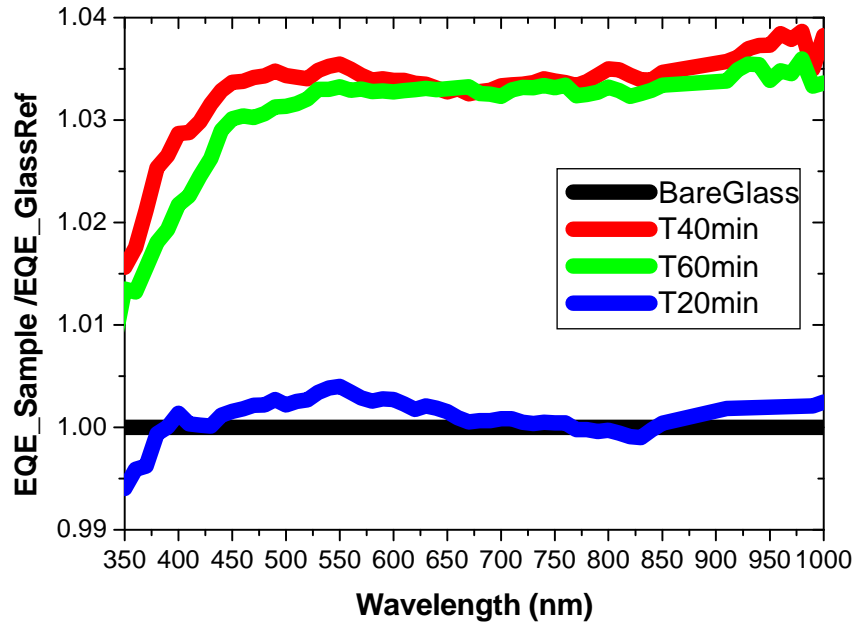


Fig. 5.4. Ratio between the EQE of the InGaAs / GaAsSb QDSC placed below the textured substrates and the bare glass.

Figure 5.4 shows that the EQE enhancement is larger for the 40 min etching case than the 60 min one, especially at short wavelengths. This explains the higher  $J_{sc}$  shown in Table 5. The higher transmittance at shorter wavelengths of 40 min is consistent with the higher EQE in this spectral region.

In all cases the EQE enhancement was slightly lower than the transmittance enhancement. The transmittance measurements were carried out using an integrating sphere and the substrates were placed in contact with the integrating sphere's port. On the other hand for the EQE measurements, the glass substrates were placed 4 cm above the InGaAs / GaAsSb QDSC. The small disagreement between these two enhancements may correspond to scattering or sample inhomogeneity. Nevertheless, 3-3.5% EQE improvement was observed between 400-1000 nm and maximum increase of  $J_{sc}$  reaching 3.40% was achieved, which demonstrates the potential of the applicability of the developed maskless plasma etching nanostructuration process to flat PV. Also, this process is suitable for current industrial fabrication lines. Since the open-circuit voltage and the fill factor are not modified, the conversion efficiency enhancement is expected to be the same as the one of  $J_{sc}$ . The mechanical durability should also be evaluated for a complete assessment of the applicability to flat PV.

### 5.1.2. Quantum-Dot solar cells below PMMA substrates

The EQE of an InGaAs / GaAsSb QDSC placed 6 cm below the bare and treated PMMA substrates described in section 3.8 is shown in Fig. 5.5.

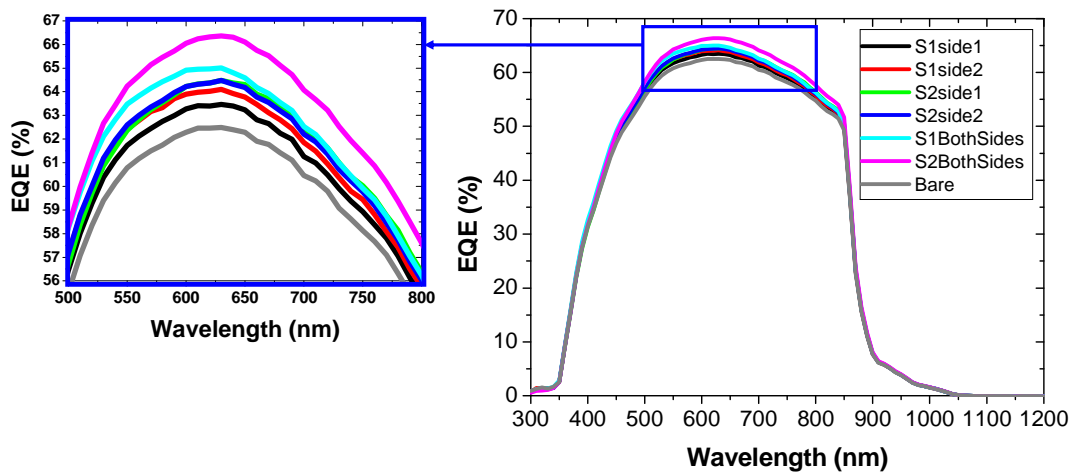


Fig. 5.5. EQE measurements of an InGaAs / GaAsSb QDSC placed 6 cm below the bare and textured substrates.

The enlarged EQE region in Fig. 5.5 shows clearly the EQE enhancement in the 500-800 nm spectral region, in which the effect of each texture can be differentiated. The calculated  $J_{sc}$  from the EQE measurements is summarized in Table 6. The current increased for all texturing conditions and the largest increase, 5.36%, was obtained for the texture S2-both-sides

<b>Table 6</b>			
<b>Sample</b>	<b><math>J_{sc}</math> (mA/cm<sup>2</sup>)</b>	<b>Relative (%)</b>	<b>Absolute (mA/cm<sup>2</sup>)</b>
<b>Bare</b>	17.52	Ref.	Ref.
<b>S1 side1</b>	17.77	1.43	0.25
<b>S1 side2</b>	17.93	2.34	0.41
<b>S2 side1</b>	17.99	2.68	0.47
<b>S2 side2</b>	18.01	2.80	0.49
<b>S1 both sides</b>	18.17	3.71	0.65
<b>S2 both sides</b>	18.46	5.36	0.94

Table 6. Summarized relative and absolute  $J_{sc}$  gains of the textured PMMA substrates compared to the bare one.

The transmittance obtained for the bare PMMA substrate was used to normalize the one of all textured substrates. In a similar way, the EQE obtained when placing the InGaAs / GaAsSb QDSC below the bare PMMA substrate was used as reference to normalize the EQE obtained when placing the textured substrates. Figure 5.6 summarizes the transmittance and EQE enhancements. For sample S1-side2 and S2-side1, both enhancements were very close. For all other samples the transmittance enhancement was higher than the EQE enhancement. The EQE measurements were carried out placing the PMMA substrates 6 cm above the QDSC. On the other hand, the transmittance measurements were carried out placing the substrates 2 mm from the integrating sphere. When increasing the distance from the integrating sphere up to 20 cm the transmittance was decreased depending on the sample. The lowest decrease was 0.3% for sample S2-side1 and largest, 1.3%, for sample S1-both-sides. In addition, the sample inhomogeneity was evaluated. It was sample dependent and maximum, 0.4%, for S1-side1. The differences between the transmittance and the EQE enhancement are mainly due to a combination of these two factors.

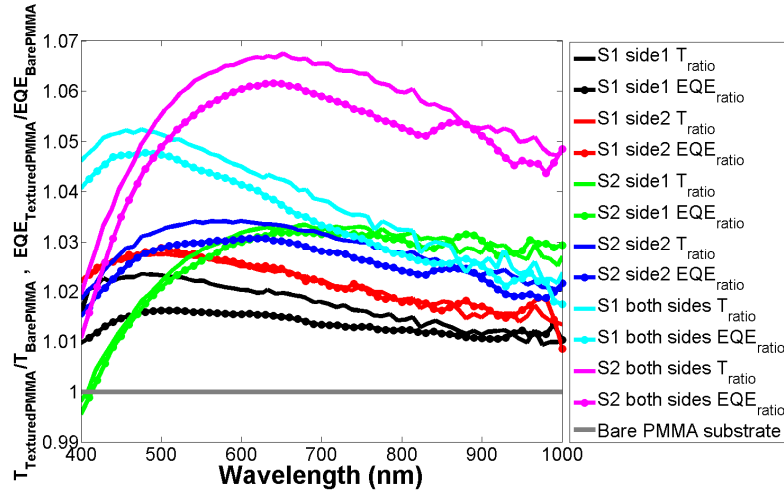


Fig. 5.6. Transmittance and EQE enhancements of textured PMMA substrates compared to bare one.

## 5.2. Cover glasses for solar cells in space

Qioptiq is the sole manufacturer of Ceria doped cover glasses that protect the solar cells in space against UV, electron, and proton irradiation. Reducing the reflectance at the Space/Glass interface would increase the efficiency of the solar cells, which can have effects on the cost of the mission reducing the number of cells required and their corresponding weight considering that launching 1 kg to space cost around 25,000 USD. If the same number of cells is kept, the improved efficiency of the cells can help power additional antennas or devices. In section 3.3.6 it was explained in detail the tests carried out and the broadband transmittance enhancement obtained on the three types cover glasses (CMG, CMX, and CMO). These results demonstrate the applicability of the maskless plasma etching process for space cover glasses from an optical point of view. Additional tests such as mechanical and irradiance durability are required in order to fully validate their applicability and suitability for the space environment.

## 5.3. Aspheric lenses

The AGL-30-23.5 aspheric condenser lenses made of B270 glass shown in Fig. 5.7 were provided by Sigma Koki and the maskless plasma etching surface nanostructuration process was tested on their curved surface.

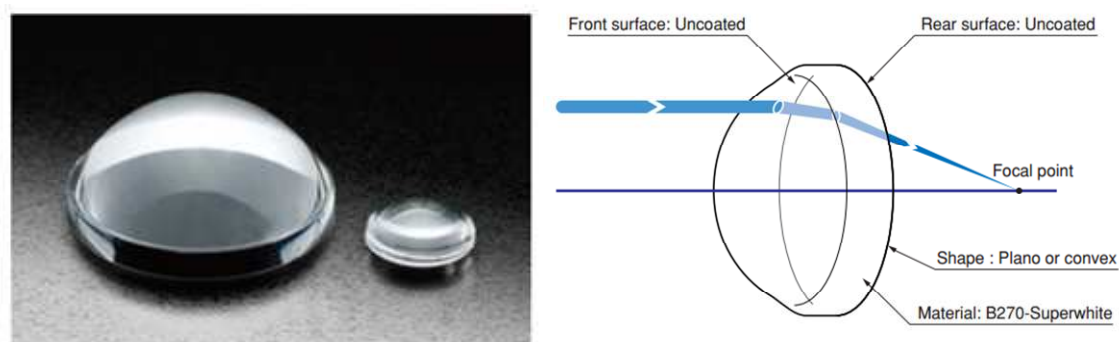


Fig. 5.7. Sigma Koki's Aspheric Condenser Lenses. Figure is from Ref. [70].

A collimated beam of 5 mm in diameter was employed to evaluate the transmittance of the treated aspheric condenser lenses at the center, 5 mm to the left, and 5 mm to the right as shown in Fig. 5.8. Figure 5.8 shows that a transmittance enhancement within 2-2.5% was achieved on AGL-30-23.5 aspheric condenser lenses by applying  $\text{CHF}_3$  plasma etching during 120 min and subsequent 10 min  $\text{O}_2$  plasma etching and deionized water cleaning processes. This transmittance enhancement supports the results obtained on the curved surface of LPI's SOE, and further improvement would depend on further optimizing the  $\text{CHF}_3$  plasma etching parameters.

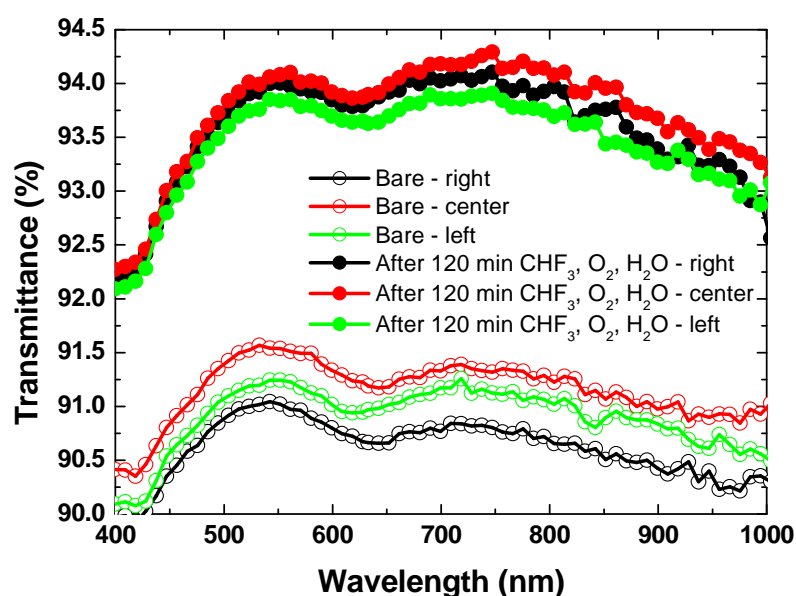


Fig. 5.8. Transmittance spectra of bare (left), after  $\text{CHF}_3$  (40 min) and  $\text{O}_2$  (10 min) plasma etching (middle), and after water rinsing (right) processes on the curved side of Sigma Koki's AGL-30-23.5P lenses.

# **Chapter 6**

## **6. Summary and outlook**

In this thesis, the reduction of the reflectance at the three Air/Optical-elements interfaces in transmission-type CPV system was approached by nanostructuring the surfaces of the optical elements employing maskless plasma etching processes. As for the Fresnel lens surfaces, in collaboration with the Fraunhofer IOF, two types of antireflection structures were applied on PMMA substrates and on Fresnel lenses at the same time. As for the surface of the homogenizer, a new fabrication method using maskless  $\text{CHF}_3$  plasma etching was developed on B270 glass and then applied on the homogenizers. Also the application on hydrophobic coating as an alternative solution to the dew accumulation on the back-side of Fresnel lenses was evaluated.

In chapter 3, the developed maskless surface nanostructuration  $\text{CHF}_3$  plasma etching process was presented. This process was developed using B270 glass because of its composition resemblance to the composition of the homogenizer in LPI's CPV system. The whole fabrication process can be completed within one hour and it has been applied on over a hundred of samples with good reproducibility and no significant dependence on the chamber history, which makes it suitable and cost effective for large scale applications compared to processes depending on lithography or assistance-masks. Based on XPS, STEM-EDX, Dektak, and SEM results, a model describing the fabrication process that occurred on B270 was proposed. Based on STEM-EDX cross section compositions mapping and the pillar shape and aspect ratio dependence on  $\text{CHF}_3$  plasma etching time, together with FDTD and RCWA simulations it was found that the graded  $\text{SiO}_2$  density in the nanostructures played a key role in order to reach the obtained broadband transmittance enhancement. The same fabrication process was evaluated in various glasses including a customized composition, space cover glasses, and quartz. Based on the characteristics of the reactive products generated from the glass and the  $\text{CHF}_3$  plasma etching, the optical, morphological, and surface composition measurements, a possible explanation of the role of the glass composition was also proposed.  $\text{BaF}_2$  and  $\text{CeF}_3$  are both materials with very high durability against electron and proton radiation. Whether the accumulation of (Ba, F) and (Ce, F) at the tips of the nanostructures enhances the radiation durability needs to be evaluated. It was found that under the evaluated fabrication conditions, (Ca, F) and (Ce, F), and very good self-generated masks that under sustained  $\text{CHF}_3$  plasma etching achieve almost ideal broadband transmittance enhancement owing to the fabrication of small and high aspect ratio nanostructures with graded  $\text{SiO}_2$  density. It is not clear whether (Ba, F) played a role in the fabrication of the nanostructured surface of space cover glasses. Further study of the role of (Ba, F) as well as other self-generated masks is suggested as part of future work.



In order to further understand the fabrication processes, nanostructures shapes, etching depth, and STEM-EDX cross section mapping are suggested on the nanostructured surfaces obtained on each type of glass. Finally, evaluation of more compositions and the influence of the fabrication parameters are also suggested.

In chapter 4 the CPV field tests carried out in order to evaluate the performance of each treated optical interface were described. LPI's treated POEs at Fraunhofer IOF, together with the treated SOEs with the newly developed fabrication process, were assembled and tested at LPI-CeDint facilities (Madrid, Spain). The maximum improvement on the POEs was obtained when applying S2 on both sides, reaching 6.56% and 3.82%  $J_{sc}$  and efficiency relative gains, respectively. As for the SOEs, maximum 3.78% and 2.75%  $J_{sc}$  and efficiency relative gains were obtained, respectively.

Finally, the CPV module assembled using the Fresnel lens with S2 on both sides and the best treated homogenizer showed maximum 7.99% and 5.06%  $J_{sc}$  and efficiency relative gains, respectively. The efficiency relative gains were lower than the  $J_{sc}$  ones because the FF was degraded on the textured samples. In order to clarify the origin of the FF decrease, it was found that the bottom cell does not become current limiting when employing the antireflection nanostructures. The evaluation of the hydrophobic coating was carried out using University of Tokyo's CPV system. Despite the slight decrease in the transmittance at short wavelengths observed after hydrophobic coating, 7.73%  $J_{sc}$  relative gain was obtained, which exceeds in about 5% the expected relative gain compared to the uncoated Fresnel lens with S2 on the back side that showed a 2.87%  $J_{sc}$  relative gain. Regarding the field tests, there are two key points that are suggested as part of future work 1) evaluation of the antireflection nanostructures under lower concentration to clarify if the origin of the FF decrease was caused by cell overheat originated by the increased current, and 2) evaluation of the focal position dependence on the Fresnel lenses with and without hydrophobic coating in order to clarify whether the additional 5% gain resulted in focal point variation in UT-CPV system.

In chapter 5, EQE enhancement of InGaAs / GaAsSb QDSC placed below textured glass and PMMA substrates was obtained showing the potential application of the nanostructured surfaced for flat PV. The broadband transmittance enhancement obtained on the three types of space cover glasses demonstrated the applicability of the CHF<sub>3</sub> maskless plasma etching process to improve the efficiency of solar cells in space. Part of future work in this direction includes the evaluation of the mechanical durability of the nanostructures as well as the high energy electron and proton radiation durability.



## 7. Bibliography

- [1] W. Shockley and H. J. Queisser, Detailed balance limit of efficiency of p-n junction solar cells, *J. Appl. Phys.*, **32**, 1961, pp. 510-519.
- [2] S. M. Sze and Kwok K. Ng, *Physics of Semiconductor Devices*, Wiley, 2007.
- [3] R. R. King, D. Bhusari, D. Larrabee, X.-Q. Liu, E. Rehder, K. Edmondson, H. Cotal, R. K. Jones, J. H. Ermer, C. M. Fetzer, D. C. Law and N. H. Karam, Solar cell generations over 40% efficiency, *Prog. Photovolt.*, *26th EUPVSEC*, 2011.
- [4] Y. Okada, T. Morioka, K. Yoshida, R. Oshima, Y. Shoji, T. Inoue, and T. Kita, Increase in photocurrent by optical transitions via intermediate quantum states in direct-doped InAs/GaNAs strain-compensated quantum dot solar cell, *J. Appl. Phys.*, **109**, 2011, pp. 024301-024305.
- [5] R. T. Ross and A. J. Nozik, Efficiency of hot-carrier solar energy converters, *J. Appl. Phys.*, **53**, 1982, pp. 3813-3818.
- [6] T. Trupke, M. A. Green, and P. Würfel, Improving solar cell efficiencies by up-conversion of sub-band-gap light, *J. Appl. Phys.*, **92**, 2002, pp. 4117-4122.
- [7] T. Trupke, M. A. Green, and P. Würfel, Improving solar cell efficiencies by down-conversion of high-energy photons, *J. Appl. Phys.*, **92**, 2002, pp. 1668-674.
- [8] O. E. Semonin, J. M. Luther, S. Choi, H. Y. Chen, J. Gao, A. J. Nozik, and M. C. Beard, Peak external photocurrent quantum efficiency exceeding 100% via MEG in a quantum dot solar cell, *Science*, **334**, 2012, pp. 1530-1533.
- [9] National Renewable Energy Laboratory (NREL), Research-cell efficiency records, as of January 20<sup>th</sup> of 2013.
- [10] Karin Hinzler, SUNLAB: [sunlab.site.uottawa.ca](http://sunlab.site.uottawa.ca).
- [11] Sarah Kurtz, High-efficiency, multijunction solar cells for large-scale solar electricity generation, *APS March Meeting*, 2006.
- [12] P. Espinet-González, R. Mohedano, I. García, P. Zamora, I. Rey-Stolle, P. Benitez, C. Algora, A. Cvetkovic, M. Hernández, J. Chaves, J.C. Miñano, and Y. Li, Triple-junction Solar Cell Performance Under Fresnelbased Concentrators Taking Into Account Chromatic Aberration And Off-axis Operation, *CPV-8th*, 2012.

- [13] P. Benitez *et al.*, “High performance Fresnel-based photovoltaic concentrator”, *OPTICS EXPRESS*, **18**, 2010, pp. A25-A39.
- [14] D.C. Miller, M.D. Kempe, C.E. Kennedy, and S.R. Kurtz, Analysis of Transmitted Optical Spectrum Enabling Accelerated Testing of CPV Designs, *Conference Paper NREL/CP-520-44968*, July, 2009.
- [15] M. Yamaguchi and A. Luque, “High Efficiency and High Concentration in Photovoltaics”, *IEEE Trans. On Elec. Dev.*, **46**, 1999, pp. 2139-2144.
- [16] P. Zamora, P. Benitez, R. Mohedano, A. Cvetkovic, Juan Vilapana, Y. Li, M. Hernández, J. Chaves, and J.C. Miñano, Experimental characterizations of Fresnel-Kohler concentrators, *J. of Photonics for Energy*, **2**, 2012, pp. 021806-1-9.
- [17] M. Victoria, C. Domínguez, I. Antón, and G. Sala, Antireflective coatings for multijunction solar cells under wide-angle ray bundles, *Optics Express*, **20**, 2012, pp. 8136-8147.
- [18] M. Victoria, C. Domínguez, I. Antón, and G. Sala, Comparative analysis of different secondary optical elements for aspheric primary lenses, *Optics Express*, **17**, 2009, pp. 6487-6492.
- [19] U. Schulz, P. Munzert, R. Leitel, I. Wendling, N. Kaiser, and A. Tünnermann, “Antireflection of transparent polymers by advanced plasma etching procedures“, *Optics Express*, **15**, 2007, pp. 13109-13113
- [20] A. Kaless, P. Munzert, U. Schulz, and N. Kaiser, “Nano-motheye antireflection pattern by plasma treatment of polymers“, *Surface & Coating Technology*, **20**, 2004, pp. 58-61
- [21] U. Schulz, P. Munzert and N. Kaiser, "Plasma Surface Modification of PMMA for Optical Applications", *Journal of Adhesion Science and Technology*, **24**, 2010, pp. 1283–1289
- [22] Moharam, M. G., and Gaylord, T. K., “Diffraction analysis of dielectric surface-relief gratings,” *J. Opt. Soc. Am.*, **72**, 10, 1982, pp. 1385-1392.
- [23] H. Sai et al., “Wide-angle Antireflection Effect of Subwavelength Structures for Solar Cells” *Jap. J. of Appl. Phys.*, **46**, 6A, 2007, pp. 3333-3336.
- [24] Y. Kemmoku, K. Araki, and S. Oke, Estimation of influence of dew condensation on annual generated energy of a concentrator PV system, *27th EUPVSEC*, 2012.
- [25] Andreas Gombert *et al.*, Field performance of FLATCON® power plants and demo systems, *CPV-6th*, 2010.
- [26] Yeuh-Yeong Liou, Li-Hsiang Kuo, Jhong-Yong Yan, and Cheng-Chung Jaing, Implementation of Universal Broadband Visible Antireflection Coating for

- Various Glass Substrates Using Ion-Assisted Deposition, *Jap. J. of Appl. Phys.*, **51**, 2012, pp. 042501-1-6.
- [27] Hakan Deniz, Tural Khudiyev, Fatih Buyukserin, and Mehmet Bayindir, Room temperature large-area nanoimprinting for broadband biomimetic antireflection surfaces, *Appl. Phys. Lett.*, **99**, 2011, pp. 183107-1-3.
  - [28] Sameer Chhajed et al., Nanostructured Multilayer Tailored-Refractive-Index Antireflection Coating for Glass with Broadband and Omnidirectional Characteristics, *Appl. Phys. Express*, **4**, 2011, pp. 052503-1-3.
  - [29] Kyoo-Chul Park et al., Nanotextured Silica Surfaces with Robust Superhydrophobicity and Omnidirectional Broadband Supertransmissivity, *ACSNANO*, **6**, 2012, pp. 3789-3799.
  - [30] Clapham, P.B. and Hutley, M.C., Reduction of lens reflection by the 'Moth Eye' principle, *Nature*, 244, 1973, pp. 281-2.
  - [31] Wilson, S.J. & Hutley, M.C., The optical properties of 'moth eye' antireflection surfaces, *Optica Acta*, **29**, No. 7, 1982, pp. 993-1009.
  - [32] Hobbs, D.S., MacLeod, B.D., Update on the Development of High Performance Anti-Reflecting Surface Relief Micro-Structures, *Proc. SPIE* 6545, 2007, pp. 65450Y.
  - [33] J. Achteik, W. Sievers and J.K.N. Lindner, Biomimetic approaches to create anti-reflection glass surfaces for solar cells using self-organizing techniques, *Materials Science and Engineering B*, **178**, 2013, pp. 635-638.
  - [34] J. Achteik, R.M. Kemper, W. Sievers, J.K.N. Lindner, *Materials Research Society Online Proceedings Library*, 1389, 2012, mrsf11-1389-g03-18
  - [35] Jung Suk Kim, Hyun Woo Jeong, Wonbae Lee, Bo Gi Park, Beop Min Kim and Kyu Back Lee, A simple and fast fabrication of a both self-cleanable and deep-UV antireflective quartz nanostructured surface, *Nanoscale Research Letters*, **7**, 2012, pp. 430.
  - [36] T. Lohmüller, M. Helgert, M. Sundermann, R. Brunner, J.P. Spatz, Biomimetic Interfaces for High-Performance Optics in the Deep-UV Light Range, *Nanoletters* **8**, 2008, pp. 1429.
  - [37] Jung Woo Leem et. al., Enhanced transmittance and hydrophilicity of nanostructured glass substrates with antireflective properties using disordered gold nanopatterns, *OPTICS EXPRESS*, **20**, 4, 2012, pp. 4056-4066.
  - [38] Douglas S. Hobbs., Laser damage threshold measurements of antireflection microstructures in the near UV and mid-infrared *Proc. of SPIE*, 7842, 2102, pp. 7842Z-1-12.

- [39] Young Min Song et al., Enhanced power generation in concentrated photovoltaics using broadband antireflective coverglasses with moth eye structures, *OPTICS EXPRESS*, **5**, 2012, Vol. 20, A916
- [40] R. Angel, T. Connors, W. Davison, B. Olbert, and S. Sivanandam, New architecture for utility scale electricity from concentrator photovoltaics, *Proc. SPIE* 7769, High and Low Concentrator Systems for Solar Electric Applications V, 2010, pp. 776903.
- [41] Qifeng Zhang, Daniel Myers, Jolin Lan, Samson A. Jenekhe and Guozhong Cao, Applications of light scattering in dye-sensitized solar cells, *Phys. Chem. Chem. Phys.*, **14**, 2012, pp. 14982–14998.
- [42] A. G. Aberle, P. I. Widenborg, and N. Chuangsuwanich, Glass Texturing, *Patent Cooperation Treaty*, International Publication Number WO 2004/089841 A1.
- [43] C. F. Madigan, M.-H. Lu, and J. C. Sturm, Improvement of output coupling efficiency of organic light-emitting diodes by backside substrate modification, *Appl. Phys. Lett.* **76**, 2000, pp. 1650–1652.
- [44] H. Fouckhardt, I. Steingoetter, M. Brinkmann, M. Hagemann, H. Zarschizky, and L. Zschiedrich, nm- and  $\mu$ m-scale surface roughness on glass with specific optical scattering characteristics on demand, *Adv. OptoElectron.*, 2007, pp. 27316.
- [45] M.-H. Lu and J. C. Sturm, Optimization of external coupling and light emission in organic light-emitting devices: modelling and experiment, *J. Appl. Phys.*, **91**, 2002, pp. 595–604.
- [46] E. Yablonovitch, Statistical ray optics, *J. Opt. Soc. Am.*, **72**, 1982, pp. 899-907.
- [47] M. Affatigato, D. H. Osborne, and R. F. Haglund Jr., Effect of surface roughness on the acid etching of amorphous silica, *Journal of the American Ceramic Society*, **79**, no. 3, 1996, pp. 688–694.
- [48] A. Ben-Yakar et al., Morphology of femtosecond-laser-ablated borosilicate glass surfaces, *Applied Physics Letters*, **83**, no. 15, 2003, pp. 3030–3032.
- [49] H. Fouckhardt, E. Hein, D. Fox, and M. Jaax, Multitude of glass surface roughness morphologies as a tool box for dosed optical scattering, *Appl. Opt.*, **49** 8, 2010, pp. 1364–1372.
- [50] E. Hein, D. Fox, and H. Fouckhardt, Self-masking controlled by metallic seed layer during glass dry-etching for optically scattering surfaces, *J. Appl. Phys.*, **107** 3, 2010, pp. 033301.
- [51] E. Hein, D. Fox, and H. Fouckhardt, Lithography-free glass surface modification by self-masking during dry etching, *J. of Nanophotonics*, **5**, 2011, pp. 051703-1-13.

- [52] E. Hein, D. Fox, H. Fouckhardt, Glass surface modification by lithography-free reactive ion etching in an Ar/CF<sub>4</sub>-plasma for controlled diffuse optical scattering, *Surface and Coatings Technology*, **205**, 2011, pp. S419–S424.
- [53] Rensselaer Polytechnic Institute: [www.scorec.rpi.edu](http://www.scorec.rpi.edu)
- [54] W. W. Stoffels, E. Stoffels, and K. Tachibana, Polymerization of fluorocarbons in reactive ion etching plasmas, *J. Vac. Sci. Technol., A*, **16**, 1998, pp. 1.
- [55] Lee JH, Kim JS, Park JS, Lee W, Lee KE, Han SS, Lee KB, Lee J, A threedimensional and sensitive bioassay based on nanostructured quartz combined with viral nanoparticles, *Adv. Funct. Mater.*, **20**, 2010, pp. 2004–2009.
- [56] M. M. Millard, J. J. Windle, and A. E. Pavlath, Plasma Synthesis of Fluorocarbon Films, *J. of Appl. Polymer Sci.*, **17**, 1973, pp. 2501-2507.
- [57] Philip G. Clark, Erik D. Olson, and Hiromi Kofuse, The use of segregated hydrofluoroethers as cleaning agents in electronics packaging applications, *International Conference on Soldering and Reliability*, Toronto, 2009.
- [58] Christoph M, Claudia P, Dennis L, Robert B, Michael H, Michael S, Joachim P.S, Tailored antireflective biomimetic nanostructures for UV applications, *Nanotechnology*, **21**, 2010, pp. 425301.
- [59] P. W. Leech, Reactive ion etching of piezoelectric materials in CF<sub>4</sub>/CHF<sub>3</sub> plasmas, *J. Vac. Sci. Technol., A*, **16**, 1998, pp. 2037.
- [60] E.E.Metwalli and C.G.Pantano, Reactive ion etching of glasses: Composition dependence, *Nucl. Instrum. Methods Phys. Res. B*, **207**, 1, 2003, pp. 21–27.
- [61] Leslie Glasser, and H. Donald Brooke Jenkins, Lattice Energies and Unit Cell Volumes of Complex Ionic Solids, *J. Am. Chem. Soc.*, **122**, 2000, pp. 632-638.
- [62] Simon Cotton, Lanthanide and Actinide Chemistry, *Wiley*, 2006.
- [63] R. D. Shannon, Revised Effective Ionic Radii and Systematic Studies of Interatomic Distances in Halides and Chalcogenides, *Acta Cryst., A*, **32**, 1976, pp. 751-767.
- [64] Ryosuke Kometani, Kenji Ishikawa, Keigo Takeda, Hiroki Kondo, Makoto Sekine, and Masaru Hori, A High-Temperature Nitrogen Plasma Etching for Preserving Smooth and Stoichiometric GaN Surface, *Applied Physics Express*, **6**, 2013, pp. 056201-1-4.
- [65] Gerhard Franz, Low Pressure Plasmas and Microstructuring Technology, *Springer*, 2009.
- [66] Gerhard Franz, Surface roughening of SiC and Ga-containing semiconductors in reactive plasmas, *Materials Science in Semiconductor Processing*, **2**, 1999, pp. 349-357.

- [67] K. S. Yee, IEEE Trans, *Antennas Propagat.*, *AP*, **14**, 1966, pp. 302.
- [68] Xiao Li, Longjian Xue and Yanchun Han, Broadband antireflection of block copolymer/homopolymer blend films with gradient refractive index structures, *J. Mater. Chem.*, **21**, 2011, pp. 5817-5826.
- [69] Dinguo Chen, Anti-reflection (AR) coatings made by solgel processes: A review, *Solar Energy Materials & Solar Cells*, **68**, 2001, pp. 313-336.
- [70] Aspheric Condenser Lenses in *Sigma Koki catalog*



# Publications and achievements

## 1. Journal papers to be submitted

- 1.1. Efrain E. Tamayo R., Takuya Hoshii, Kentaroh Watanabe, Ryo Tamaki, Masakazu Sugiyama, Yoshitaka Okada, and Kenjiro Miyano. “Maskless plasma etching fabrication of broadband antireflection or scattering nano-microstructures on glasses with different compositions”.
- 1.2. Efrain E. Tamayo R., Takuya Hoshii, Ryo Tamaki, Kentaroh Watanabe, Masakazu Sugiyama, Yoshitaka Okada, and Kenjiro Miyano. “Maskless plasma etching broadband antireflection nanostructures with graded composition on glass flat and curved surfaces”.
- 1.3. Efrain E. Tamayo R., James Hall, Takuya Hoshii, Andy Gray, Kentaroh Watanabe, Ryo Tamaki, Masakazu Sugiyama, Yoshitaka Okada, and Kenjiro Miyano. “Broadband antireflection nanostructures on Ceria-doped cover glasses for solar cells in space applications”.

## 2. International conferences

- 2.1. Efrain E. Tamayo R., Kentaroh Watanabe, Ryosuke Watanabe, Masakazu Sugiyama, Yoshitaka Okada, and Kenjiro Miyano, “Efficiency simulations of top surface light management structures for concentrator solar cells using RCWA and detailed balance theory”, 4th International Symposium on Innovative Solar Cells, 2012 (Tokyo, Japan).

- 2.2. Efrain E. Tamayo R., Kentaroh Watanabe, Ryosuke Watanabe, Masakazu Sugiyama, Yoshitaka Okada, and Kenjiro Miyano, “Efficiency simulations of top surface light management structures for concentrator solar cells using RCWA and detailed balance theory”, 38th IEEE PVSC, 2012, June (Austin, Texas, US).
- 2.3. Efrain E. Tamayo R., Kentaroh Watanabe, Masakazu Sugiyama, Takuya Hoshii, Yasushi Shoji, Yoshitaka Okada, and Kenjiro Miyano, “Fabrication of broadband antireflection structures on glass substrates by Reactive Ion Etching for application on homogenizers in CPV systems”, 39th IEEE PVSC, 2013, June (Tampa, Florida, US).
- 2.4. Efrain E. Tamayo R., Ryo Tamaki, Kentaroh Watanabe, Masakazu Sugiyama, Yasushi Shoji, Daniel J. Farrell, Yoshitaka Okada, and Kenjiro Miyano, Kevin Füchsel, Friedrich Rickelt, Peter Munzert, Andreas Büchtemann, and Ulrike Schulz, “Antireflection structures on Fresnel lenses fabricated by Induced Coupled Plasma etching for improving CPV Systems ”, 28th EUPVSEC, 2013, September (Paris, France).
- 2.5. Efrain E. Tamayo R., Ryo Tamaki, Kentaroh Watanabe, Masakazu Sugiyama, Yasushi Shoji, Takuya Hoshii, Daniel J. Farrell, Yoshitaka Okada, and Kenjiro Miyano, “Lithography-free nanostructures for optical management in CPV systems”, 6th International Symposium on Innovative Solar Cells, 2013 (Tokyo, Japan).

### 3. Others

#### 3.1. **Best poster award**

Efrain E. Tamayo R., Kentaroh Watanabe, Masakazu Sugiyama, Yasushi Shoji, Yoshitaka Okada, and Kenjiro Miyano, “Fabrication of broadband antireflection structures on glass substrates by Reactive Ion Etching for application on homogenizers in CPV systems”, 39th IEEE PVSC, 2013, June (Tampa, Florida, US).

#### 3.2. **Patent submission**

Patent submitted on Dec. 18<sup>th</sup> 2013: Fabrication of broadband antireflection or scattering nano-microstructures by maskless plasma etching on glasses with different compositions. Japanese Patent Application number 2013-260712.